

On the scalability of helium-filled soap bubbles for PIV measurements

Tim de Reijer

Delft University of Technology

On the scalability of helium-filled soap bubbles for PIV measurements

by

Tim de Reijer

to obtain the degree of Master of Science

at the Delft University of Technology,

to be defended publicly on Tuesday June 7, 2021 at 16:00 PM.

Student number:	4306570	
Date:	June 7, 2021	
Thesis committee:	Prof. Dr. F. Scarano,	Chair of assessment committee
	Dr. A. Sciacchitano,	Supervisor
	Ir. E. Saredi	Daily Supervisor
	Dr. S. Ghaemi,	Examiner
	Dr. D. Engler Faleiros,	Examiner

An electronic version of this thesis is available at <http://repository.tudelft.nl/>.

Abstract

In connection with attempts to expand the maximum attainable measurement domain of volumetric Particle Image Velocimetry (PIV), a research project is carried out into the production flexibility and scalability of helium-filled soap bubbles (HFSB). Based on a literature survey, limitations of PIV systems have been identified which fail to meet the demand for large-scale, industrial wind tunnel experiments. The reason for this is the limited available energy density supplied by conventional light sources, providing sufficient contrast between the image background and the light scattered by tracer particles. Henceforth, state-of-the-art time-resolved volumetric measurements with helium-filled soap bubbles have not yet been performed on domains larger than the human body itself. These domains are deemed to be too small for automotive, aerospace and wind energy industries. Proposed solutions such as increasing the laser power have high costs associated with them. Furthermore, traversing or robotic PIV measurements are time-consuming and suffer from the need to time-average the velocity data, only providing insight into the statistics of the mean flow.

The third solution is to scale particles, increasing the intensity of the light scattered from the particle to the camera sensor. Using an existing ray-tracing model, the light scattering behaviour of soap bubbles is analysed. With this model, the quadratic relationship between the intensity of scattered light from a particle and its diameter is confirmed. It is for this reason that the introduction of sub-millimetre HFSB has increased the measurement domain of volumetric three-component time-resolved experiments from 10^4 cm^3 , achieved by conventional micron-sized particles, to 10^4 cm^3 . A subsequent theoretical analysis of the attainable measurement domain for varying particle diameter shows that for particles five times larger than conventional HFSB, the measurement domain can be increased from 10^4 to 10^5 cm^3 . This demonstrates the potential of scaling HFSB to lift some of the restrictions for large-scale PIV measurements. Consequently, the flexibility and scalability in the production of HFSB have been assessed by analysing and changing the design of the HFSB nozzle generator used by TU Delft.

An experimental set-up is realised to localise the light intensity peaks of individual glare points originating from the bubble's surface. The distance between interpolated, sub-pixel accurate glare points is subsequently used to derive the average bubble diameter based on a Gaussian least-squares fit of the particle size distribution. The produced bubbles comply with the theoretical neutrally buoyant condition so that the flow can be followed faithfully with these tracers. The effect of varying operational parameters is analysed by changing the flow rates of air, helium and soap. The nozzle scale and the orifice diameter are the geometrical parameters considered in this study. It is found that pure geometrical scaling leads to excessive accumulation of soap within the nozzle, resulting in blockage and therefore failing to produce bubbles. However, updating the internal soap channels has shown significant improvements.

A novel, physics-based model is presented which couples operational and geometrical parameters to the HFSB diameter. So far, scientific literature has only established data-driven relationships between these variables. The proposed model is benchmarked with experimental data and is in good agreement with the given proportionality for a broad spectrum of operational conditions. Additionally, bubble diameter is scaled from 0.5 mm produced by conventional nozzles to 2.5 mm with a scaled and improved nozzle. This corresponds to a 25 fold increase in the volume compared to the current operational domain for HFSB experiments, or a 3 fold increase along all dimensions.

Conclusively, the identified need for large-scale PIV measurements is addressed by designing and improving the conventional HFSB nozzle generator used by Delft University of Technology. This research highlights the flexibility of the operational range of nozzle generators and the scalability of the resulting bubbles. It also provides guidelines for designing nozzles for a particular experimental arrangement, requiring a specific bubble size. The 5 fold increase in particle diameter compared to conventional

HFSB further closes the gap between PIV measurements and the identified need for its application on a larger scale. Recommendations include further increasing the size of the nozzle while carefully controlling the size of internal channels, as well as investigating the effect of the orifice length and shape.

Contents

Abstract	iii
List of Figures	ix
List of Tables	xiii
List of Symbols	xv
List of Abbreviations	xix
1 Introduction	1
2 Particle Image Velocimetry	3
2.1 History of Applications	3
2.2 Working Principle	4
2.2.1 Imaging and Digital Image Recording	5
2.2.2 Illumination	6
2.2.3 Image Analysis	7
2.3 Flow Seeding Particles	8
2.3.1 Particle Dynamics	8
2.3.2 Tracer Fidelity	9
2.3.3 Optical Characteristics	11
2.3.4 Tracer Types	12
2.4 Seeding Concentration & Measurement Spatial Resolution	13
2.5 Measurement Domain	13
3 Use and Scaling of HFSB	15
3.1 History of applications	15
3.2 Working Principle	16
3.3 Production Methods	17
3.4 Production Regimes	19

3.5	Fluid Mechanical Properties	22
3.5.1	Particle Dynamics	22
3.5.2	Tracing Fidelity	23
3.6	Optical Characteristics	26
3.7	Bubble Scalability.	27
3.8	Extended Optical Analysis	29
3.8.1	Ray Tracing Model	29
3.8.2	Scattering Intensity	30
3.9	Measurement Volume	31
3.10	Discussion	33
4	Experimental Set-up and Procedures	37
4.1	Experimental Apparatus	37
4.2	Nozzle Design	38
4.3	Calibration Curves	41
4.4	Acquisition Strategy	44
4.5	Image Pre-processing	45
4.6	Bubble diameter determination	46
4.7	Data Reduction Techniques	47
4.8	Operating Regime Determination	48
4.9	Production Frequency	48
4.10	Uncertainty Analysis	49
5	Results & Discussion	51
5.1	General Nozzle Performance	51
5.2	Mean Bubble Diameter.	53
5.3	Bubble Diameter Dispersion	60
5.4	Detailed Nozzle Performance	61
5.5	Production Frequency	65
6	Conclusion & Recommendations	67
6.1	Conclusion	67
6.2	Recommendations	68

A Test matrices	71
B Code Flowchart	73
Bibliography	75

List of Figures

2.1	Various applications of PIV. From top left, CW: flapping-wing micro air vehicles (Herrero et al. 2018), full-scale swimmer's hand (Berg et al. 2019), F1 tire wake analysis (Nakagawa et al. 2016), near wake of a vertical axis wind turbine (Tescione et al. 2014), vortices over a delta wing (Caridi et al. 2017) and flow diagnostics in biomedical flows (TSI Incorporated 2019).	4
2.2	Overview of a PIV measurement set-up. Reproduced from Raffel et al. (2018).	5
2.3	PIV and PTV image processing procedures. Adapted from Lynch (2015).	5
2.4	Schematic representation of a double-pass illumination arrangement. Reproduced from Scarano (2013a).	7
2.5	Three-dimensional overview of a multi-pass illumination system. Reproduced from Ghaemi and Scarano (2011).	7
2.6	Image analysis operating sequence. Adapted from Scarano (2013b) and Raffel et al. (2018).	7
2.7	Particle drag coefficient for finite particle Reynolds number Re_p , modelled after Stokes, Oseen and Schiller and Neumann (SN). Reproduced from Marshall and Li (2014).	9
2.8	Drag correction term ϕ for finite particle Reynolds number Re_p , modelled after Stokes, Oseen and Schiller and Neumann (SN). Adapted from Marshall and Li (2014).	9
2.9	Particle slip velocity. Reproduced from Scarano (2013b).	11
2.10	Particle lag after a velocity step change. Reproduced from Scarano (2013b).	11
2.11	Scattering intensity and the relation with the Mie parameter for a scattering angle of 90° . Adapted from Tropea (2011).	12
2.12	Scattered light intensity distribution as a function of the scattering angle at $x_* = 10$. The solid line represents perpendicular polarization, parallel polarization is represented by the dashed line. Adapted from Tropea et al. (2007).	12
2.13	Traversing stereoscopic PIV system within a Formula One wind tunnel. Reproduced from Senft and Gillan (2019).	14
2.14	Robotic Coaxial Volumetric Velocimetry on a full-scale cyclist. Reproduced from Jux et al. (2018).	14
3.1	First commercially available HFSB nozzle generator. Reproduced from Hale et al. (1971).	16
3.2	Schematic of an orifice-type nozzle used to produce HFSB. Adapted from Faleiros et al. (2018).	17
3.3	Schematic illustration of the fluid supply unit (FSU). Reproduced from Morias (2016).	17

3.4	Schematic sectional comparison between pitot- and orifice-type nozzles. Reproduced from Okuno et al. (1993).	17
3.5	Schematic illustration of the DLR nozzle. Reproduced from Bosbach et al. (2009).	18
3.6	Schematic illustration of the nozzles used in the study by Faleiros et al. (2019) (not to scale). Adapted from Faleiros et al. (2019).	18
3.7	Schematics of the nozzles used in the studies by Gibeau and Ghaemi (2018), Gibeau et al. (2019; 2020) (not to scale). Adapted from Gibeau et al. (2019).	18
3.8	Bubbling (<i>left</i>) and jetting (<i>right</i>) production regimes visualized by shadowgraphy. Adapted from Faleiros et al. (2019).	19
3.9	Change in HFSB coefficient of variation of the bubble diameter for bubbling and jetting regimes. Adapted from Faleiros et al. (2019).	19
3.10	Bubble size distribution for the jetting and bubbling regimes. Reproduced from Caridi (2018).	20
3.11	Production envelopes of Nozzle 3 (Figure 3.7, <i>right</i>), with arrows indicating nozzle orientation; vertically (top) and horizontally (bottom). Adapted from Gibeau et al. (2019).	21
3.12	Bubbling and jetting behaviour as a result of changes in operational parameters for the NLR nozzle (Figure 3.6, <i>left</i>). Adapted from Faleiros et al. (2019).	21
3.13	Production envelopes of Nozzles 1,2 and 3 (Figure 3.7), all in the vertical orientation. Adapted from Gibeau et al. (2019).	22
3.14	Variation of the Weber number with slip velocity. Reproduced from Faleiros et al. (2019).	23
3.15	Streamlines and HFSB trajectories in a NACA00012 stagnation flow. Reproduced from Kerho and Bragg (1994).	24
3.16	Comparison between DEHS, HFSB and AFSB trajectories in a stagnation flow in front of a cylinder. Adapted from Faleiros et al. (2018).	24
3.17	HFSB time response and Stokes number as a function of soap and helium flow rates, with $U_\infty = 30$ m/s and $L = 50$ mm. The linear fit is forced through the experimental neutral buoyancy condition. Reproduced from Faleiros et al. (2019).	25
3.18	HFSB time response as a function of particle diameter. Reproduced from Faleiros et al. (2019).	25
3.19	Light scattered by a bubble's surface. Reproduced from Macháček (2003).	26
3.20	Schematic illustration of glare points produced by scattering of parallel light rays. Adapted from Morias (2016).	26
3.21	Relation between scattered light intensity and HFSB diameter for a scattering angle of $\theta = 90^\circ$. Adapted from Caridi (2018).	27
3.22	Light scattering intensity as a function of observation angle. Adapted from Caridi (2018).	27
3.23	Bubble size scaling law for the nozzles displayed in Figure 3.7, including linear fit of the NLR nozzle. Reproduced from Gibeau et al. (2020).	28
3.24	Relation between flow rates and bubble diameter, for the nozzles displayed in Figure 3.7. Outlines in black represent the bubbling regime. Adapted from Gibeau et al. (2020).	28

3.25 Trends observed for HFSB particle size with flow rate and orifice diameter. Reproduced from Faleiros et al. (2019).	28
3.26 Model coordinate system for a for 90° scattering angle. Dimensions not to scale.	30
3.27 2D light ray scattering behaviour modelled via ray tracing.	30
3.28 Numerical 2D scattering intensity behaviour as a resulting of particle diameter scaling.	30
3.29 Detail of 2D light ray scattering behaviour	31
3.30 Intensity distribution of glare points in 3D with maxima indicated by red crosses. Reproduced from Morias (2016).	31
3.31 Overview of time-resolved 3D3C experiments in air at $U_\infty > 5$ m/s. 1: Pröbsting et al. (2013), 2: Violato et al. (2011), 3: Ghaemi and Scarano (2011), 4: Schröder et al. (2008), 5: Schneiders et al. (2016), 6: Kim et al. (2020), 7: Caridi (2018), 8: Caridi et al. (2015), 9: Caridi et al. (2016).	32
3.32 Measurement volume as a function of particle diameter for time-resolved experiments.	33
4.1 Experimental set-up of nozzle test bench, including camera (<i>left</i>) and laser (<i>right</i>).	37
4.2 Schematic of the test-set-up, not to scale.	37
4.3 Clamp for holding HFSB nozzle generators in place.	38
4.4 Schematic of the FSU and nozzle, not to scale.	38
4.5 Cross-sectional view of the *S2_O200 nozzle.	40
4.6 Calibration curve for BSF.	42
4.7 Calibration curve for air, of the S1 series nozzles.	42
4.8 Calibration curve for helium, of the S1 series nozzles.	42
4.9 Calibration curve for BSF	43
4.10 Calibration curve for air for S15, S2 and S3 nozzles.	43
4.11 Calibration curve for helium for S15, S2 and S3 nozzles.	43
4.12 Image pre-processing steps. Note that relative intensity between images changes. <i>Left</i> : Raw image with highlighted cropping region (<i>red</i>) and nozzle (<i>yellow</i>). <i>Middle</i> : Minimum background noise over three images. <i>Right</i> : Processed image, with 1x1 mm grid.	46
4.13 Peak sorting step on post-processed images with 1x1 mm grid. <i>Left</i> : Raw image. <i>Middle</i> : Initial peaks found at pixel accuracy. <i>Right</i> : Remaining 2D Gaussian interpolated peaks after the sorting phase.	47
4.14 Initial peak location with integer pixel accuracy.	47
4.15 2D Gaussian interpolated peak location.	47
4.16 Unimodal distribution of HFSB diameters for *S2_O200, test T21.6.	48
4.17 Bimodal distribution of HFSB diameters for *S2_O200, test T21.5.	48

4.18	Distribution of HFSB diameters for <i>S15_O150</i> , test <i>T11.1</i> whereby $CV_d = 3.4\%$	48
4.19	Distribution of HFSB diameters for <i>S15_O150</i> , test <i>T11.7</i> whereby $CV_d = 13.5\%$	48
4.20	2D intensity distribution of a large bubble	50
4.21	2D intensity distribution of small bubbles	50
5.1	Production regimes for series <i>S1</i> nozzles, whereby filled and empty markers indicate working and non-working conditions, respectively.	52
5.2	Production regimes for series <i>S15</i> nozzles, whereby filled and empty markers indicate working and non-working conditions, respectively.	52
5.3	Production regimes for series <i>S2</i> nozzles, whereby coloured and gray markers indicate working and non-working conditions, respectively.	53
5.4	Production regimes for series <i>S3</i> nozzle, whereby filled and empty markers indicate working and non-working conditions, respectively.	53
5.5	HFSB diameter variation as a function of Q_{Air} for all tested nozzles.	54
5.6	HFSB diameter variation as a function of Q_{Air} for the * <i>S2_O200</i> nozzle.	54
5.7	HFSB diameter variation as a function of Q_{He} for the * <i>S2_O200</i> nozzle. The black marks, slightly offset for clarity, indicate the expected values based on proportionality between Q_{He} and d_b	55
5.8	Normalized HFSB diameter variation as a function of Q_{Air}/Q_{He} for all tested nozzles.	56
5.9	Parameter definitions used in the model. Figure not to scale.	56
5.10	Normalized HFSB diameter variation as a function of Q_{Air}/Q_{He} for the * <i>S2_O200</i> nozzle, including approximated and fitted trend.	58
5.11	Normalized HFSB diameter variation as a function of Q_{Air}/Q_{He} including theoretical approximation.	59
5.12	Normalized HFSB diameter variation as a function of Q_{Air}/Q_{He} including theoretical approximation and data from the study by Faleiros et al. (2019) for the NLR type nozzle, shown in Figure 3.6 (<i>left</i>).	60
5.13	HFSB diameter disparity expressed as CV_d as a function of Q_{Air}/Q_{He}	61
5.14	Detailed nozzle performance for series <i>S1</i> nozzles	62
5.15	Detailed nozzle performance for series <i>S15</i> nozzles	63
5.16	Detailed nozzle performance for series <i>S2</i> nozzles	63
5.17	Bubble volume dependency on the production rate.	65
5.18	Variation of the production frequency with bubble diameter	65
6.1	Streamlines for sharp-edged and rounded orifices. Adapted from Cengel et al. (2016).	70
B.1	Code Flowchart.	73

List of Tables

2.1	Properties of commonly used PIV tracers for experiments in air.	12
3.1	Fluid properties for 20 °C at 1 atm. Reproduced from Faleiros et al. (2019).	17
3.2	Production variables for various nozzles.	18
4.1	Nozzle naming convention for geometrically scaled nozzles, including cross-sectional views with mm scaling grid.	39
4.2	Nozzle naming convention for orifice scaled S1 series nozzles, including cross-sectional views with mm scaling grid.	40
4.3	Overview of tested nozzles.	40
4.4	Test Matrix for nozzles with a scaling factor of 1.5, 2 and 3 and varying orifice sizes. . .	45
5.1	Theoretical minimum and maximum particle diameter for an ideally operating nozzle. . .	60
5.2	Minimum and maximum bubble diameter per nozzle for $CV_d < 13\%$	64
A.1	Test Matrix for P_{BSF} and P_{He} for nozzles with a scaling factor of 1.5, 2 and 3 and varying orifice sizes.	71
A.2	Conversion matrix Q_{Air} to P_{Air} per geometrical scaling factor.	72

List of Symbols

Greek symbols

δ_{99}	Boundary layer thickness	[m]
δL	Distance between successive bubbles	[mm]
δz	Depth of focus	[mm]
Δt	Pulse separation time	[s]
Δx	Particle displacement	[mm]
ΔZ	Measurement volume depth	[mm]
ρ	Density	[kg m ⁻³]
$\bar{\rho}$	Relative density	[-]
λ	Wavelength of a periodic wave	[nm]
λ	Bubble pitch	[mm]
μ	Dynamic viscosity	[kg s ⁻¹ m]
σ	Surface tension	[N m]
τ_0	Characteristic time	[s]
τ_p	Particle response time	[s]

Latin symbols

A_{mv}	Area of measurement volume	[m ²]
a	Speed of sound	[m s ⁻¹]
C	Tracer concentration	[particles/m ³]
CV_d	Coefficient of variation of the bubble diameter	[-]
D	Effective aperture	[mm]
d_B	Bubble diameter	[mm]
d_{diff}	Particle image diameter due to diffraction	[mm]
d_G	Glare point distance	[mm]
d_i	Image distance	[mm]
d_o	Orifice diameter	[mm]
d_o	Object distance	[mm]
d_p	Particle diameter	[mm]
d_s	Streamtube diameter	[mm]
d_τ	Particle image diameter	[mm]
E_{HFSB}	HFSB light scattering intensity	[J]
F_{AM}	Added-mass force	[N]
F_{FS}	Pressure force	[N]
F_{G-B}	Gravity-buoyancy force	[N]
F_H	History force	[N]
F_L	Traverse lift force	[N]
F_{QS}	Quasi-steady viscous drag force	[N]
f	Production frequency	[Hz]
f	Focal length	[mm]
$f_\#$	Numerical aperture	[-]
I	Light intensity	[W m ⁻²]
L_a	Distance to aperture	[mm]
L_o	Object distance	[mm]
M	Magnification factor	[-]
M	Mach number	[-]
m_p	Particle mass	[kg]
n	Index of refraction	[-]
n_{bub}	Number of bubbles	[-]
P	Pressure	[bar]
Q	Flow rate	[l h ⁻¹]
Re_D	Cylinder Reynolds number	[-]
Re_p	Particle Reynolds number	[-]
r_p	Particle radius	[mm]
St_k	Stokes number	[-]
u	Velocity	[m s ⁻¹]
u_{slip}	Slip velocity	[m s ⁻¹]
U_∞	Free-stream velocity	[m s ⁻¹]
V	Velocity	[m s ⁻¹]
\dot{V}	Flow rate	[l h ⁻¹]
V_b	Bubble volume	[mm ³]
v_{jet}	Jet velocity	[m s ⁻¹]
We_p	Particle Weber number	[-]

Subscripts

BFS	Bubble soap solution
exp	Experimental
f	Fluid
He	Helium
HP	Hagen-Poiseuille
p	Particle

List of Abbreviations

2D-2C	Two-Dimensional Two-Components
3D-3C	Three-Dimensional Three-Components
AFSB	Air-filled soap bubbles
BFS	Bubble fluid solution
CCD	Charge-coupled device
CMOS	Complementary metal oxide semiconductor
DEHS	Di-ethyl-hexyl-sebacat
DOF	Depth of field
DSR	Dynamic spatial range
DVR	Dynamic velocity range
FOV	Field of view
FSU	Fluid supply unit
HFSB	Helium-filled soap bubbles
Nd:YLF	Neodymium-doped yttrium lithium fluoride
PIV	Particle image velocimetry
ppp	Particles per pixel
PTV	Particle tracking velocimetry
rpm	rounds per minute

1

Introduction

The complexity and omnipresence of the inherently three-dimensional processes governing turbulence have been awakening the curiosity of researchers and scientists since the early 16th century. Turbulence dictates the fluid flow of blood within our veins, the weather via large-scale atmospheric and oceanic flows and the airborne transmission of diseases such as the recent SARS-CoV-2 virus. From an engineering perspective, accurately predicting the behaviour of fluid and gas flows results in more sustainable product solutions. Aerodynamicists are challenged within various industries such as automotive, aerospace and wind energy to analyse these complex flow phenomena. The growing demand to conduct large-scale, industrial wind tunnel experiments is not met by the experimental technique considered in this project, called Particle Image Velocimetry (PIV), due to limitations on the maximum size of the measurement domain.

PIV relies on the assumption that particles, which are introduced into the flow of interest, accurately track the fluid flow. The principle of the technique can be illustrated by the observation of a leaf floating on a river or moving through an autumn storm. Without being able to see the actual flow, tracing the movement of the leaf provides an insight into the motion of the flow. In PIV, advanced imaging devices are used to capture the motion of numerous tracer particles flowing through the measurement domain. High-powered lasers provide the energy required for the recorded images to have sufficient contrast between the image background and the light scattered by the tracers. The literature survey from Chapter 2 however, illustrates that adequate illumination is still the limiting factor in performing large-scale time-resolved PIV measurements. Increasing the laser power is a possible solution, but is often economically unfavourable. Other solutions such as traversing systems ([Nakagawa et al. 2016](#)) and robotic PIV ([Jux 2017](#)), combine multiple measurements into a large single domain. However, these fall short of the need for time-averaging the velocity fields and the increasing operational costs due to the time-consuming process of acquiring multiple sub-domains.

The third solution employs the quadratic scaling behaviour of the light scattering intensity with particle diameter to achieve larger measurement domains. The development of soap bubbles having a particle diameter of two orders of magnitude larger than conventional micron-sized tracers already enabled the upscale of measurement domains and lifted some of the restrictions of PIV for large-scale industrial applications. However, the limited size of these so-called helium-filled soap bubbles (HFSB) forms additional challenges for the application of PIV on a larger scale, as outlined in Chapter 3. Current HFSB equipped PIV systems are unable to study domains larger than the human body itself. For this reason, the flexibility of producing and scaling HFSB is investigated. The gathered knowledge will ultimately be used to fulfil the fundamental aim of this research project:

To increase the ratio of largest to smallest particle diameter of neutrally buoyant HFSB by analysing the experimental results of varying geometrical and operational parameters of a 3D printed nozzle developed by Delft University of Technology.

The current work leverages the advantages of flexible and accurate additive manufacturing techniques to produce and analyse the impact of geometrical changes on operational performance and HFSSB particle size. The state-of-the-art HFSSB nozzle generator developed by Delft University of Technology serves as a reference. To fulfil the aforementioned research objective, an experimental campaign is carried out. Focusing on the nozzle exit, the particle diameter can be derived from recordings of the bubbles produced by localising the light intensity peaks of individual glare points. The experimental arrangement and data processing procedures required for this are outlined in Chapter 4.

Existing literature has yet to establish a mathematical formulation of the particle diameter based on the operational and geometrical parameters. A theoretical model, describing the proportionality between the bubble diameter and operational parameters is presented in Chapter 5. The discussion of the results continues with an overview of the performance for each tested nozzle. Conclusions are drawn in Chapter 6, together with recommendations on further improvements for both the design of the HFSSB nozzle generators as well as the assessment procedure on the bubble diameter and future research.

2

Particle Image Velocimetry

The aim of this chapter is to provide the reader with a general guideline on the different components of a PIV system, as well as the key aspects in the choice of tracers and the result thereof. An overview of the different fields of research in which PIV is employed is presented first. Hereafter, the working principle of the technique is discussed. A significant portion of this chapter is devoted to the fluid mechanical and optical properties of tracer particles, which is followed by a description of commonly used tracers. The discussion is concluded by highlighting limitations in terms of measurement volume and describing the potential of a new type of tracer to up-scale the domain.

2.1. History of Applications

In the early 1980s, [Adrian and Yao \(1985\)](#) developed a technique to study the intricate structures of turbulence by visualizing and quantifying instantaneous velocity fields within a certain domain. This planar imaging technique was able to capture two velocity components within a two-dimensional domain (2D-2C). Particle Image Velocimetry (PIV) is nowadays a well-accepted and often used measurement technique in experimental facilities ([Scarano 2013a](#)). With technological advancements being made in both image acquisition techniques and illumination devices, accuracy and reliability have been greatly improved. Modern experimental fluid mechanics made a large step forward with the introduction of tomographic PIV by [Elsinga et al. \(2006b\)](#), enabling three-dimensional three-component measurements (3D-3C PIV) to measure the complete topology of turbulent structures.

While PIV was developed as a measurement technique for laboratory and research environments, its non-intrusiveness and potential to perform whole flow field analyses quickly triggered the attention of aerospace, automotive and wind energy industries which required the technique to be applied on a larger, industrial scale. Challenges of applying PIV to larger measurement domains ($> 1 \text{ m}^3$) include camera positioning and calibration, as well as particle tracing behaviour and post-processing ([Biwole 2009](#)). For volumetric measurements, the light intensity is inversely proportional to the required measurement volume thickness, posing a major bound on the use of tomographic PIV to large domains ([Scarano 2013a](#)).

The versatility of PIV can be emphasized by the wide variety of applications to obtain 2D and 3D velocity data in both industrial and laboratory environments. [Jux et al. \(2018\)](#) analysed the complex flow field around a full-scale replica of a professional cyclist. Large-scale testing has become increasingly valuable in automotive industries, especially in competitive sports whereby rapid development programs are required to stay ahead of the competition, such as Formula 1 ([Nakagawa et al. 2016](#)). PIV is also used in high-speed flows, such as the turbulence analysis of fundamental flows in supersonic ([Scarano 2008](#)) and hypersonic ([Oudheusden, van et al. 2006](#)) conditions. Furthermore, PIV has been employed

in turbomachinery (Uzol et al. 2003) and more recently in internal combustion flows (Mamaikin et al. 2020). PIV has also proven to be of value in bio-medical flows (Bakar et al. 2018). Lastly, advancements have been made to support computational fluid dynamics simulations through data assimilation, decreasing noise and increasing the resolution of the reconstructed velocity fields (Symon et al. 2017). Ample examples exist where PIV is used for flow field analysis (Figure 2.1), and the aforementioned overview is therefore by no means an all-inclusive summary of potential applications.

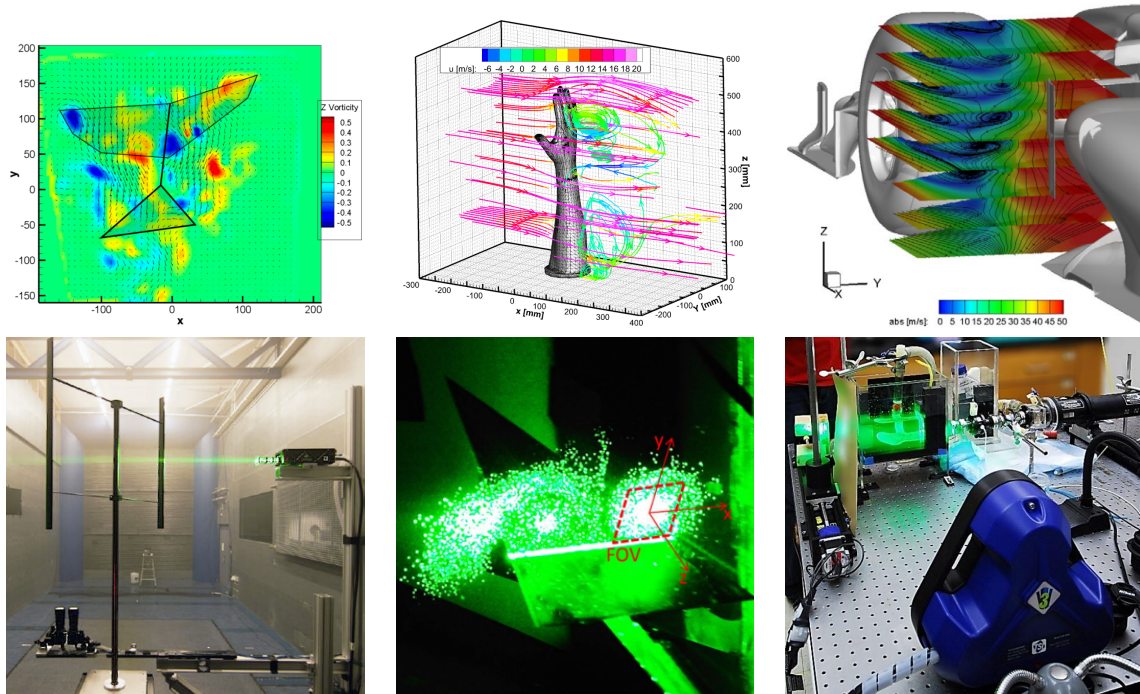


Figure 2.1: Various applications of PIV. From top left, CW: flapping-wing micro air vehicles (Herrero et al. 2018), full-scale swimmer's hand (Berg et al. 2019), F1 tire wake analysis (Nakagawa et al. 2016), near wake of a vertical axis wind turbine (Tescione et al. 2014), vortices over a delta wing (Caridi et al. 2017) and flow diagnostics in biomedical flows (TSI Incorporated 2019).

2.2. Working Principle

PIV relies on the tracking of tracer particles introduced upstream of the measurement domain by an imaging system. Within the measurement domain, a pulsed illumination source ensures sufficient contrast between the image background and the light scattered by the tracer particles. A camera captures the scattered light, which must therefore be in-focus with the illuminated measurement domain. An algorithm subsequently determines the displacement vector of the tracer particles between two successive images with a predefined separation time. This can be converted to a velocity vector field by basic kinematic relations. The working principle of a complete PIV system is schematically shown in Figure 2.2.

Depending on the seeding concentration inside the measurement domain, two varieties of particle tracking methods can be distinguished. PIV is used for higher seeding concentrations, where an ensemble of particles in an interrogation window is used for a cross-correlation analysis between image pairs. The resulting velocity vector is therefore a mean per interrogation window. In particle tracking velocimetry (PTV), individual tracer particles are tracked and subsequently used to reconstruct a velocity field. This is only possible for relatively low seeding densities. A schematic of both image processing techniques is illustrated in Figure 2.3.

The following sections will provide a more detailed description of the individual components of a PIV set-up.

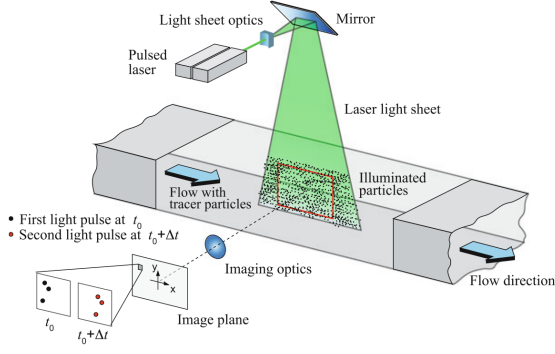


Figure 2.2: Overview of a PIV measurement set-up. Reproduced from Raffel et al. (2018).

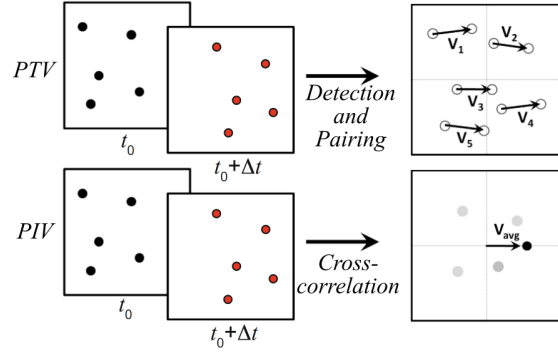


Figure 2.3: PIV and PTV image processing procedures. Adapted from Lynch (2015).

2.2.1. Imaging and Digital Image Recording

The measurement quality of PIV experiments depends on the imaging system which records the particles flowing through the domain of interest. The optical arrangement of a PIV system ensures that an image of the tracer particle is formed by means of a lens on the image sensor. The imaging system can be characterized by three parameters: image magnification M , focal length f and f-stop or lens aperture $f_{\#}$ (Scarano 2013a). Mathematically, they are expressed as:

$$M = \frac{d_i}{d_o}, \quad (2.1)$$

$$f = \frac{1}{d_i} + \frac{1}{d_o}, \quad (2.2)$$

$$f_{\#} = \frac{f}{D}. \quad (2.3)$$

Where the ratio between the image-lens distance d_i and object-lens distance d_o defines the magnification factor M of the imaging system. The focal length of the objective f is related via the thin-lens formula, which can be derived from a geometric analysis of tracing light rays for thin lenses. Lastly, the numerical aperture $f_{\#}$ is defined by focal length f and effective aperture D .

Crucial in PIV is that tracer particles are in focus throughout the measurement domain. The thickness of the volume Δz should therefore be equal to or smaller than the depth of focus δz , given by

$$\delta z = 4.88\lambda f_{\#}^2 \left(1 + \frac{1}{M}\right)^2, \quad (2.4)$$

where λ is the wavelength of light. The depth of focus, or focal depth, represents the region where particles are imaged with sufficient sharpness.

For small tracer particles of the order of several microns, the particle image diameter is mainly diffraction limited d_{diff} . With larger particles however, geometrical imaging dominates the imaging diameter. The particle image diameter d_{τ} , considering geometrical and diffraction imaging, can ultimately be defined as

$$d_{\tau} = \sqrt{(Md_p)^2 + d_{\text{diff}}^2}. \quad (2.5)$$

With the focus of this project on larger particles not limited by diffraction imaging, the reader is referred

to [Raffel et al. \(2018\)](#) for more information regarding the finite resolution of an optical system.

A digital image recording system is required to convert the light of the particle image to a digital signal, which can subsequently be read out by a computer. Such a system is composed of a rectangular array of photosensitive elements or pixels, which convert light into an electric charge. Depending on the requirements of the measurement, either a charge coupled device (CCD) or a CMOS (Complementary Metal Oxide Semiconductor) sensor is used. For high-speed measurements, where the acquisition frequency is in the order of 10 kHz, CMOS sensors are used. The analogue-to-digital signal conversion for this type of sensor is much higher, compared to a CCD ([Raffel et al. 2018](#)). Next generation CMOS sensors, named scientific CMOS sensors, outperform CCD and previous generation CMOS cameras by simultaneously featuring low readout noise, high frame rates, a high resolution and a large field-of-view. The low read-out noise allows the sensor to distinct between weak signals which is necessary in low light conditions.

2.2.2. Illumination

The choice of illumination devices for PIV experiments is governed by three main requirements. First, the light source must be strong enough to allow the scattered light of tracer particles to be detected by digital imaging devices. Secondly, the light source must emit light for a short duration of time so that moving particles are observed as dots rather than streaks of light. The third requirement is that the light must be shaped to only illuminate the particles which are in focus.

As a result, PIV commonly uses lasers as a source of illumination. Lasers produce highly collimated light beams that can be shaped into sheets of light by lenses. Lasers emit monochromatic light with a high energy density, which is unaffected by chromatic aberrations. An example of a typical laser used for PIV is a diode-pumped Nd:YLF laser emitting light at 10 to 50 mJ at repetition rates of 1 to 10 kHz, for a duration varying between 70 and 150 ns ([Caridi 2018](#)).

However, several factors decrease the intensity of the light scattered by the tracer particles, which will be described in more detail in Section 2.3.3. To counter the limiting energy density within a measurement domain, mirrors can be employed to reflect the laser light back in-itself. A single mirror arrangement, called a double-pass system, is presented in Figure 2.4. Typically, a gain factor of 1.5 in comparison to a single-pass configuration can be achieved. The use of double-pass illumination is described in the works of [Scarano and Poelma \(2009\)](#) and [Schröder et al. \(2013\)](#). Higher gains can be achieved by using a multi-pass illumination system, whereby the measurement domain is located between two opposing mirrors, reflecting the laser beam several times. Using the experimental set-up as shown in Figure 2.5, [Ghaemi and Scarano \(2010\)](#) were able to realize an amplification factor of 7. However, the use of reflective mirrors could pose additional challenges. First, the wind tunnel must be able to house the required equipment. Furthermore, unwanted reflections could hamper cross-correlation and therefore require additional post-processing due to the laser light originating from different directions.

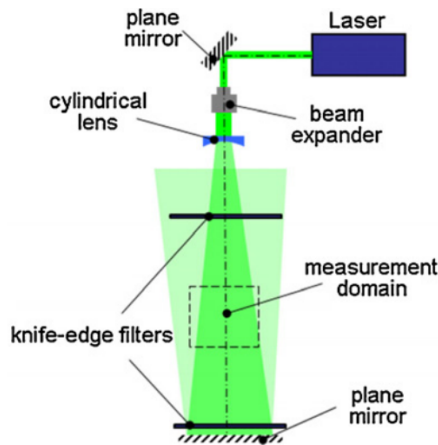


Figure 2.4: Schematic representation of a double-pass illumination arrangement. Reproduced from Scarano (2013a).

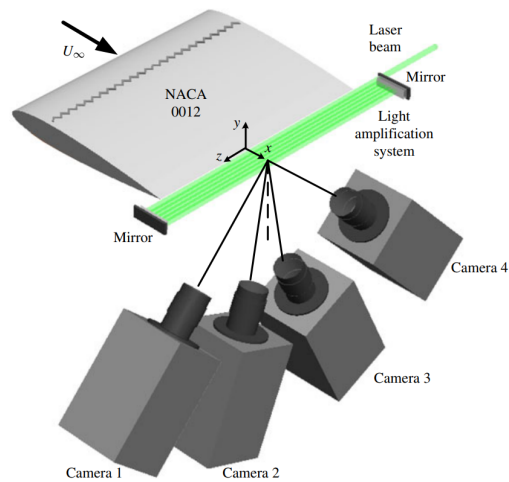


Figure 2.5: Three-dimensional overview of a multi-pass illumination system. Reproduced from Ghaemi and Scarano (2011).

2.2.3. Image Analysis

After capturing the motion of tracer particles by the imaging system, images are processed by a spatial correlation algorithm yielding the particle velocity. First, images are partitioned into smaller windows. For PIV, an ensemble of tracers is used to determine the local velocity vector within the interrogation window. Hereafter, the cross-correlation function ϕ between successive image pairs is computed, yielding a peak which location corresponds to the average displacement of the particles in the interrogation window. The highest peak ϕ_1 indicates the most probable average particle displacement, measured from the origin. Particle displacement is measured by an integer number of pixels, but its accuracy can be enhanced by sub-pixel interpolation methods. The result of the cross-correlation analysis can subsequently be divided by the known time separation between laser pulses and the scaling, yielding the velocity (Scarano 2013b). Figure 2.6 illustrates the image analysis procedure between two interrogation windows $I(x, y, t)$ and $I'(x, y, t + \Delta t)$.

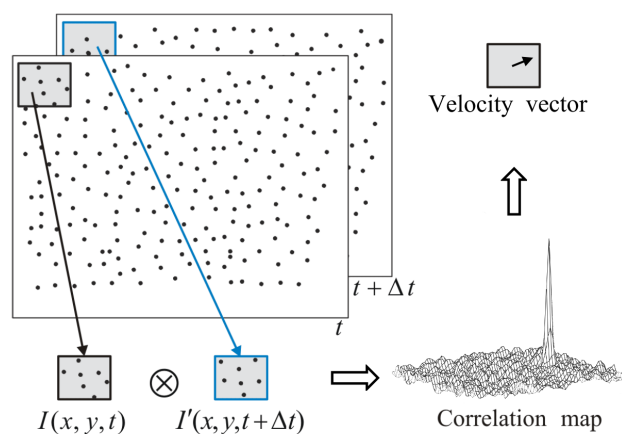


Figure 2.6: Image analysis operating sequence. Adapted from Scarano (2013b) and Raffel et al. (2018).

For lower particle concentrations it is not possible to derive the velocity via cross-correlation of an ensemble of tracers. Particle tracking velocimetry, briefly introduced in Section 3.2, provides the opportunity to process images and derive the velocity field for lower particle concentrations. Tracking individual particles also enhances the local resolution of the velocity and acceleration field, which is otherwise impossible for spatially averaged interrogation cells. For volumetric measurements, state-of-

the-art particle tracking techniques rely on the 2D particle detection from the light intensity distributions and posterior 3D triangulations. The technique, introduced by [Schanz et al. \(2016\)](#) as Shake-the-box, predicts and reconstructs particle trajectories from information of preceding images, reducing computational effort and measurement uncertainties.

According to [Raffel et al. \(2018\)](#), the overall success of particle velocimetry techniques can be mainly attributed to the unique ability to analyse instantaneous velocity vectors at numerous locations within the measurement domain. With the use of relatively small tracer particles, the resulting resolution allows for the analysis of coherent structures in a wide range of scales. [Adrian \(1991\)](#) concludes that PIV is, therefore, a powerful tool for the analysis of structural elements in turbulent flows.

Both particle velocimetry techniques are regarded as non-intrusive since it does not require any instrumentation inside the test section such as hot-wire probes or pressure tubes. These instruments cannot be used to analyse the boundary layer or high-speed flows with shock waves as the presence of probes or tubes will affect flow dynamics. Due to the use of an optical system, optical access to the test section is required. This poses challenges to the use of PIV in industrial facilities, where the test section often cannot be adapted to house a complex optical arrangement of cameras and mirrors. Lastly, to capture the airflow dynamics accurately, tracer particles must follow the local motion of the flow faithfully which requires a careful assessment of tracer capabilities, as will be described in the following section.

2.3. Flow Seeding Particles

The particle displacement obtained from successive image pairs provides knowledge of the particle motion in time. To quantify velocity information of turbulence, PIV relies on the assumption that tracer particles accurately follow the instantaneous motion of the flow of interest. A crucial aspect to obtain accurate and reliable data is to minimize the discrepancies associated with this assumption. The following sections will therefore serve as a general basis upon which familiarity with the requirements of seeding particles can be gained.

2.3.1. Particle Dynamics

To gain a better insight into the forces acting on a tracer, particle dynamic equations can be modelled for spherical particles according to Newton's second law of motion. This law pertains to the acceleration $d\mathbf{u}_p/dt$ of an object with mass m_p due to an unbalance of forces \mathbf{F}_i acting on the particle.

$$\mathbf{F}_{G-B} + \mathbf{F}_{QS} + \mathbf{F}_H + \mathbf{F}_{AM} + \mathbf{F}_{FS} + \mathbf{F}_L = m_p \frac{d\mathbf{u}_p}{dt} \quad (2.6)$$

The individual terms in Equation (2.6) are the gravity-buoyancy force \mathbf{F}_{G-B} , quasi-steady viscous drag force \mathbf{F}_{QS} , history force \mathbf{F}_H , added-mass force \mathbf{F}_{AM} , pressure force \mathbf{F}_{FS} and transverse lift force \mathbf{F}_L ([Adrian and Westerweel 2011](#)). Equation (2.6) is examined for a sphere in Stokes flow, i.e. where the particle Reynolds number is lower than unity by [Maxey and Riley \(1983\)](#). Based on this work, [Mei \(1996\)](#) extensively discussed Equation (2.6) and proposed a solution for a finite particle Reynolds number Re_p , as defined by Equation (2.7).

$$Re_p = \frac{\rho_f |u_p - u_f| d_p}{\mu_f} \quad (2.7)$$

The relation for particle Reynolds number is based on a particle with radius d_p moving at velocity u_p through a fluid of density ρ_f and dynamic viscosity μ_f with local fluid velocity u_f . When larger tracers are used in combination with higher operating flow velocities, the particle Reynolds number is in the order of 100. In that case, the drag of a sphere must be corrected for, since the drag approximated by Stokes' law is only accurate for small Reynolds numbers, see Figure 2.7.

Schiller and Naumann (1933) adapted the quasi-steady drag term \mathbf{F}_{QS} in Equation (2.6) to include an additional correction term ϕ , which is based on the particle Reynolds number as presented in Equation (2.8). The correction is accurate within 5% of the actual drag coefficient as presented by Figure 2.7, up to a Reynolds number of 800. For a more elaborate review of the individual terms in Equation (2.6), the reader is referred to Morias (2016).

$$\phi = 1 + 0.15Re_p^{0.687} \quad (2.8)$$

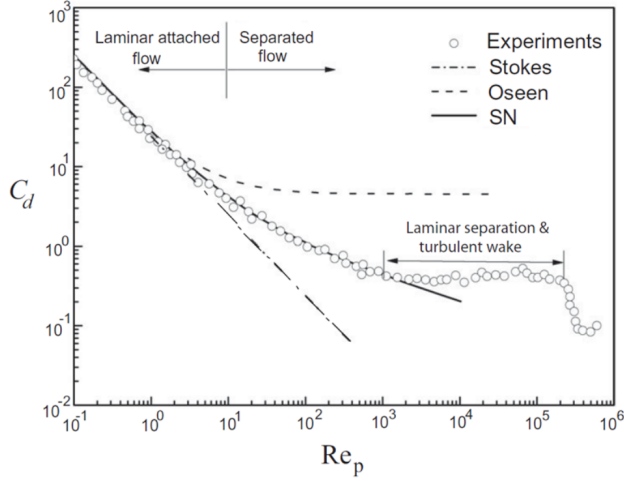


Figure 2.7: Particle drag coefficient for finite particle Reynolds number Re_p , modelled after Stokes, Oseen and Schiller and Neumann (SN). Reproduced from Marshall and Li (2014).

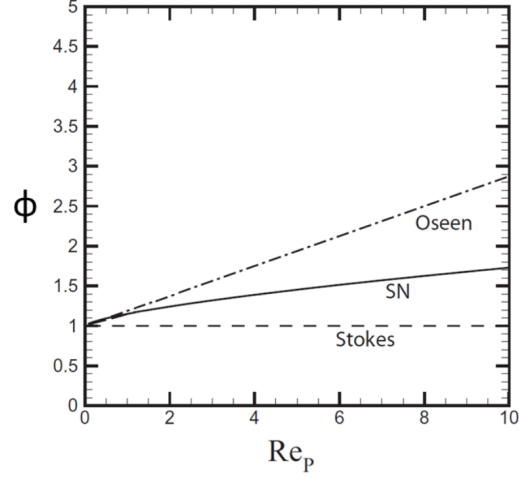


Figure 2.8: Drag correction term ϕ for finite particle Reynolds number Re_p , modelled after Stokes, Oseen and Schiller and Neumann (SN). Adapted from Marshall and Li (2014).

2.3.2. Tracer Fidelity

As previously mentioned, PIV relies on the generalisation that the instantaneous local velocity of a fluid can be derived from the movement of flow seeding particles. The validity of this assumption is evaluated and quantified in terms of the particle response time and slip velocity u_{slip} . Using the equation of motion for spherical particles in the absence of external forces (gravitational, centrifugal and electrostatic), Melling (1997) argued that a particle's tracking capability depends only on the shape, diameter d_p and density ρ_p of the particle, as well as density ρ_f and viscosity μ_f of the surrounding fluid. Equation (2.6) for near neutrally buoyant tracer particles is derived by neglecting buoyancy effects, which are assumed to be small compared to the fluid flow motion $D\mathbf{u}/Dt$. Additionally, the particle acceleration $d\mathbf{u}_p/dt \approx D\mathbf{u}/Dt$ due to the particle's near neutrally buoyancy. With the quasi-steady viscous drag and pressure force obtained from Mei (1996) remaining, Equation (2.6) simplifies to

$$\mathbf{F}_{FS} + \mathbf{F}_{QS} = m_p \frac{d\mathbf{u}_p}{dt}, \quad \text{with} \quad (2.9)$$

$$\mathbf{F}_{QS} = 6\pi\mu_f \frac{d_p}{2} \mathbf{u}_{slip}, \quad \text{and} \quad (2.10)$$

$$\mathbf{F}_{FS} = \frac{4}{3}\pi \left(\frac{d_p}{2}\right)^3 \rho_f \frac{D\mathbf{u}}{Dt}. \quad (2.11)$$

Equating the above relationships and substituting $m_p = \rho_p\pi/6d_p^3$ results in:

$$(\rho_p - \rho_f) \frac{d\mathbf{u}_p}{dt} = \frac{18\mu_f}{d_p^2} \mathbf{u}_{slip} \quad (2.12)$$

Conclusively, Equation (2.13) relates the slip velocity for small particles and small relative velocity, where the particle Reynolds number is lower than unity so that Stokes flow regime can be assumed.

$$\mathbf{u}_{\text{slip}} = \mathbf{u}_p - \mathbf{u}_f = d_p^2 \frac{(\rho_p - \rho_f)}{18\mu_f} \frac{d\mathbf{u}_p}{dt} \quad (2.13)$$

The discrepancy between the surrounding fluid u_f and particle velocity u_p is illustrated in Figure 2.9. To minimise the slip velocity and to approach ideal particle tracing behaviour, either the neutral buoyancy condition $\rho_f \approx \rho_p$ must be approached or the particle acceleration term du_p/dt must be zero. The latter condition is purely theoretical, as this flow condition is insignificant to aerodynamics. As the slip velocity scales quadratically with the particle diameter, its size should be minimized to favour tracing fidelity.

The analytical solution for the first-order ordinary differential equation given in Equation (2.13) to a step change is a single exponentially decaying function with characteristic time τ_0 , given by

$$\tau_0 = \frac{(\rho_p - \rho_f)d_p^2}{18\nu_f\rho_f}, \quad (2.14)$$

which is used to analyse the response time of a particle for $Re_p < 1$. τ_0 remains a constant value while valid in the Stokes regime since it is only dependent on fluid and particle properties. However in PIV, Re_p is often higher than unity and ρ_f may approach ρ_p . It is, therefore, necessary to define a generalized time constant which accounts for the effect of high finite Reynolds numbers and the density ratio with the correction term ϕ and relative density $\bar{\rho}$ given by $(\rho_p - \rho_f)/\rho_f$ (Adrian and Westerweel 2011):

$$\begin{aligned} \tau_p &= \frac{\bar{\rho} - 1}{\bar{\rho}} \frac{\tau_0}{\phi} \\ &= \frac{\bar{\rho} d_p^2}{18\nu_f \phi}. \end{aligned} \quad (2.15)$$

Figure 2.10 illustrates the definition of the particle response time, which can be interpreted as the required time of the particle velocity to reach 63% of the initial step change ΔU_{1-2} . Comparing Equations 2.13 and 2.15 results in an additional relation for the particle time response:

$$\tau_p = \frac{u_p - u_f}{\frac{du_p}{dt}}. \quad (2.16)$$

The choice of tracer particles depends on the type of flow under investigation. Knowledge about the time scale of the flow τ_t must therefore be incorporated to assess flow tracing capabilities. By normalising the particle response time with this time scale, the Stokes number is created:

$$St_k = \frac{\tau_p}{\tau_t}. \quad (2.17)$$

In the limit of Equation (2.17) when $St_k \rightarrow 0$, particles act as ideal flow tracers. Research on the motion of particles showed that for high Reynolds number flows where a large range of scales is present, the condition $St_k < 0.1$ yields acceptable flow tracing capabilities with errors $< 1\%$ (Samimy and Lele 1991, Tropea et al. 2007). The flow time scale can be estimated by performing dimensional analysis. Typically, $\tau_s = \delta_{99}/U_\infty$ for boundary layer flows. In experiments involving stagnation flow in front of a

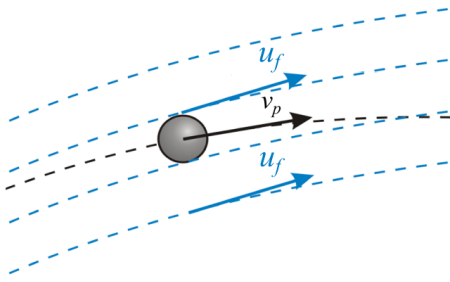


Figure 2.9: Particle slip velocity. Reproduced from Scarano (2013b).

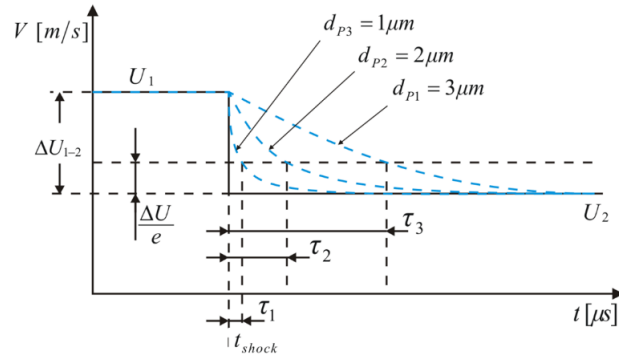


Figure 2.10: Particle lag after a velocity step change. Reproduced from Scarano (2013b).

cylinder, which is commonly used to determine the particle response time, the flow time scale is defined as the ratio between the cylinder diameter D and free-stream velocity U_∞ (Faleiros et al. 2019, Kerho and Bragg 1994, Scarano et al. 2015). The slip velocity is subsequently derived by subtracting the velocity field determined by the tracer of interest from the reference velocity field obtained by tracers with a known accuracy, such as micron-sized particles.

2.3.3. Optical Characteristics

The aforementioned analysis highlights the fluid-mechanical requirements for tracer particles. An effective way to minimise the particle response time is to decrease the particle diameter. However, opposing requirements arise when analysing the light scattering characteristics of particles which necessitate larger diameters instead of smaller.

The scattering amplitude per particle size range is defined by the Mie parameter $x_M = \pi d_p / \lambda$, with particle diameter d_p and wavelength of the incident light given by λ . Three scattering ranges are defined: Rayleigh ($x_M < 1$), Geometrical Optics ($x_M > 90$) and the intermediate-range called the Mie scattering regime, see Figure 2.11. For tracers with a diameter in the order of a micrometre, light is scattered according to Mie's scattering theory (Mie 1908). The dependence of the scattering function on the scattering angle, defined as the angle between the observer and the illumination source, is presented in Figure 2.12. It shows that it is advantageous to record forward scattered light. From a practical point of view, however, optical access is often limited which prohibits the placement of a camera system behind the light source and the domain of interest. Therefore, PIV experiments are commonly conducted at 90 degrees scattering angle where the scattering amplitude is minimal. This negatively influences the signal-to-noise ratio. The angular distribution and peak intensity is only dependent on the particle size and is independent of parameters such as surface material Caridi (2018).

For larger tracers such as soap bubbles (HFSB), $x_M \approx 1800$ and the scattered light intensity is governed by geometrical optics. Figure 2.11 shows that in this range, particle scattering intensity is highest, and the scattering intensity is proportional to $\approx d_p^2$. Doubling the particle diameter is thus substantially more effective than doubling the amount of laser light.

Illuminating a large domain requires the use of lenses to distribute laser light, causing the energy density to drop. More specifically, the scattered light intensity is inversely proportional to the depth of a three-dimensional measurement volume. In addition to the limiting energy density, the large depth of field as compared to two-dimensional experiments requires a small optical aperture to ensure all particles within the domain are in focus. With the aperture limiting the amount of light passing through, a small aperture further decreases the amount of light reaching the camera sensor. Lastly, increasing the observation distance follows a quadratic decay in light scattering intensity Caridi (2018). Acquiring data within a three-dimensional domain, therefore, requires the use of expensive high powered lasers. The maximum attainable light intensity is currently regarded as the bottleneck in the process of up-scaling

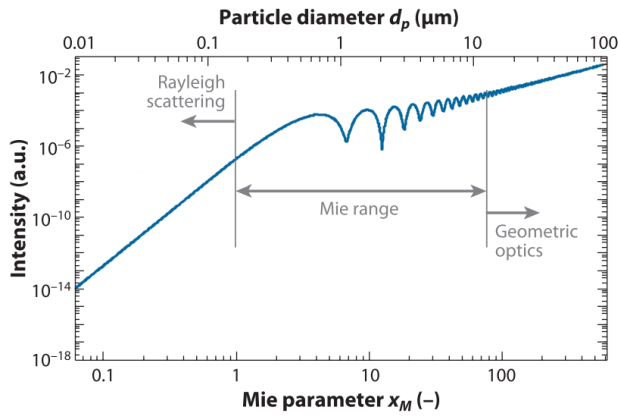


Figure 2.11: Scattering intensity and the relation with the Mie parameter for a scattering angle of 90° . Adapted from Tropea (2011).

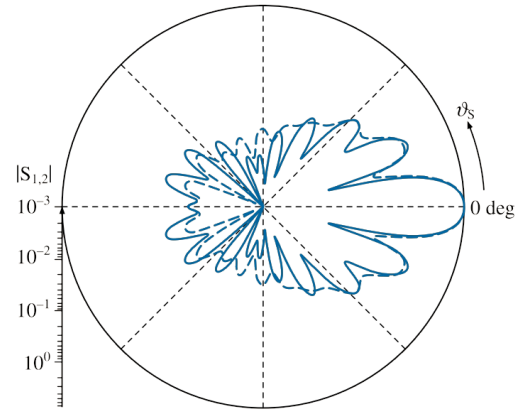


Figure 2.12: Scattered light intensity distribution as a function of the scattering angle at $x_s = 10$. The solid line represents perpendicular polarization, parallel polarization is represented by the dashed line. Adapted from Tropea et al. (2007).

measurement volumes Scarano (2013a).

2.3.4. Tracer Types

It is evident that the choice of tracers for a particular experiment is based on one hand by fluid mechanical characteristics and on the other hand by the optical properties. To use PIV in a wide range of applications, tracers with various mechanical and optical properties are required. For liquid flows, selecting the proper tracer to achieve adequate flow tracing characteristics is less challenging due to the higher density and viscosity of the fluid. However, in air flows, tracers particles which are much heavier than air are commonly used. Therefore, much smaller particles are required to maintain an adequate slip velocity between the surrounding fluid and particle. For high-speed transonic and supersonic flows, the occurrence of shock-waves poses additional challenges in the choice of tracers Oudheusden, van et al. (2006). This causes particles to travel at different velocities than that of the surrounding fluid, hence decreasing reliability and accuracy of the resulting velocity vector field. An overview of typically used particles in PIV experiments and their properties is given in Table 2.1.

Table 2.1: Properties of commonly used PIV tracers for experiments in air.

Particle	ρ_p [km/m^3]	d_p [μm]	τ_p [μs]	Reference
HFSB	≈ 1.2	300-600	10-20	(Faleiros et al. 2019)
DEHS	1000	1-3	2	(Kähler et al. 2002)
Olive oil	1000	3	22.5	(Melling 1997)
Hollow glass	2600	1.7	22.6	(Melling 1997)
TiO ₂	3500	0.02	0.4-3.7	(Ragni et al. 2011)
Al ₂ O ₃	3970	0.3	20-28	(Urban and Mungal 2001)

The opposing optical and fluid mechanical requirements of tracers call for careful consideration of the choice of particles. Additional requirements include health and safety aspects, which must be taken into account. Substances should not be toxic when deposited in the lungs. Additionally, particles should not cause corrosion or reactions to other components of the test facility and tracer residue and the subsequent contamination should be minimal. Therefore, naturally evaporating substances are preferred. Lastly, in the production of tracers, a mono-disperse size and density distribution is desired to minimize errors in the velocity vector algorithm, as explained in Section 2.3.2 (Tropea et al. 2007).

2.4. Seeding Concentration & Measurement Spatial Resolution

Tracer concentration ultimately governs the spatial resolution of the resulting data. For PIV, an ensemble of particles that are tracked within a certain interrogation box are used to determine the average displacement. [Adrian \(1986\)](#) therefore argued that the spatial resolution of the velocity field is equal to the size of the interrogation window in the fluid. Within the interrogation box, between 5 and 10 particles are required to perform cross-correlation between image pairs ([Scarano 2013a](#)). By tracking individual particles, as done in PTV, the spatial resolution can be enhanced to the theoretical limit of the maximum possible seeding concentration produced by the seeding generator. This limit, however, ignores all aspects of the accuracy with which a particle's displacement is derived ([Adrian 1997](#)). Beyond a certain number of particles per pixel (ppp), image contrast decreases due to the limited optical transmission of the flow of interest. The reader is referred to [Elsinga et al. \(2006a\)](#) for more information regarding the accuracy of particle reconstruction and the accompanying limit of seeding density.

[Adrian \(1997\)](#) defined a ratio of the largest to smallest resolvable flow structures, called dynamic spatial range (DSR). The DSR dictates the ability of a particular PIV set-up to measure small-scale variations embedded within the motion of larger scales. A high DSR is required to study the wide range of scales present in boundary layer development and turbulence. Tomographic PIV experiments typically have a DSR ranging from 20 to 30 ([Caridi 2018](#)). According to [Caridi et al. \(2015\)](#), DSR can be related to the number of tracers per unit volume for a given particle velocimetry system. The number of tracers within the region of interest C depend on the production rate f of the emitter, which is related via

$$C = \frac{f}{A_{mv}u_{\infty}}, \quad (2.18)$$

where the tracers are travelling with a free-stream velocity u_{∞} through a cross-section A_{mv} of the region of interest. Achieving a high production rate is, therefore, crucial to obtain a DSR to adequately resolve a large range of flow scales.

2.5. Measurement Domain

Despite advancements in both image acquisition techniques and illumination devices, PIV is predominantly used in research and academic environments. The use of 3D-3C PIV in a large industrial scale is limited due to the size of the maximum attainable measurement domain by this technique.

Section 2.3.3 described that the scattered light intensity increases with the square of the particle diameter. Before the development of larger tracer particles such as soap bubbles (see Table 2.1), measurement volumes of tomographic PIV experiments in air with micron-sized particles did not commonly exceed a tenth of a litre [Scarano \(2013a\)](#). In the first 3D-3C PIV experiments conducted by [Elsinga et al. \(2006b\)](#), a measurement volume of $3.5 \times 3.5 \times 0.7 = 8.6 \text{ cm}^3$ was used to analyse a ring vortex flow. Subsequent tomo-PIV experiments by [Schröder et al. \(2008\)](#), [Ghaemi and Scarano \(2011\)](#) and [Bomphrey et al. \(2012\)](#) did not exceed 20 cm^3 . [Staack et al. \(2010\)](#) investigated coherent structures of a free turbulent jet in a volume as large as $5.0 \times 5.0 \times 2 = 50 \text{ cm}^3$. Only in the works of [Fukuchi \(2012\)](#) and [Henningsson et al. \(2015\)](#), measurement volumes exceeded 1000 cm^3 , whereby the latter analysed wake deformation of a desert locust in a $20 \times 24 \times 5 = 2400 \text{ cm}^3$ volume. However, the limited scattering intensity of these particles required the use of complex multi-camera set-ups to realise the desired field of view and high powered lasers with a pulse energy of 1 J/pulse to illuminate the domain. To put this in perspective, time-resolved experiments commonly require high-speed Nd:YLF lasers with approximately 1-10 mJ/pulse. For non-time-resolved measurements, dual-cavity Nd:YAG lasers having a pulse energy of 200 mJ/pulse are sufficient for most applications [Scarano \(2013a\)](#). This highlights that the use of micron-sized particles for large-scale analyses is not suitable due to the required energy density.

A possible method to circumvent the limited laser energy capacity is to mount an entire PIV system

along a traversing rail or robotic arm. These traversing and robotic systems, as displayed in Figure 2.13 and Figure 2.14 respectively, have been extensively used due to their ability to measure multiple planes without the need for calibrations between measurements. These image planes can either be studied to obtain information of the out-of-plane component as conducted by [Nakagawa et al. \(2016\)](#), or can be stitched together to form a single data set as shown in the work of [Tescione et al. \(2014\)](#) and [Jux \(2017\)](#).

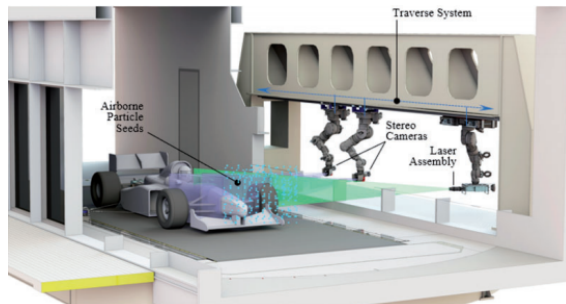


Figure 2.13: Traversing stereoscopic PIV system within a Formula One wind tunnel. Reproduced from [Senft and Gillan \(2019\)](#).

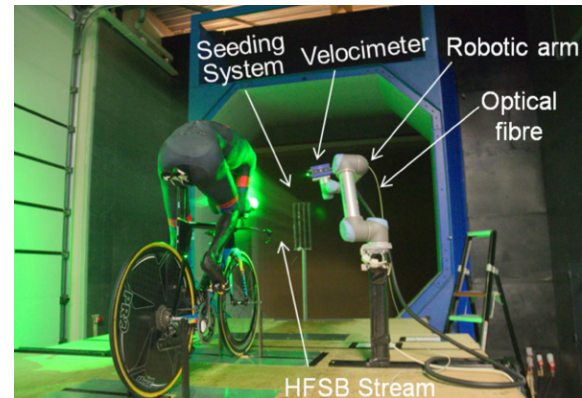


Figure 2.14: Robotic Coaxial Volumetric Velocimetry on a full-scale cyclist. Reproduced from [Jux et al. \(2018\)](#).

A second solution has been the development of soap bubbles having a particle diameter of two orders of magnitude larger than conventional micron-sized tracers. These tracers enabled the upscale of measurement domains, lifting some of the restrictions of PIV for large-scale industrial applications. However, the limited flexibility in the production of these so-called helium-filled soap bubbles forms additional challenges for the application of PIV on a larger scale. The use of helium-filled soap bubbles in PIV experiments and its application will therefore be treated in-depth in the following chapter.

3

Use and Scaling of HFSB

As described in the previous chapter, limitations on the available laser energy density within a large three-dimensional volume triggered the development of larger tracers. These tracers scatter more light due to the increased particle diameter. However, fluid mechanical properties of large particles and flow tracing accuracy requires the use of particles with a comparable density as air. The use of helium-filled soap bubbles (HFSB) is a viable solution, which will be discussed elaborately in the following chapter. It will ultimately highlight the need for up-scaling HFSB, which is the aim of this research project.

In the first part, a brief overview of the development and use of HFSB as tracer particles is presented. This is followed by a synopsis of the working principle of the generation of HFSB. The crucial aspects required for high accuracy PIV measurements, as introduced in the previous chapter, will be applied to the application of HFSB. This includes a description of one of the promising features of HFSB, the high scattering intensity. Hereafter, the need for up-scaling HFSB will be highlighted, which is the aim of this research project. Section 3.3 then focuses on the various designs of the bubble generator. A detailed characterization of the operating conditions is presented, along with an overview of the parameters that govern the operating condition in Section 3.4. This survey will then discuss the current body of knowledge regarding the scaling of HFSB. A critical review of the described studies concludes this chapter.

3.1. History of applications

Using soap bubbles to analyse the motion of air requires a lighter-than-air gas to compensate for the mass of the sphere and to approach the neutrally buoyant condition. Use of this technique can be traced back to the work of [Lock \(1928\)](#). In this work, it was reported that H.C. H. Townend was the first to use bubbles filled with coal gas as flow tracers to study a propeller flow field. Hydrogen was later used in the study of [Redon and Vinsonneau \(1936\)](#), describing the application of soap bubbles in a wind tunnel environment. Additional research in the production of helium-filled soap bubbles, roughly 3 mm in diameter, was done by [Hale et al. \(1971\)](#). Authors report that “this device was initially employed with remarkable success to visualize the motion of the wind through a field of crops” (p. 1), which is presented in Figure 3.1.

There is ample literature describing the use of HFSB for flow visualization. Early experiments include the observation of flows around parachutes by [Pounder \(1956\)](#) and [Klimas \(1973\)](#) and the study of tip vortices of airfoils and rotor blades [Hale et al. \(1971\)](#). Furthermore, neutrally buoyant soap bubbles have been employed in the analysis of combustor flows in gas turbine engines ([Rhode 1981](#)) and engine cylinders ([Kent and Eaton 1982](#)). The application of HFSB has been mostly limited to qualitative measurements due to the lack of research on their aerodynamic performance. This was first

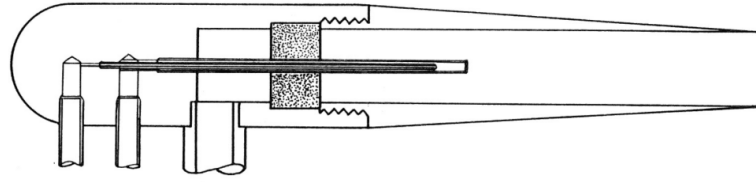


Figure 3.1: First commercially available HFSB nozzle generator. Reproduced from Hale et al. (1971).

addressed by Kerho and Bragg (1994), investigating the measurement uncertainty of HFSB as flow tracers. By experimentally assessing HFSB trajectories, a deviation was reported from the theoretical streamlines in the stagnation region in front of an airfoil (Figure 3.15). The uncertainties were deemed to be unacceptable as a result of difficulties in the generation of neutrally buoyant particles.

Henceforth, HFSB have been mainly used for qualitative research in convective flows where velocities remain relatively low (<1 m/s). For such flows, fluid accelerations will be negligible, hence only marginally affecting the slip velocity for bubbles deviating from the neutral buoyancy condition. Flow fields within a ventilated test room (Müller and Renz 2000) and a heat exchanger intake (Müller et al. 2001) were analysed using particle streak tracking (PST) to measure all three air-flow velocity components in a plane. Additional low-speed tests in a full-scale double aisle aircraft cabin mock-up by Bosbach et al. (2009) provided sufficiently accurate data needed to validate Computational Fluid Dynamics simulations. In the work of Kühn et al. (2011), the concept of using HFSB tracers for quantitative measurements in large-scale experiments was re-established, by highlighting that calibration errors remain small (<0.1 pixels) for a large-scale tomographic PIV system. Subsequent research by Scarano et al. (2015) revealed that HFSB tracers can be utilised for quantitative velocimetry in wind tunnel experiments by using sub-millimetre bubbles. This recommendation, in contrast to conclusions drawn earlier by Kerho and Bragg (1994), can be mainly attributed to the use of smaller tracers and more refined control of helium, air and soap flow rates to ensure that the neutral buoyancy condition is met.

This eventually triggered the use of HFSB as tracers for quantitative PIV in experimental facilities, such as the aerodynamic optimization in competitive cycling (Jux et al. 2018, Sciacchitano et al. 2015) and flow field studies in automotive (Kim et al. 2020), aerospace Czyż et al. (2020) and wind energy industries Brownstein et al. (2019). Other applications include turbulence studies with insects Henningsson et al. (2015), wall-bounded turbulence Faleiros et al. (2018) and vortex core velocimetry Caridi et al. (2017).

3.2. Working Principle

HFSB are produced by a bubble generating nozzle. The current state-of-the-art generators, called orifice-type nozzles, were first introduced by Okuno et al. (1993). They house three coaxial channels, which provides the helium, bubble fluid solution (BFS) and air required to produce bubbles (see Figure 3.2). The outer air and centre helium channels are used to draw a soap filament from the middle supply channel, forming an annular jet consisting of helium surrounded by soap. During this process, the thickness of the soap film decreases and is forced through the nozzle opening, called the orifice. The subsequent formation of bubbles is analogous to the behaviour of water flowing from a faucet. For low flow rates, droplet formation occurs at the exit. By increasing the water flow, a liquid jet starts to form, eventually breaking up into droplets. For higher flow rates, inertial forces start to overcome the surface tension forces. Jet break-up into droplets is then governed by the Rayleigh-Plateau instability (Ambravaneswaran et al. 2004, Clanet and Lasheras 1999), whereby inter-facial tension acts as to minimise the total surface area of the annular soap jet (Utada et al. 2005).

The production of HFSB is controlled by a fluid supply unit (FSU). It consists of a system of pressure valves to regulate the flow rates of air, helium and BFS to the nozzle, illustrated in Figure 3.3. Pres-

surized air and helium can be directly controlled, whereas the bubble fluid solution is pressurized by compressed air. The properties of the fluids used for the production of HFSB can be found in Table 3.1.

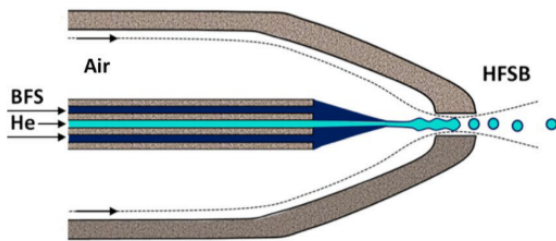


Figure 3.2: Schematic of an orifice-type nozzle used to produce HFSB. Adapted from Faleiros et al. (2018).

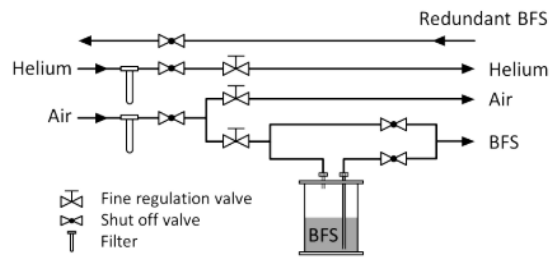


Figure 3.3: Schematic illustration of the fluid supply unit (FSU). Reproduced from Morias (2016).

Table 3.1: Fluid properties for 20 °C at 1 atm. Reproduced from Faleiros et al. (2019).

Variable	Air	Helium	BFS
Density ρ [kg/m ³]	1.20	0.17	1124
Dynamic viscosity μ [Pa s]	$1.8 \cdot 10^{-5}$	$2.0 \cdot 10^{-5}$	$8.0 \cdot 10^{-3}$
Surface tension σ [mN/m]	-	-	27.5

3.3. Production Methods

Before the development of the orifice-type nozzle by Okuno et al. (1993), aerodynamic flows were visualized by pitot-type nozzles. For the latter nozzle, the focusing gas is released behind the soap exit. For the orifice-type nozzle, air is used as a focusing gas to force the soap and helium filament through an orifice. It was reported that with this arrangement, a tenfold increase in bubble production frequency could be achieved with regard to the pitot-type nozzle. Furthermore, it was reported that particle diameters could be controlled by the orifice diameter and the gas flow rates. Figure 3.4 shows a cross-sectional schematic of both nozzle types.

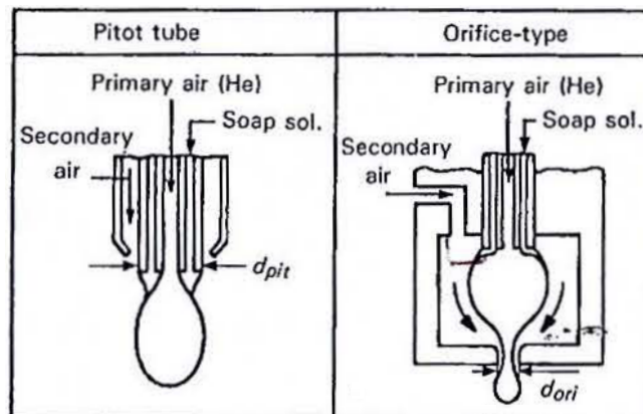


Figure 3.4: Schematic sectional comparison between pitot- and orifice-type nozzles. Reproduced from Okuno et al. (1993).

Developments by the German Aerospace Center (DLR) led to an improved version of the orifice-type generator, which is presented in Figure 3.5 hereafter referred to as the DLR nozzle. The first use of the DLR nozzle was reported by Bosbach et al. (2009). It was capable of producing 0.23 mm bubbles in diameter at an estimated production frequency of 200,000 bubbles/s.

Recent developments in 3D printing technologies enabled the production of nozzles without the use of metal machined parts, decreasing production costs and enabling agile product development. Delft

University of Technology designed and manufactured a bubble generator with a conical contraction to better control flow separation inside the nozzle. The use of the HFSB-GEN-V11 nozzle, producing between 20,000 to 60,000 bubbles/s with a mean diameter of 0.55 mm, is discussed in the work of [Faleiros et al. \(2018\)](#) (see Figure 3.2).

[Faleiros et al. \(2019\)](#) employed a CNC-manufactured generator based on the nozzle developed by Delft University of Technology and a bubble generator based on the DLR design by [Bosbach et al. \(2009\)](#). Both nozzles are illustrated in Figure 3.6.

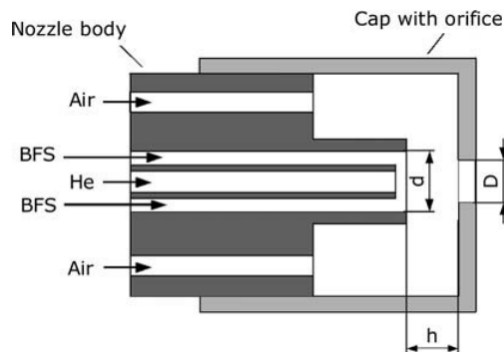


Figure 3.5: Schematic illustration of the DLR nozzle. Reproduced from [Bosbach et al. \(2009\)](#).

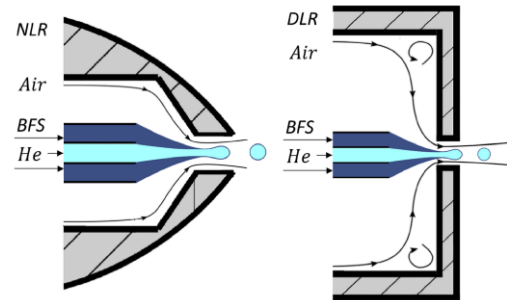


Figure 3.6: Schematic illustration of the nozzles used in the study by [Faleiros et al. \(2019\)](#) (not to scale). Adapted from [Faleiros et al. \(2019\)](#).

Three similar designs were presented and tested by [Gibeau et al. \(2019\)](#). For all nozzles, bubbles were produced with a mean diameter ranging from 0.2 mm to 0.9 mm at approximately 70,000 bubbles/s.

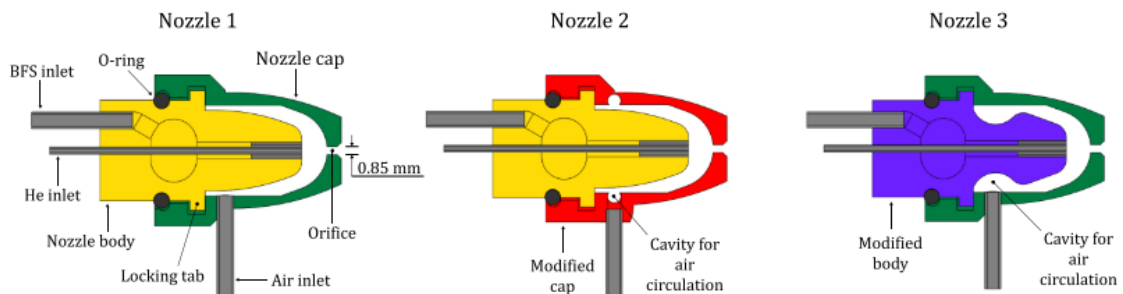


Figure 3.7: Schematics of the nozzles used in the studies by [Gibeau and Ghaemi \(2018\)](#), [Gibeau et al. \(2019; 2020\)](#) (not to scale). Adapted from [Gibeau et al. \(2019\)](#).

Table 3.2 provides an overview of the main production variables for each of the discussed nozzles.

Table 3.2: Production variables for various nozzles.

Generator	Figure	$\langle d_b \rangle$ [mm]	f [kHz]	Reference
Pitot	3.4, <i>left</i>	1.35	0.3	Okuno et al. (1993)
Orifice	3.4, <i>right</i>	1.39	3	Okuno et al. (1993)
DLR	3.5	0.23	200	Bosbach et al. (2009)
DLR	3.5	0.37	50	Morias et al. (2016)
HFSB-GEN-V11	3.2	0.55	40	Faleiros et al. (2018)
Nozzle 3	3.7, <i>right</i>	0.45	70	Gibeau et al. (2020)

3.4. Production Regimes

The accuracy of PIV measurements is directly related to the size distribution of HFSB, affecting the time response as indicated by Equation (2.14). It is therefore crucial to ensure that the nozzle is producing bubbles at optimal operating conditions. As previously mentioned, [Morias et al. \(2016\)](#) distinguished between a stable and unstable production of HFSB while determining the time response variation. A stable, or bubbling, regime is characterized by a periodic production of bubbles that are being formed from within the nozzle. The resulting distribution of bubble diameters is rather monodisperse. The unstable, jetting, regime is characterized by the formation of a slender cylindrical jet extending several diameters beyond the nozzle. Hereafter, jet breakup causes the aperiodic formation of bubbles, with a polydisperse distribution of the particle size. The bubbling and jetting production regimes are also referred to as interior and exterior bubble production, respectively. An example of a nozzle operating in the bubbling and jetting regime can be found in Figure 3.8, whereby shadowgraphy is used to visualize the bubble formation near the nozzle exit.

[Faleiros et al. \(2019\)](#) showed that whether the nozzle is operating in the jetting or bubbling regime can also be evaluated by observing the coefficient of variation of the bubble diameter for both regimes, which reads as

$$CV_d = \frac{\sigma_d}{\langle d_b \rangle}. \quad (3.1)$$

Here, $\langle d_b \rangle$ and σ_d are the average and standard deviation of the bubble diameter, respectively. These statistics can be directly related to the tracing capabilities of a particle which depend, according to [Melling \(1997\)](#), on the diameter and density of a tracer (see Section 2.3.2).

For the HFSB-GEN-V11 generator developed by TU Delft, the coefficient of variation remains between 2 - 3% in the bubbling regime. In the jetting regime, $CV_d \approx 13\%$, as can be observed in Figure 3.9. Results by [Gibeau et al. \(2020\)](#) showed similar deviations in particle diameter coefficient of variation. It was found that for bubbling, $CV_d \approx 2\%$ and while jetting, a wide range of diameters was produced with a coefficient of variation of 23%.

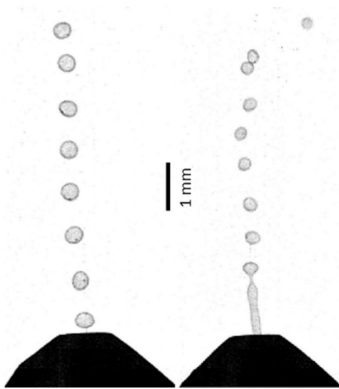


Figure 3.8: Bubbling (*left*) and jetting (*right*) production regimes visualized by shadowgraphy. Adapted from [Faleiros et al. \(2019\)](#).

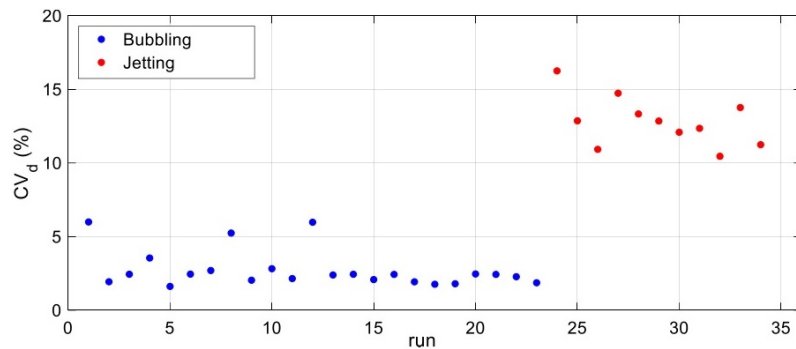


Figure 3.9: Change in HFSB coefficient of variation of the bubble diameter for bubbling and jetting regimes. Adapted from [Faleiros et al. \(2019\)](#).

Akin to the previous results, [Caridi \(2018\)](#) visualized the particle diameter dispersion in another form by plotting the HFSB diameter in both jetting and bubbling cases. The dispersion, as indicated by the coefficient of variation of the particle diameter, is significantly larger for the jetting regime, see Figure 3.10.

Besides the two primary production regimes of bubbling and jetting, [Faleiros et al. \(2019\)](#) distinguished three additional regimes and differentiated between monodisperse and polydisperse operations based

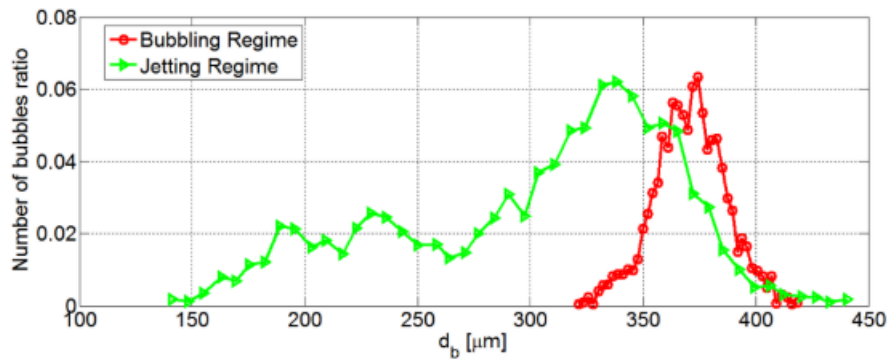


Figure 3.10: Bubble size distribution for the jetting and bubbling regimes. Reproduced from Caridi (2018).

on particle size distributions within the bubbling and jetting regimes. Additional regimes include the production of bubbles in pairs (*Double-bubbling*), merging of bubbles (*Merging*) and the formation of satellite bubbles resulting in a bimodal distribution of bubble sizes (*Satellite bubbling*). Gibeau et al. (2020) identified several more regimes, including the occurrence of satellite bubbles remaining attached to the primary bubble (*Attached satellite bubbling*) and the condition when satellite bubbles were produced in the jetting mode (*Satellite Jetting*).

The parameters that dictate the production regime are orientation, internal nozzle geometry and operational parameters. The latter refers to the combination of supply flow rates of air, helium and bubble fluid solution which allow for precise control of the bubble production. The influence on bubble production parameters, such as size and production frequency, will be addressed in Section 3.7. In the comparisons below, the effect of nozzle orientation is discussed first. Secondly, variations in nozzle performance by changing air, helium and soap flow rates are described. Lastly, an overview is given how geometrical changes affect the type of production regime.

Nozzle Orientation

In the works by Faleiros et al. (2019) and Gibeau et al. (2019), several nozzle designs have been tested. In the former work, a systematic procedure was used to assess nozzle performance based on production regimes. Here, production maps are used to qualitatively classify nozzle performance based on production behaviour. These maps are created by consecutively increasing the volume flow rate of helium while keeping air and soap fixed. For each flow setting, the production regime is labelled. The procedure is repeated for varying flow rates of helium and soap until a complete overview of the operational range is obtained.

The influence of nozzle orientation on the performance of a bubble generator has been investigated by Gibeau et al. (2019). The nozzle design, illustrated in Figure 3.7, is positioned both horizontally and vertically while cycling through various volume flow rates and mapping the production behaviour. The resulting maps are presented in Figure 3.11. Note that *Bubbling* includes: *mono- and polydisperse bubbling* and *attached satellite bubbling*, while *Jetting* includes both *mono- and polydisperse jetting*. All other regimes are grouped under *Atypical*, consisting of *Merging*, *Satellite- bubbling* and *jetting* and any transitions between regimes. Gibeau et al. (2019) reported that the loss of performance for the horizontally orientated nozzle is associated with soap built-up within the nozzle. Excessive soap, which is blocking the nozzle, is drained in the vertical direction. Furthermore, it is suggested that the axisymmetry of the coaxial flows is better preserved since gravity acts parallel to the nozzle output flow.

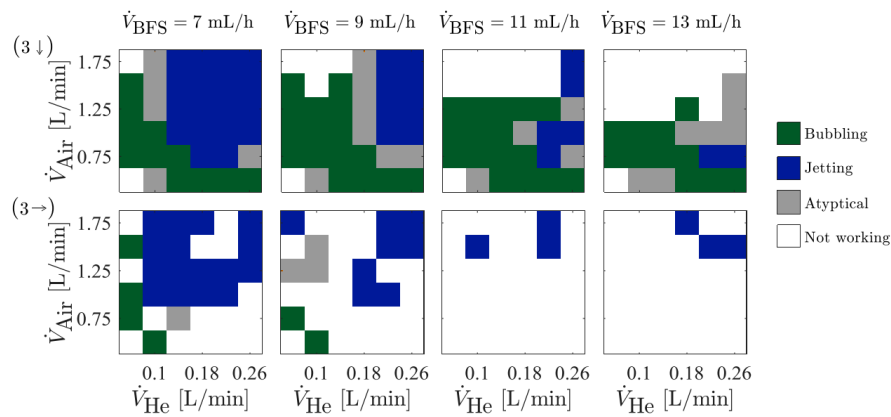


Figure 3.11: Production envelopes of Nozzle 3 (Figure 3.7, *right*), with arrows indicating nozzle orientation; vertically (top) and horizontally (bottom). Adapted from [Gibeau et al. \(2019\)](#).

Operational parameters

By observing the trends in Figure 3.11 for the vertically orientated nozzle 3, [Gibeau et al. \(2019\)](#) argued that increasing soap flow rates decreased jetting behaviour of the nozzle. Additionally, bubbling behaviour was often found at relatively low flow rates while jetting was often the result of higher rates of air and/or helium. [Faleiros et al. \(2019\)](#) observed similar trends for the NLR type nozzle (Figure 3.6) and corroborated this by shadowgraph visualizations, presented in Figure 3.12. It was also noted that opposite trends are valid for soap, yielding bubbling behaviour for higher flow rates of BSF.

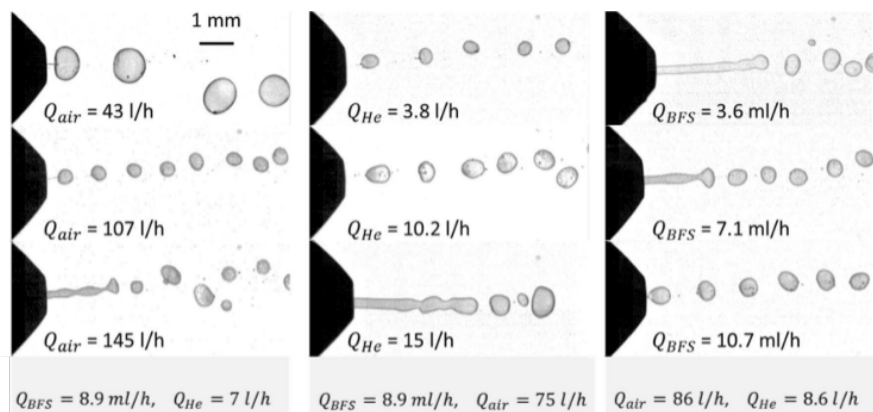


Figure 3.12: Bubbling and jetting behaviour as a result of changes in operational parameters for the NLR nozzle (Figure 3.6, *left*). Adapted from [Faleiros et al. \(2019\)](#).

Geometrical parameters

The effect of the internal nozzle geometry on the production behaviour in terms of regimes has only been addressed by [Gibeau et al. \(2019\)](#). The authors investigated modifications to improve the concentricity of the internal flows, in particular for the focusing air gas. It was observed that for nozzle 3 (see Figure 3.7), with the most extreme modifications to aid axisymmetry of the airflow, the performance had been greatly improved in terms of bubbling behaviour. The results of this study for the nozzles in Figure 3.7 can be found in Figure 3.13

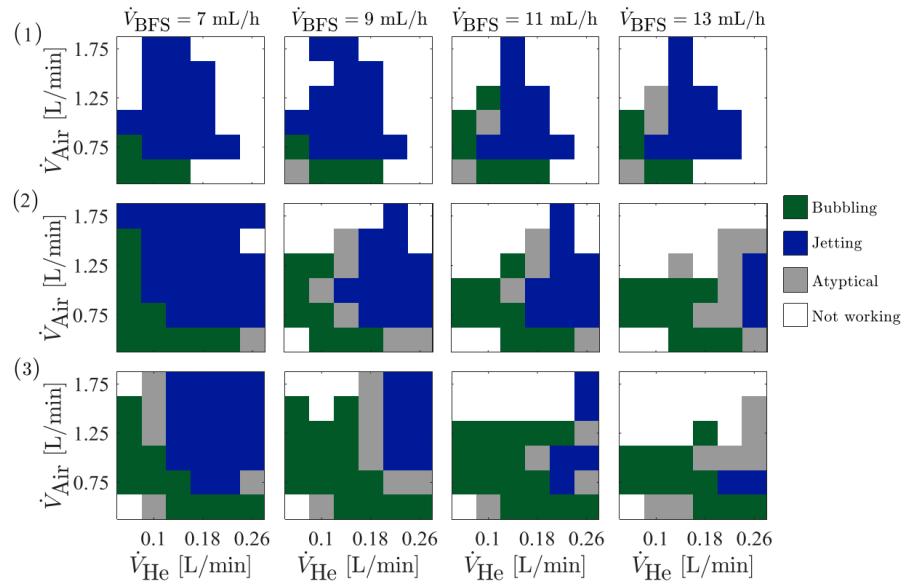


Figure 3.13: Production envelopes of Nozzles 1, 2 and 3 (Figure 3.7), all in the vertical orientation. Adapted from [Gibeau et al. \(2019\)](#).

3.5. Fluid Mechanical Properties

With the introduction of a new kind of tracer for aerodynamic wind tunnel experiments, it is relevant to assess the pros and cons of the increased particle size in terms of tracing characteristics. Section 3.5.1 will highlight the deviations from Stokes' law as a result of the larger diameter. Previous research on the tracing fidelity of HFSB and the influence of the operational parameters on the time response is described in Section 3.5.2.

3.5.1. Particle Dynamics

The increased size of an HFSB, compared to a conventional micron-sized particle, causes the particle drag coefficient modelled after Stokes to further deviate from experimental findings, as presented in Figure 2.7. As a result of the direct proportionality of the particle Reynolds number with the particle diameter d_p , Re_p for a typical HFSB experiment has an order of magnitude above 1 ([Scarano et al. 2015](#)). However, applying the additional correction term as described in Section 2.3.1 will ensure an accurate modelling and accounts for the effects of high Reynolds numbers in the determination of the time constant τ_p in Equation (2.15).

The application of the particle dynamic equations of Section 2.3.1 to model tracers, requires that particles retain their spherical shape. For solid particles, this condition is easily met. However, as a bubble is produced, the bubble may be deformed and a certain amount of time is required to attain its spherical shape. [Loth \(2008\)](#) noted that the deformation is predominantly controlled by the non-dimensional Weber number We . It relates inertial stresses, causing deformation, to surface tension stresses which resist deformation by:

$$We_p = \frac{\rho_f(u_p - u_f)^2 d_p}{\sigma}, \quad (3.2)$$

where σ is the surface tension between the surrounding fluid and the bubble surface. This relation is valid for $1 \leq Re_p \leq 10,000$. [Loth \(2008\)](#) defined three states based on the Weber number:

- $We_p \ll 1$ particles rapidly tend to spherical geometry
- $We_p \sim 1$ particles suffer moderate deformation
- $We_p \gg 1$ particles deviate significantly from a sphere

The validity of the assumption that tracers are spherical, for which the dynamic forces on a particle can be modelled, was investigated by [Faleiros et al. \(2019\)](#). In the experiment, conducted in a stagnation flow in front of a cylinder of 50 mm in diameter, the relationship of We_p with the bubble slip velocity is studied. Bubble deformation was considered negligible since We_p is more than one order of magnitude smaller than the condition for a clean sphere ($We_p \leq 0.064$), see Figure 3.14.

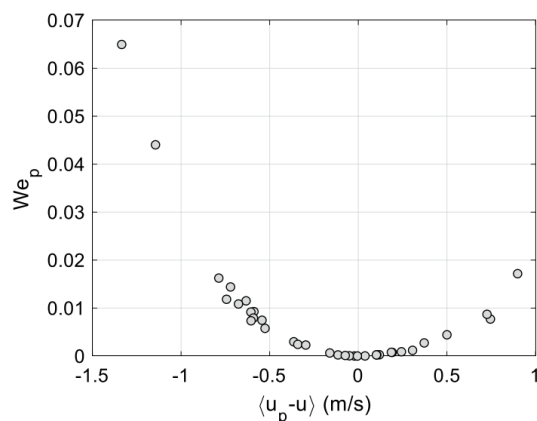


Figure 3.14: Variation of the Weber number with slip velocity. Reproduced from [Faleiros et al. \(2019\)](#).

3.5.2. Tracing Fidelity

Research on the tracing fidelity of neutrally buoyant bubbles was first initiated by [Kerho and Bragg \(1994\)](#), analysing particle trajectories in the stagnation region of a NACA0012 airfoil at a free-stream velocity of 18 m/s, whereby $Re_c = 640,000$. The bubble generator in Figure 3.1 produced bubbles ranging from 1 mm to 4.75 mm in diameter with deviations from the neutrally buoyant condition $\rho_p/\rho_f = 1 \pm 0.3$. After being produced, bubbles were injected into a vortex filter to expel heavier-than-air bubbles. The resulting bubbles released into the free stream flow were therefore biased towards lighter-than-air particles. As a consequence, HFSB trajectories departed from the theoretical streamlines by anticipating the deceleration and curvature of the flow, as presented in Figure 3.15.

With the improved nozzle design by [Bosbach et al. \(2009\)](#), which will be discussed in Section 3.3, [Scarano et al. \(2015\)](#) produced sub-millimetre HFSB with higher controllability of the input flow rates to assess flow-tracing fidelity. Again, a stagnation flow was considered to ensure high particle decelerations, maximizing the effect of deviations from the neutral buoyancy condition. The region of interest was located in front of a 25 mm cylinder at flow speeds up to 30 m/s. The particle diameter d_b was estimated to be 400 μm , with a time response τ_p of 10-30 μs . By comparing reference velocities of micron-sized fog droplets with bubble trajectories of varying flow rates, a mean value of $u_{\text{slip}} = 10$ cm/s was reported in optimal conditions. This corresponds to 0.3% of the free-stream value. Authors critically reflect on the particle size deviation between tracers, as this could lead to deviations in the neutral buoyancy of HFSB.

Individual particle statistics of HFSB were included in the study of [Morias et al. \(2016\)](#), whereby 40 mm in diameter cylinder was submerged in a free-stream flow at 20 m/s. With the nozzle generator from [Bosbach et al. \(2009\)](#), it was observed that bubble diameter variations CV_d remained below 5%. In this work, a distinction between the bubbling and jetting production regimes was first made. From the presented data, it is determined that within the jetting regime, CV_d increased up to 18.9%.

Additional experiments to assess tracer fidelity include velocity measurements in the core of vortices by [Caridi et al. \(2017\)](#) and in wall-bounded turbulence by [Faleiros et al. \(2018\)](#). In the former work, a mean diameter of $300 \mu\text{m}$ and $CV_d = 10\%$ was reported using the nozzle of [Bosbach et al. \(2009\)](#). It was concluded that due to the dispersion in HFSB density, lighter-than-air tracers tend to accumulate within the vortex axis, which is advantageous for leading edge vortex visualizations. The latter study described the use of an in-house developed nozzle by TU Delft to analyse tracer fidelity in a cylinder stagnation flow, see Figure 3.16. Bubble diameters were estimated to be 0.55 mm , and $CV_d = 13\%$ in the stable production regime. The time response $\tau_p = 30 \mu\text{s}$ with a standard deviation σ_τ of $20 \mu\text{s}$. The study concludes that ‘‘HFSB tracers can be used to determine the mean velocity and the turbulent fluctuations of turbulent boundary layers above a distance of approximately two bubble diameters from the wall’’ ([Faleiros et al. 2018, p. 12](#)).

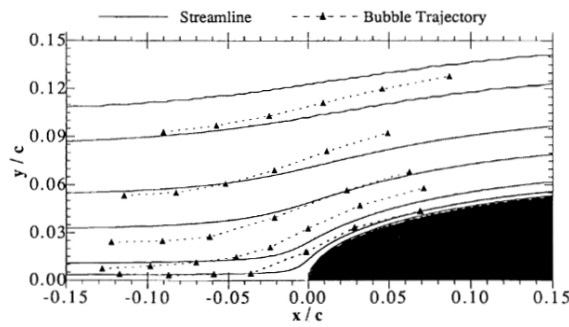


Figure 3.15: Streamlines and HFSB trajectories in a NACA0012 stagnation flow. Reproduced from [Kerho and Bragg \(1994\)](#).

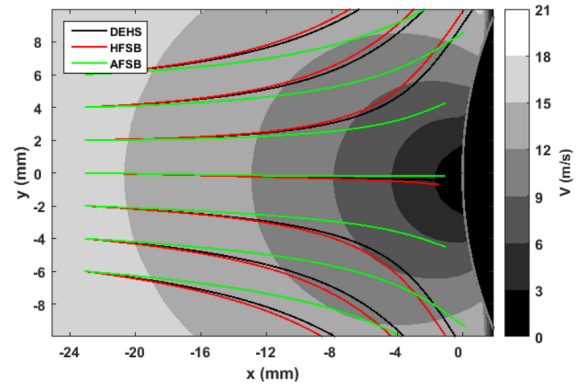


Figure 3.16: Comparison between DEHS, HFSB and AFSB trajectories in a stagnation flow in front of a cylinder. Adapted from [Faleiros et al. \(2018\)](#).

More recently, [Faleiros et al. \(2019\)](#) extensively reported on the tracing capabilities of HFSB. By approaching the neutral buoyancy condition, the time response is minimized. This can be achieved by careful control of the helium and soap flows ([Scarano et al. 2015](#)). Assuming no leakage of helium and spillage of soap, mass conservation can be applied to the bubble formation process:

$$fV_b\rho_b = Q_{\text{He}}\rho_{\text{He}} + Q_{\text{BFS}}\rho_{\text{BFS}}, \quad (3.3)$$

in which ρ_b , ρ_{He} and ρ_{BFS} are the bubble, helium and soap densities, respectively. A relation for the bubble density can be derived by relating the bubble volume V_b to the production frequency f via $V_b = Q_{\text{He}}/f$. As the soap film thickness is three orders of magnitude smaller than the diameter of the bubble, it can be neglected ([Caridi 2018](#)). This yields:

$$\rho_b = \rho_{\text{He}} + \frac{Q_{\text{BFS}}}{Q_{\text{He}}}\rho_{\text{BFS}}. \quad (3.4)$$

As a result, the density of air at room temperature is approached by ρ_b at $Q_{\text{He}}/Q_{\text{BFS}} = 1095$ using the values stated in Table 3.1. At this theoretical flow rate ratio, a HFSB acts as an ideal flow tracer [Faleiros et al. \(2019\)](#). In practice, however, this condition is difficult to achieve due to helium and soap production losses. This was experimentally investigated by determining the density difference $\bar{\rho}$, as stated in Section 2.3.2, for a variety of conditions of $Q_{\text{He}}/Q_{\text{BFS}}$. The experimental neutral buoyancy condition was subsequently derived by applying an empirical fit. At the crossing of the neutral buoyancy condition $\bar{\rho} = 0$, the ratio $Q_{\text{He}}/Q_{\text{BFS}} = 900$. This is indicative for spillage of soap since the neutral buoyancy condition can be achieved at lower flow rates of helium as compared with the theoretical value of approximately 1095.

[Faleiros et al. \(2019\)](#) studied, among other relationships, the relation between the HFSB response time and the Stokes number as a function of soap and helium flow rates with a similar experimental

set-up as previously used in [Faleiros et al. \(2018\)](#). The results, displayed in Figure 3.17, show that the data largely follows the linear trend between response time and $Q_{\text{BFS}}/Q_{\text{He}}$, given by Equation (3.4) and Equation (2.15) Equations (2.15) and (3.4). [Faleiros et al. \(2019\)](#) concluded that the deviations from the linear regression line may be a result of the non-linear correction term ϕ and variations in the particle diameter.

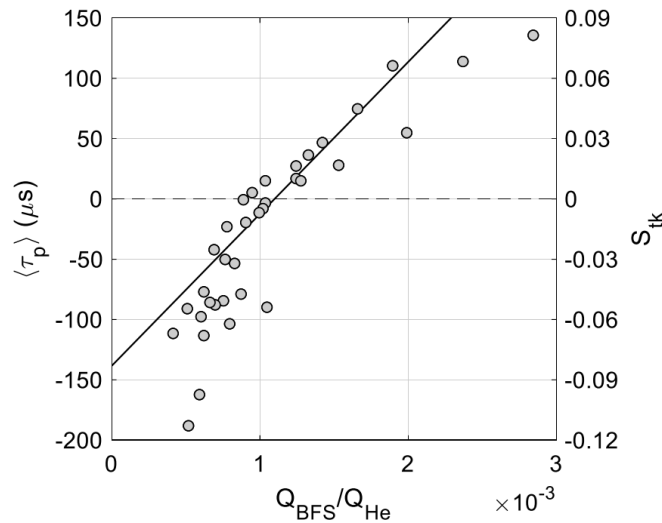


Figure 3.17: HFSB time response and Stokes number as a function of soap and helium flow rates, with $U_{\infty} = 30 \text{ m/s}$ and $L = 50 \text{ mm}$. The linear fit is forced through the experimental neutral buoyancy condition. Reproduced from [Faleiros et al. \(2019\)](#).

Lastly, [Faleiros et al. \(2019\)](#) studied the relationship between the mean particle time response τ_p and mean diameter $\langle d_b \rangle$ for varying particle densities. Figure 3.18 shows that as particles become larger, the volume ratio of helium over soap increases, therefore creating a lighter particle anticipating flow features. Moreover, it provides quantitative information regarding the production accuracy of bubbles. As the bubble size increases, deviations between particle and fluid density become more pronounced in the time response of an HFSB.

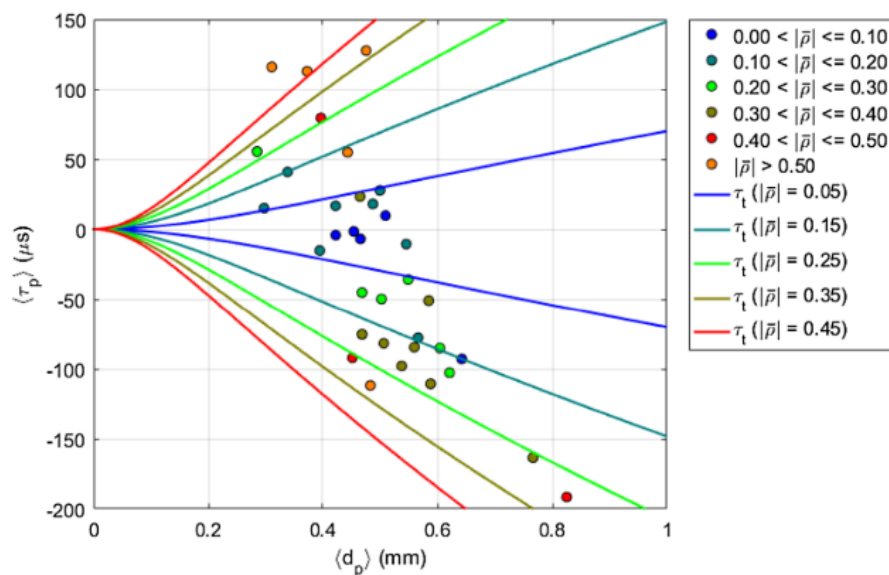


Figure 3.18: HFSB time response as a function of particle diameter. Reproduced from [Faleiros et al. \(2019\)](#).

3.6. Optical Characteristics

The unique optical behaviour of HFSB requires careful consideration of its light scattering characteristics. Given the average size of a soap bubble, Section 2.3.3 described that the optical behaviour is governed by geometrical optics. To quantify the scattering behaviour, light propagation through an HFSB is modelled by a homogeneous air-filled sphere with a negligible-thickness transparent shell, using the following assumptions:

- Negligible BFS soap film thickness compared to the bubble size (approximately 55 nm for a bubble diameter of 300 μm (Morias 2016))
- Marginal differences in the refractive indexes of air and helium ($n_{\text{air}}/n_{\text{helium}} \approx 1$ (Mansfield and Peck 1969))

As a result, ray deflection is only a result of refraction and reflection between the air and soap mediums and is negligible through the soap film. This creates two bright spots of intensity maxima when viewed by a certain direction, see Figure 3.19. Those source points, generally known as glare points, were the subject of a study by Hulst van de and Wang (1991). It was found that the spacing between glare points d_g is dependent on the scattering angle θ_s , the particle diameter d_p and the refractive indices of the outer and inner medium of the bubble. Glare points are equidistant with respect to the circumcentre of the bubble, as indicated in Figure 3.20.

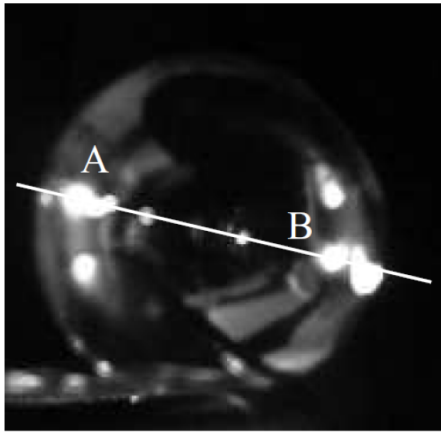


Figure 3.19: Light scattered by a bubble's surface. Reproduced from Macháček (2003).

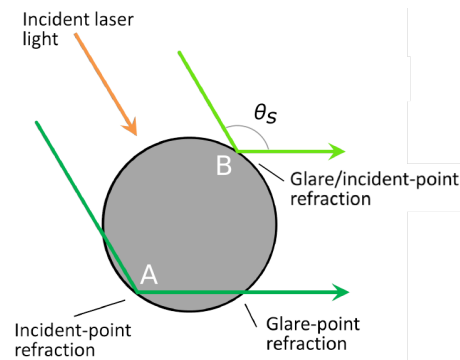


Figure 3.20: Schematic illustration of glare points produced by scattering of parallel light rays. Adapted from Morias (2016).

Mathematically, the glare point distance is related to the particle diameter via:

$$d_g = d_p \cos\left(\frac{\pi - \theta_s}{2}\right). \quad (3.5)$$

This means that for a scattering angle θ_s of 90° , the relation for particle diameter d_p and glare point distance d_g becomes:

$$d_b = \sqrt{2}d_g. \quad (3.6)$$

Comparing the collected scattering energy and camera aperture size for both DEHS and HFSB particles, Caridi (2018) experimentally confirmed that HFSB scatter $2 \cdot 10^4$ more light for a given set-up. This is a result of the higher scattering efficiency and increased particle size of the bubbles.

A numerical assessment of the total energy collected by the camera, for a given experimental set-up and HFSB size, was also conducted by Caridi (2018). A ray-tracing model was employed to compute

the light scattered by an HFSB, using only the most energetic rays from reflection and the first order refraction. It was found that the scattered light intensity follows a quadratic increase with particle diameter, see Figure 3.21. Furthermore, Caridi (2018) investigated the angular dependence of the light scattering intensity of an HFSB with a diameter of 300 μm , which is graphically shown in Figure 3.22 for both theoretical and experimental results. It shows that the scattering intensity is lowest at side-scattering, or $\theta = 90^\circ$. This trend is similar to the scattering distribution of micron-sized particles in Figure 2.12. However, the changes in magnitude are significantly different. The scattering intensity of micron-sized particles between forward and backward scattering differ several orders of magnitude, while for HFSB, scattering intensity is in the same order of magnitude for both directions.

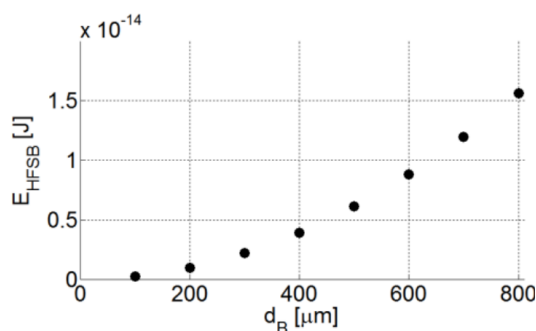


Figure 3.21: Relation between scattered light intensity and HFSB diameter for a scattering angle of $\theta = 90^\circ$. Adapted from Caridi (2018).

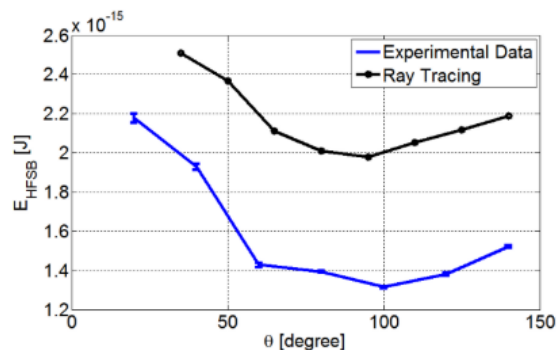


Figure 3.22: Light scattering intensity as a function of observation angle. Adapted from Caridi (2018).

3.7. Bubble Scalability

Besides the production regime, operational and geometrical parameters also govern the bubble size. According to Bosbach et al. (2009), this is one of the very promising features of HFSB for PIV measurements. The scalability of bubbles can be attributed to two aspects, which will be covered in more detail in the following sections.

Operational parameters

The study by Gibeau and Ghaemi (2018) was the first to report variations of particle diameters by varying flow rates. It was observed that the air flow rate did not significantly affect HFSB diameter. Variations in helium caused the largest changes in particle size. Lastly, it was concluded that an increase in soap flow rate resulted in thickening of the soap film, explaining the observed trend of increasing diameter.

However, Faleiros et al. (2019) reported that $d_p = d_p(Q_{\text{Air}}, Q_{\text{He}}, d_o)$, which partially contradicts the statements made by Gibeau and Ghaemi (2018). Empirical analysis showed that the bubble volume is proportional to the flow rate ratio of air and helium and the orifice diameter. Therefore, Faleiros et al. (2019) suggested that the particle diameter scales according to $d_p \propto (d_o Q_{\text{He}} / Q_{\text{Air}})^{1/3}$. In subsequent research by Gibeau et al. (2020), the scaling law is examined for the nozzles presented in Figure 3.7. From the results in Figure 3.23, authors conclude that the data in accordance with the scaling law. Additionally, Gibeau et al. (2020) presented maps, similar to the production regime maps, of the mean bubble diameter for 144 operating points, shown in Figure 3.24. Conclusively, both studies replicated findings that larger bubbles can be obtained by increasing Q_{He} , while smaller bubbles are a result of increasing Q_{Air} .

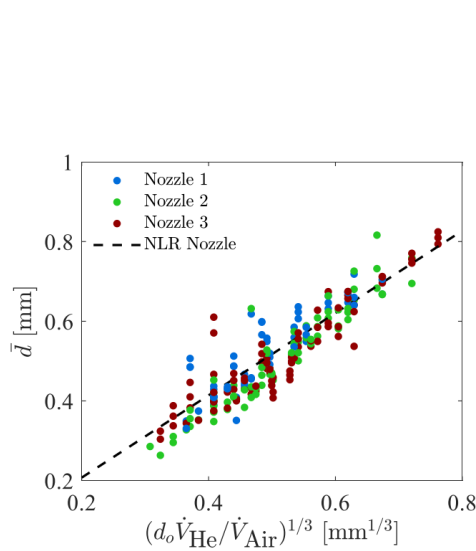


Figure 3.23: Bubble size scaling law for the nozzles displayed in Figure 3.7, including linear fit of the NLR nozzle. Reproduced from Gibeau et al. (2020).

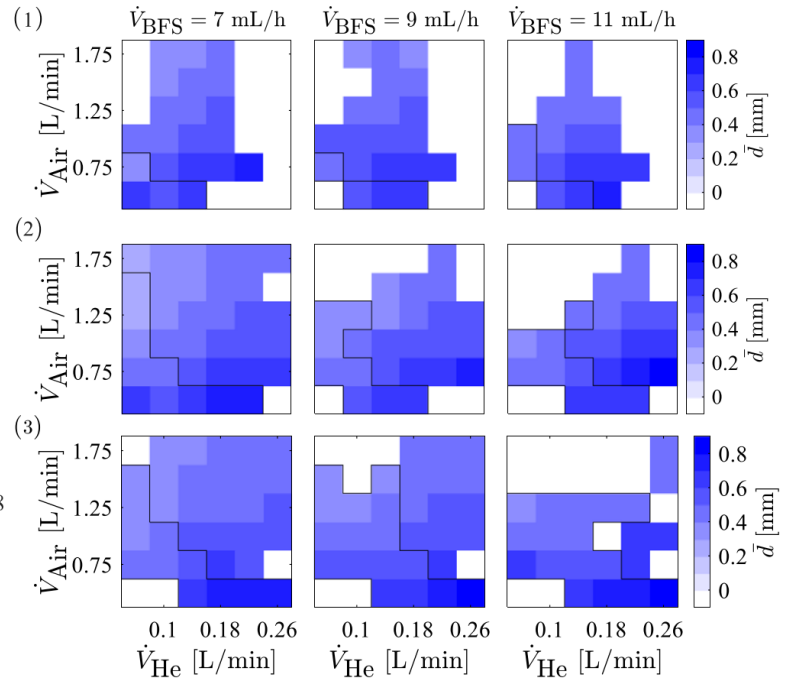


Figure 3.24: Relation between flow rates and bubble diameter, for the nozzles displayed in Figure 3.7. Outlines in black represent the bubbling regime. Adapted from Gibeau et al. (2020).

Geometrical parameters

With the introduction of the orifice-type nozzle, Okuno et al. (1993) reported that HFSB size can be controlled by the nozzle orifice diameter. Authors reported that there is a one-to-one relationship between particle and orifice diameter for the three tested conditions $d_o = [1.0, 1.5, 2.0]$. Trends of state-of-the-art orifice type nozzles, capable of producing bubbles at rates ten times higher, were presented by Faleiros et al. (2019). It was found that the data for varying orifice diameter follows the aforementioned proportionality up to a certain degree. At the extremes, it was reported that the spread is more pronounced, as can be seen in Figure 3.25. As the Weber number increases for larger particles, Authors argued that the deviation from a spherical shape could cause measurements to overestimate the actual particle size.

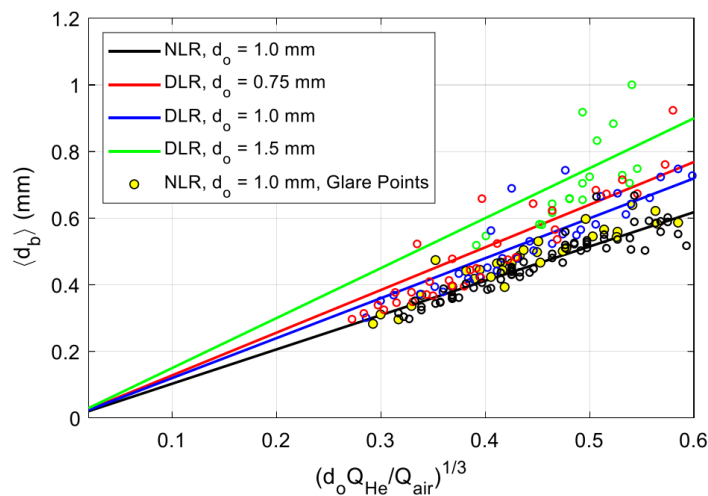


Figure 3.25: Trends observed for HFSB particle size with flow rate and orifice diameter. Reproduced from Faleiros et al. (2019).

3.8. Extended Optical Analysis

The preceding section described how both operational and geometrical parameters can influence the size of HFSB. Increasing the measurement domain is based on the premise that larger particles scatter more light. To substantiate this, a detailed optical analysis by means of a ray-tracing model is performed, based on the model presented by [Caridi et al. \(2015\)](#). This is a method for calculating the path of light rays, which direction can be changed by reflecting surfaces such as the soap shell of HFSB. With the known light propagation in all directions, the amount of light passing the camera aperture is determined. Herewith, the relationship between the particle diameter and the light intensity is determined theoretically.

3.8.1. Ray Tracing Model

As described in Section 2.3.3, for particles where the Mie scattering parameter $x_M > 90$, geometrical optics is applicable. Here, light is divided into discrete or individual light rays which propagate without interacting with each other. A simplified model is used to describe light behaviour. Adding to the model assumptions of geometrical optics:

- Incident light rays are parallel and uniform.
- Reflections are specular.
- The soap shell has a negligible thickness and is optically smooth.
- Light propagation through helium and air is identical.
- Higher-order reflections are neglected.
- The problem is considered to be two-dimensional

The model assumes a collimated beam of light, which is the case for lasers. After emittance, collimated light is reflected onto the surface of the bubble. Surface reflectance is called specular when the incident light is reflected in a single direction. The reflective surface is mirror-like, and thus incident and reflected rays have identical angles between the ray and the surface normal: $\alpha_i = \alpha_r$ ([Katz 2002](#)). Snell's law can be used to determine the direction of refracted rays:

$$n_1 \sin \alpha_1 = n_2 \sin \alpha_2. \quad (3.7)$$

Here, the indices of refraction for both mediums are given by n_1 and n_2 .

After reflecting with the sphere's surface, a part of the ray propagates through the soap film. As presented in Section 3.6, the film thickness is approximately 55 nm for a bubble diameter of 300 μm ([Morias 2016](#)). Although the light refracts in the soap film, due to its thickness the change in direction is assumed to be negligible. This also implies that thin-film interference effects do not occur. These effects arise when light reflects against the upper and lower boundaries of the soap film and interfere with each other. As a result, the amplitude of the reflected light is either enhanced or reduced. However, as this model will analyse the number of light rays reaching the camera sensor, the loss or increase of light intensity of individual rays is not computed.

Light rays are modelled to pass without alterations in their direction through the inner medium of the HFSB. This approximation is accurate, since the ratio of refractive indices between helium and air is approximately 1 ([Mansfield and Peck 1969](#)). Snell's law, therefore, states that the incident and reflective angles are identical. Furthermore, only the most energetic reflections are considered. A study by [Tropea \(2011\)](#) showed that for the first 10 reflection and refractive scattering order, at a scattering angle of 90° the first-order reflection is the most energetic. Hence, it is sensible to neglect all higher order reflections.

The model is considered to be two-dimensional to simplify the reflectance of rays. However, it will be

shown that the drawn conclusions can be extended to three-dimensions without additional computations.

A schematic overview of the optical set-up that is used by the model is shown in Figure 3.26. Four incident light rays reflect on the bubble's surface which are captured by the camera aperture. Hereafter, both red and blue rays are focused on the camera sensor via a converging lens (not drawn), creating two glare points. The incident light is travelling parallel to the x -axis. The angle of incidence α_i is defined with respect to the dotted line, normal to the sphere's surface. Following Snell's law, this angle is identical to the reflected angle α_r for mediums with the same index of refraction. The camera aperture, modelled as a slit with width D , is placed at a distance L_a .

To analyse the amount of light that is captured by the camera sensor, the amount of light reaching the sensor is divided by the number of emitted rays.

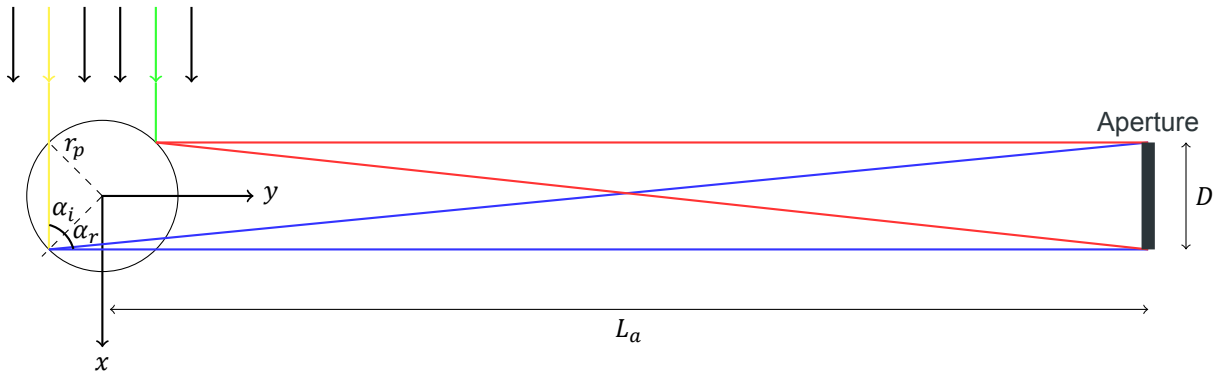


Figure 3.26: Model coordinate system for a for 90° scattering angle. Dimensions not to scale.

3.8.2. Scattering Intensity

A numerical evaluation of the amount of light collected by the imaging system is performed using the simplified ray tracing model as explained in the previous section. The results for two particles, whereby $d_{p,2} = 2d_{p,1}$, are shown in Figure 3.27. While emitting the same number of light rays, the bubble's surface is able to focus more rays towards the aperture. The ratio between the reflected rays reaching the aperture and the total number of rays emitted I_{sensor}/I_0 is plotted against the particle diameter in Figure 3.28.

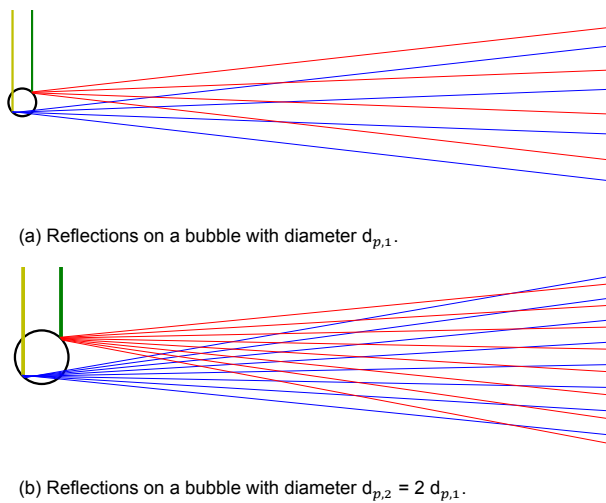


Figure 3.27: 2D light ray scattering behaviour modelled via ray tracing.

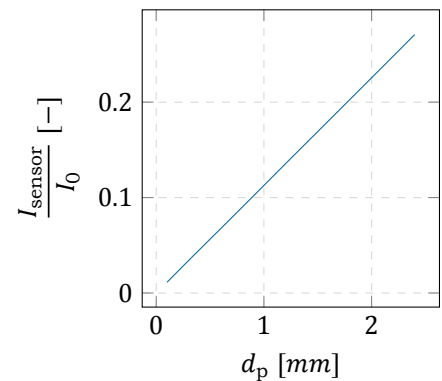


Figure 3.28: Numerical 2D scattering intensity behaviour as a resulting of particle diameter scaling.

The ray tracing model shows that the following relation holds in the two-dimensional case:

$$I_{2D} \propto d_p.$$

However in reality, the bubbles act as a sphere and reflect light in three-dimensions. In this case, the aperture is no longer a slit and is approximated as a circle. The relationship between light intensity and particle size is thus:

$$I_{3D} \propto d_p^2.$$

The quadratic increase of scattered light intensity with particle diameter from this analysis is identical to the observations made by [Caridi \(2018\)](#), as described in Section 3.6.

Figures 3.26 and 3.27 may give the impression that glare points originating from reflection points on the bubble's surface are visible as point sources. However, looking at a more detailed image of the reflection of light in Figure 3.29, it becomes clear that in the two-dimensional case glare points represent part of the bubble arc. The asymmetry of the reflections originating from the convex and concave sides can also be observed. The incident rays reflecting on the convex side of the bubble's surface diverge, whereas light rays reflecting on the concave side converge and form a focal point. In three-dimensional space, glare points exhibit a circular shape, as presented by the intensity distribution of camera pixels in Figure 3.30.

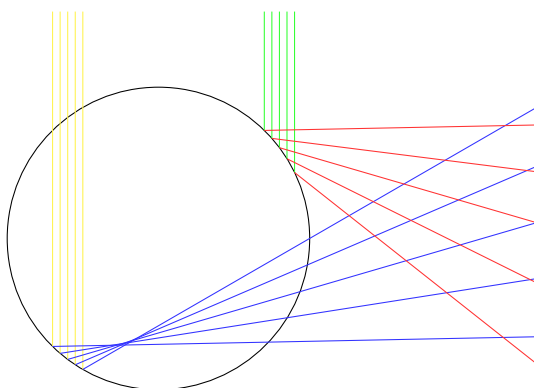


Figure 3.29: Detail of 2D light ray scattering behaviour

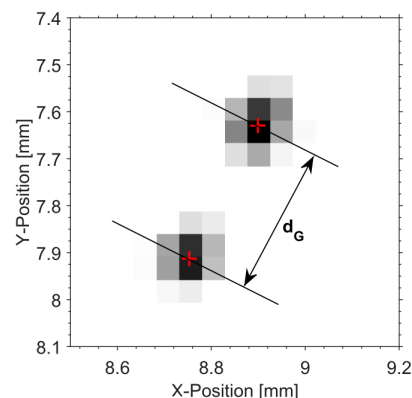


Figure 3.30: Intensity distribution of glare points in 3D with maxima indicated by red crosses. Reproduced from [Morias \(2016\)](#).

3.9. Measurement Volume

Measurements with conventional particles do not commonly exceed 50 cm^3 . To put this into perspective, 50 cm^3 is roughly the size of a strawberry. The introduction of HFSB lead to the partial upscale of the maximum attainable measurement domain due to the increase in reflected light for larger particles sizes. Using HFSB allowed [Scarano et al. \(2015\)](#) to measure flows inside a 4800 cm^3 domain, which is similar to measurements by [Terra et al. \(2016\)](#) to visualize flow fields within a 4800 cm^3 domain. This can approximately be resembled by the volume of a human head. It shows that using HFSB with an average diameter of $300 \mu\text{m}$ does not provide adequate light scattering capabilities to increase the field of view for large scale experiments. Traversing or robotic PIV systems, as described in Section 2.5, provide the flexibility to increase the measurable domain to the order of a metre. An example is the

2 m³ cyclist wake analysis by [Jux \(2017\)](#). However, it will be shown in Section 3.10 that this system suffers from some drawbacks.

With the use of PIV in automotive, aerospace and wind energy industries, a full-scale analysis requires even bigger domains. Competitive motorsports, such as Formula One, require the use of scaled wind tunnel models typically occupying 3.2 m³ ([Senft and Gillan 2019](#)). For commercial automotive industries, an averaged-sized sedan occupies approximately 10 m³. An overview of relevant time-resolved experiments using micron-sized particles as well as helium-filled soap bubbles is presented in Figure 3.31. Additional marks of typical volumes are included as a reference. It should be noted that the size of the measurement domain for an aerodynamic analysis depends on the wake of an object, which is only partly dependent on its size. Using HFSB of approximately 0.3 mm in diameter, measurement volumes do not exceed the average human body volume. Only with the use of robotic CCV as done by [Jux \(2017\)](#), time-averaged measurements can be performed in domains in the order of 1 m³.

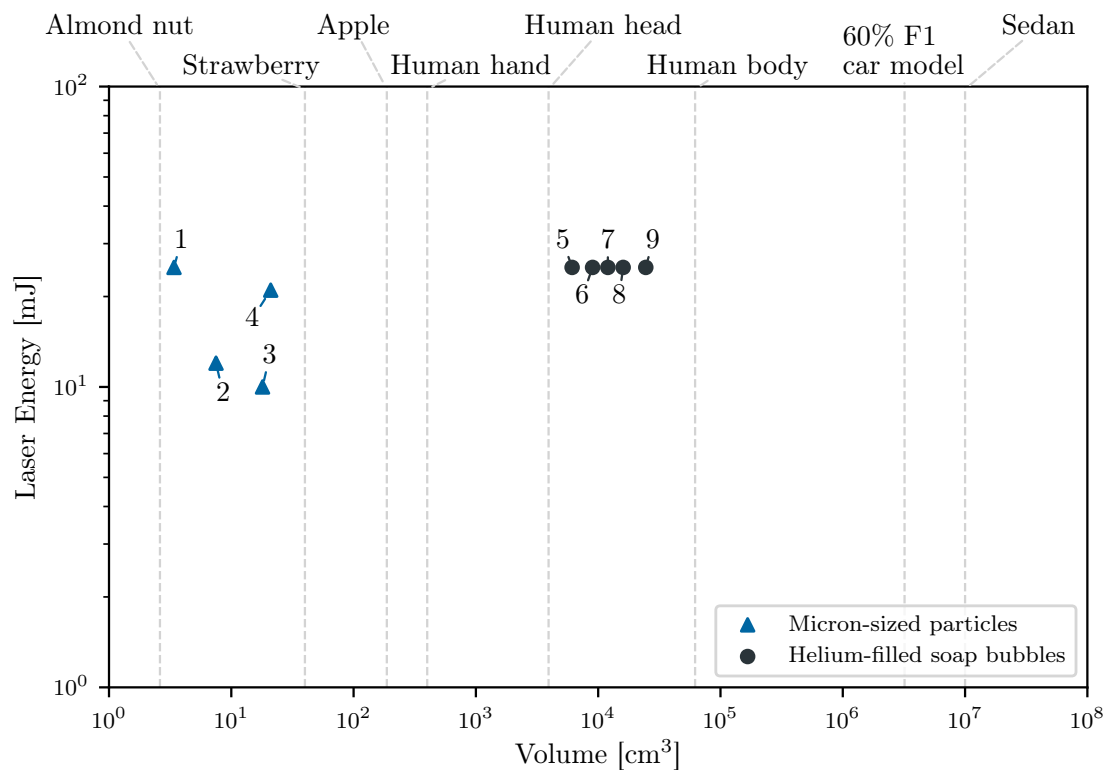


Figure 3.31: Overview of time-resolved 3D3C experiments in air at $U_\infty > 5$ m/s. 1: [Pröbsting et al. \(2013\)](#), 2: [Violato et al. \(2011\)](#), 3: [Ghaemi and Scarano \(2011\)](#), 4: [Schröder et al. \(2008\)](#), 5: [Schneiders et al. \(2016\)](#), 6: [Kim et al. \(2020\)](#), 7: [Caridi \(2018\)](#), 8: [Caridi et al. \(2015\)](#), 9: [Caridi et al. \(2016\)](#).

Further upscale of the measurement domain requires the use of more powerful light sources, advanced multi-camera set-ups, larger traversing or robotic PIV systems or the use of bigger particles. An example is the study of [Rosi et al. \(2014\)](#) where air-filled soap bubbles have been employed to analyse part of the atmospheric surface layer. In a measurement domain of 16 m³, particles were used to characterize coherent structures within the atmospheric surface layer. Another use of bigger particles is the use of helium-filled latex balloons in the study of a convective cell of 134 m³ ([Lobutova et al. 2009](#)). A drawback is the manual filling of the balloons and thus the limited production frequency. These techniques are therefore only employed at relatively low flow rates such as convective cells ($U_\infty < 1$ m/s).

[Caridi \(2018\)](#) investigated the implications on the measurement volume in terms of particle imaging. This is based on the work of [Adrian \(1991\)](#) in which the light energy collected by the camera sensor E is defined by

$$E = \frac{I_0 \lambda^2}{\Delta Z^2 L_O^2} \frac{\pi}{4} \left(\frac{f}{f_{\#}} \right)^2 \left(\frac{d_p}{\lambda} \right)^2. \quad (3.8)$$

The laser pulse energy is defined by I_0 having a wavelength λ . The object distance is given by L_O . Out-of-focus particles, which affect the measurement accuracy, are minimised by choosing the f-stop $f_{\#}$ such that the measurement volume depth ΔZ is equal to the depth of focus δZ , as explained in Section 2.2.1. It is therefore possible, as [Caridi \(2018\)](#) argued, to substitute Equation (2.4) resulting in

$$E = \frac{I_0 \lambda^2}{\Delta Z^2 L_O^2} \frac{\pi}{4} \frac{4.88 \lambda}{\Delta Z} \left(\frac{M+1}{M} \right)^2 \left(\frac{d_p}{\lambda} \right)^2, \text{ or} \quad (3.9)$$

$$\Delta Z^2 = \left(\frac{I_0}{E_{\text{HFSB}}} \frac{\pi}{4} \frac{4.88 \lambda}{L_O^2} \left(\frac{M+1}{M} \right)^2 d_p^2 \right)^{\frac{2}{3}}, \quad (3.10)$$

where measurement volume is a square area. Analogous to [Caridi \(2018\)](#), an experimental set-up with $f = 50$ mm, $M = 0.05$, $L_O = 1.0$ m and $\lambda = 530$ nm is used. A high-speed laser with a pulse energy of $I_0 = 25$ mJ is chosen, corresponding to the lasers used in HFSB experiments of Figure 3.31. The light energy scattered by a HFSB E_{HFSB} of 0.3 mm in diameter is taken as a reference, which is 1.4×10^{-15} J. In the present work, the cross-sectional area ΔZ^2 is multiplied by ΔZ to obtain the volume of the domain, resulting in a cube.

Figure 3.32 shows the variation of the three-dimensional measurement domain for varying particle diameter. The $\Delta Z^3 = 10^4$ cm³ mark, where the experiments using HFSB are situated (see Figure 3.31), is crossed for $d_p \approx 0.5$ mm. This corresponds to the size of particles reported in these experiments. For a particle diameter of 1.58 mm, the measurement volume reaches 10^5 cm³ which corresponds to the size of the human body. With a diameter of 5.0 mm, the theoretical approximation approaches a domain 10^6 cm³.

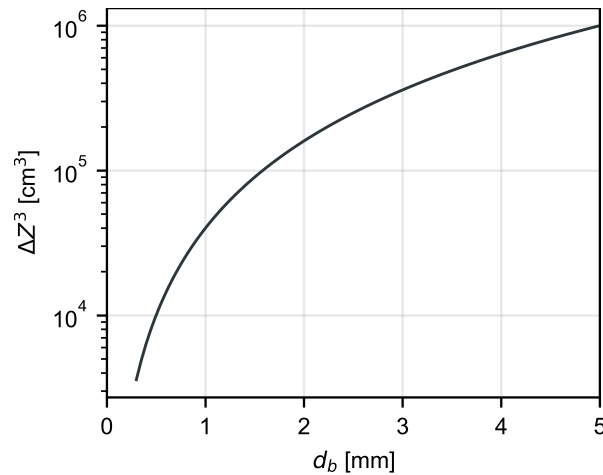


Figure 3.32: Measurement volume as a function of particle diameter for time-resolved experiments.

3.10. Discussion

Research on the fluid mechanical and optical properties of the newly developed helium-filled soap bubbles has proven that HFSB offers new opportunities for quantitative velocimetry in aerodynamic

experiments. In this section, the studies previously described in this literature survey will be critically reviewed in the same order.

[Faleiros et al. \(2019\)](#) reported that there is a linear relation between HFSB response time and $Q_{\text{BFS}}/Q_{\text{He}}$. The authors also stated that variations in the particle size may cause deviations from this trend. The particle response time is dependent on d_p^2 , which is influenced by the orifice diameter and the ratio of flow rates of helium to air. Although a linear trend may be observed from the data, it requires careful consideration of the other parameters involved, particularly while up-scaling HFSB.

For industrially motivated research in large-scale wind tunnels, it is crucial to have a short acquisition time to reduce operational costs. While the use of traversing and robotic systems does increase the maximum attainable measurement domain, its limited single field of view requires multiple volumes to be captured. This adds to the total operational time of a single measurement campaign. Increasing the field of view for a single acquisition could therefore reduce the costs per measurement. An additional remark on the use of traversing and robotic PIV systems is that it only provides knowledge on the time-averaged velocity fields due to the stitching of multiple fields of view. The resulting velocity field of the entire domain, therefore, lacks instantaneous velocity information ([Caridi 2018](#), [Jux 2017](#)).

While characterizing bubble production regimes, [Gibeau et al. \(2020\)](#) reported to include both attached satellite bubbling and polydisperse bubbling in the collective regime of bubbling. It was noted that polydisperse bubbling results in a wider particle size dispersion, but due to the rare nature of this regime, it is considered as bubbling. Since tracing fidelity, and therefore the accuracy of PIV measurements is directly affected by the particle size distribution, this classification could lead to uncertainties in the results. This is comparable to labelling attached satellite bubbling as bubbling since density variations could arise from soap droplets piggybacking onto bubbles. A possible solution may be the characterization of production regimes based on both visual observations and measurements of the coefficient of variation of the particle diameter. Applying a threshold below which an operating point is considered as bubbling could benefit the classification. Additionally, visually inspecting the production regime is only possible for a limited number of bubbles. Recording and determining the bubble size, however, can be performed at a much bigger scale. [Faleiros et al. \(2019\)](#) also mentioned that measuring glare point distance with a short illumination pulse does not suffer from nozzle exit effects, in comparison to fitting an ellipsoid to the data gathered by shadowgraphy visualizations.

Although the vertically operating nozzle from [Gibeau et al. \(2020\)](#) exhibited bubbling behaviour more often than operating it horizontally, it could suffer from several drawbacks. First, it is aerodynamically favourable to place the nozzle horizontally. The coaxial alignment of the air, helium and soap capillaries cause nozzles to have a cylindrical shape. Subsequently, the wetted surface area is increased for a vertically orientated nozzle. Second, the direction of the output flow causes additional momentum input perpendicular to the free-stream flow for a vertical nozzle. However, the velocity deficit in the wake of a horizontally orientated nozzle is filled by the momentum input of the nozzle, countering both effects having a negative influence on a downward facing nozzle. An assessment of the additional turbulence due to the rake with vertical nozzles was performed by [Gibeau et al. \(2020\)](#). However, it was reported that the analysis did not include the effect of operating nozzles. Hence, the results most likely underestimate the additional turbulence.

The observations made by [Gibeau and Ghaemi \(2018\)](#) regarding variations in particle diameter by changing air, helium and soap flow rates may be inaccurate since the operating regime of the nozzle was unknown. Since the soap film thickness is approximately 55 nm for a bubble of 300 μm , it is highly unlikely that a variation of 13.5% of the bubble size can be attributed to the increase of soap film thickness.

The scaling law presented by [Faleiros et al. \(2019\)](#), $d_p \propto (d_o Q_{\text{He}}/Q_{\text{Air}})^{1/3}$, is likely the result of data fitting. A relationship whereby a dimensional analysis shows the correct use variables in terms of units is favourable, especially when the trends can be related to physical processes. A simplified theoretical model could provide new insights between those variables.

The scaling of HFSB affects the production rate at which bubbles are emitted from the nozzle. [Faleiros](#)

et al. (2019) showed that the air flow rate is the main parameter governing the production rate of HFBS. Particles scale inversely with Q_{Air} , thus larger bubbles are produced at a lower rate. Moreover, Melling (1997) argued that the particle size limits the size of detectable turbulent scales present in the flow. The effect of particle size on the measurable flow scales can thus be seen as a high pass filter, whereby scales below the size of the particle are suppressed in the velocity fluctuations. Henceforth, PIV experiments cannot resolve turbulent scales smaller than the tracer diameter.

Some of the drawbacks of helium-filled soap bubbles over conventional micron-sized particles are the limited bubble lifetime of approximately 2 minutes and the higher sensitivity to mechanical stresses (Bosbach et al. 2009). Besides bursting beyond the bubble life-time, Huhn et al. (2017) reported a substantial decay in the scattered light intensity. It was found that the mean intensity of HFBS decays to half the original value after 10 minutes. It is also crucial to ensure that neutrally buoyant bubbles are produced, which otherwise affects data accuracy. Bosbach et al. (2009) also remarked about the limited visibility of helium-filled soap bubbles due to their transparency. However, a study by Lobutova et al. (2009) showed that the bubble soap solution can be enhanced by adding luminescent dye and illuminating the domain with UV light. As a result, a 688% increase in scattered light intensity was observed, comparing the use with and without the addition of luminescent dye. An additional drawback may be the costs of the bubble soap solution which must be purchased from third parties such as Sage Action, Inc. This could become be a bigger source of expense for larger bubbles. Finally, the use of helium as a lighter-than-air gas could pose problems in the future, as the Earth's helium storages are finite (Smith et al. 2004).

4

Experimental Set-up and Procedures

The available literature was only capable of providing a basic framework and could not directly answer the research objective as outlined in Chapter 1. For this reason, experiments are required to provide definitive answers. A small scale testing facility has been built to operate a single nozzle, which is outlined in Section 4.1. Details of the particular nozzle designs and the naming conventions are given in Section 4.2. The process of relating volumetric flow rates to the pressures and the subsequent acquisition strategy are described in Sections 4.3 and 4.4, respectively. The images captured during the experiment have to be pre-processed first, as portrayed in Section 4.5. Section 4.6 outlines the procedure of determining the distance between glare points, followed by a description of the data reduction techniques in Section 4.7. The procedure of determining the operating regime and production frequency are detailed in Sections 4.8 and 4.9. The chapter is concluded by defining the uncertainties associated with the experiments and data-processing techniques.

4.1. Experimental Apparatus

To conduct measurements on the bubbles produced by the nozzles presented in Section 4.2, a small closed-loop wind tunnel with an open test section was used, as shown in Figure 4.1. The tunnel exit is circular, with a diameter of 200 mm. A 575 W electrical motor at 1750 rpm is used to drive the air.

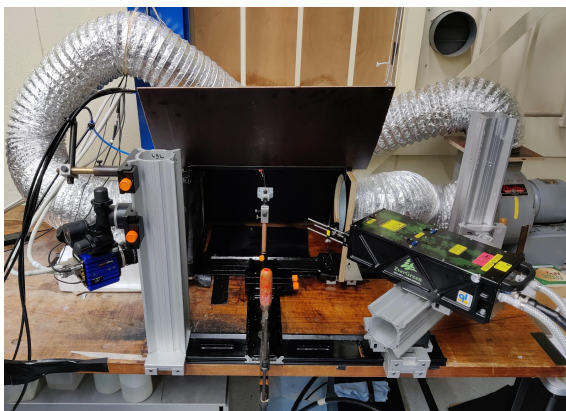


Figure 4.1: Experimental set-up of nozzle test bench, including camera (*left*) and laser (*right*).

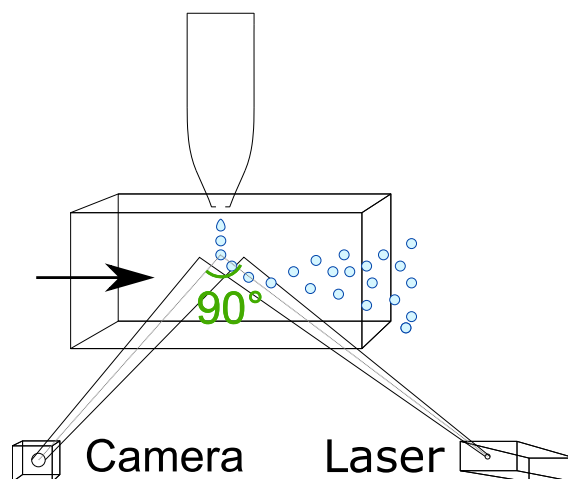


Figure 4.2: Schematic of the test-set-up, not to scale.

Nozzles are placed at the midpoint of the test section. A clamp is designed to hold nozzles in place, shown in Figure 4.3. The 3D-printed part is held in place by an M5 thread nut underneath the part, which is attached to a pole. The nozzles are orientated downwards, which has several advantages over a horizontally placed nozzle. First, axisymmetry of the coaxial flows within the nozzle is maintained. Particularly for larger bubbles, gravity may disrupt the stable formation of bubbles when the nozzle is placed horizontally. Second, any excessive soap which may block the nozzle is drained due to gravity. Hence, the nozzle may perform over a larger range of operational conditions, as results from Gibeau et al. (2019) in Section 3.4 suggest. Another feature is that in a horizontal nozzle orientation, bubbles are released directly into the wake of the clamp assembly. The air flowing around the clamp separates and recirculates within this region. The purpose of the bubbles is to follow this pattern, which may affect the recordings as bubbles produced by a previous operating condition may still be present. Furthermore, the images captured to assess the production frequency may also include more bubbles than produced successively, introducing errors in the derivation. With the cross-flow configuration, these risks are mitigated.

Bubbles are illuminated by a Quantel EverGreen laser with a nominal pulse energy of 2×200 mJ at 15 Hz with a wavelength of 532 nm. Two spherical lenses expand the beam into a cylinder with a cross section of approximately 80 mm^2 , which upper side coincides with the nozzle exit. The laser is placed at 90° angle with the imaging system, consisting of a single LaVision Imager sCMOS camera (2560 x 2160 px resolution, $6.5 \mu\text{m}$ pixel pitch, 16 bit). The camera is equipped with a 105 mm Nikkor objective with aperture settings of f/32. A small aperture is required to capture the HFSB at the correct brightness. For a 16 bit camera, pixels are saturated at 2^{16} counts. To accurately determine the peak location of glare points and compare glare point intensities between nozzles, saturated pixels must be prevented. The field of view is $47 \text{ mm} \times 55 \text{ mm}$, resulting in a magnification factor 0.3. The camera shutter and laser trigger are controlled via a LaVision Programmable Time Unit, which is connected to the acquisition PC running DaVis 8.4.0, commercial software by LaVision.

The air, helium and soap supply to the nozzle are controlled via the fluid supply unit (FSU). This unit consists of a soap container and pressure values to regulate the pressure upstream of the supply line. Compressed helium and air are used from an external source, and the latter is also used to pressurize the soap container. Mass flow meters were not available during this experiment to obtain flow rates. Instead, the fluid flow rates are obtained by relating the flow rates to the pressure set with the FSU. The calibration procedure and its results are presented in Section 4.3.

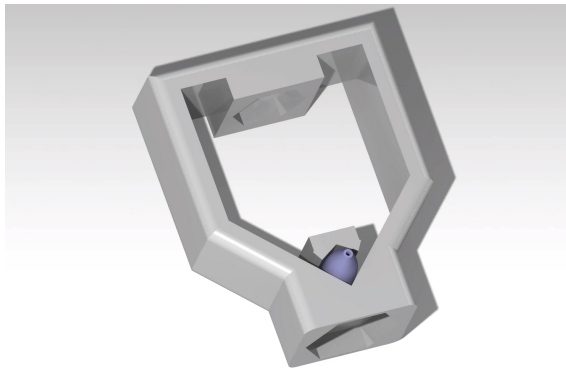


Figure 4.3: Clamp for holding HFSB nozzle generators in place.

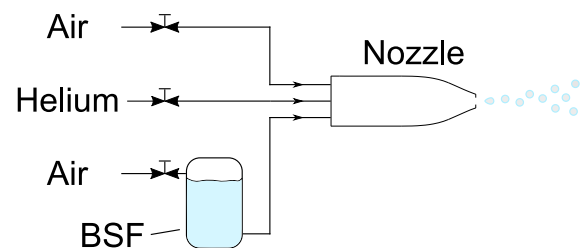


Figure 4.4: Schematic of the FSU and nozzle, not to scale.

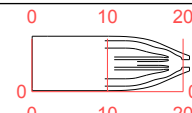
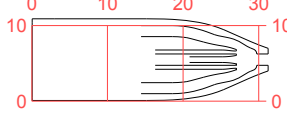
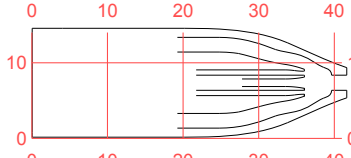
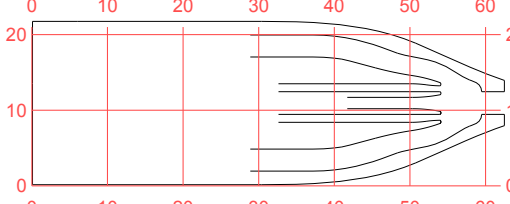
4.2. Nozzle Design

For the design of the nozzles, the baseline geometry was imported as *.stp* file and adapted accordingly. The baseline geometry serves as a reference geometry with a geometrical scaling factor of 1. 3D modelling of the geometry was performed with *CATIA V5 R21*. Nozzles were subsequently printed by

an *EnvisionTEC Perfactory 4 DDP* 3D resin printer at the *DEMO (Dienst Elektronische en Mechanische Ontwikkeling)* lab of TU Delft.

To distinguish between the different geometries, the following naming convention has been used. Every nozzle is associated with a code: S_{xx_Oyy} , where xx represents the scaling factor and $yy = d_o \times 100$, with d_o being the orifice diameter of the nozzle. The effect of geometrical scaling is investigated by scaling the baseline geometry according to Table 4.1.

Table 4.1: Nozzle naming convention for geometrically scaled nozzles, including cross-sectional views with mm scaling grid.

Name	Scaling factor	
S1_O100	1.0	
S15_O150	1.5	
S2_O200	2.0	
S3_O300	3.0	

The literature survey showed that the orifice diameter is a key parameter affecting the size of the produced bubble. A scaling factor of 0.75, 1.25 and 1.5 is therefore applied to the orifice of the base $S1_O100$ nozzle. These nozzles are identified with: $S1_O075$, $S1_O125$ and $S1_O150$, respectively. An overview of the orifice scaled nozzles with base scaling $S1$ is given in Table 4.2.

Name	Orifice diameter [mm]
S1_O075	0.75
S1_O100	1.0
S1_O125	1.25
S1_O150	1.5

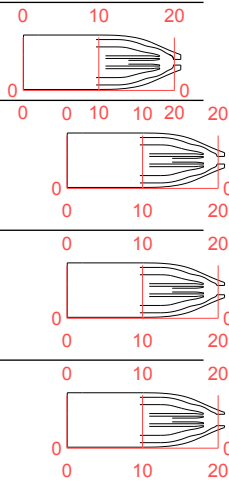


Table 4.2: Nozzle naming convention for orifice scaled S1 series nozzles, including cross-sectional views with mm scaling grid.

In addition to the nozzles described previously, scaling of the orifice has also been applied to the *S15_O150* nozzle. However, a slightly more aggressive orifice scaling factor is applied: 0.67, 1.33 and 1.67. The resulting nozzles are called *S15_O100*, *S15_O200* and *S15_O250*.

Initial experiments showed excessive soap being emitted from the nozzle for the S2 and S3 series nozzles. Soap was continuously dripping from the nozzle exit, without achieving any stable production of bubbles. It is hypothesised that this due to the scaling of the soap lines within the nozzle. Consequently, it was decided to fix the width of the soap channels within the nozzle for all geometrical scaling factors. This way, the soap channel scales linearly with the scaling factor, instead of quadratic. A prefix * is added to the nozzle name to be able to identify this updated version. Unfortunately, results were only obtained for **S2_O200* due to difficulties in the 3D printing process of the other versions. A cross-sectional view of the nozzle can be found in Figure 4.5. Table 4.3 provides an overview of all nozzles analysed.

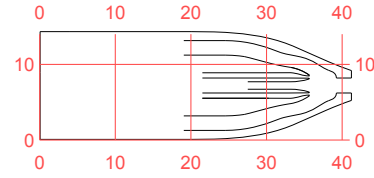


Figure 4.5: Cross-sectional view of the **S2_O200* nozzle.

Table 4.3: Overview of tested nozzles.

Name	Scaling factor	Orifice diameter [mm]
S1_O075	1.0	0.75
S1_O100	1.0	1.0
S1_O125	1.0	1.0
S1_O150	1.0	1.0
S15_O100	1.5	1.0
S15_O150	1.5	1.50
S15_O200	1.5	2.0
S15_O250	1.5	2.5
S2_O200	2.0	2.0
<i>*S2_O200</i>	2.0	2.0
S3_O300	3.0	3.0

4.3. Calibration Curves

The calibration curves relate the pressure levels set with the FSU to the fluid flow rates reaching the nozzle. For the BFS fluid, these curves are obtained by measuring the total volume of soap exiting the tubing after a set amount of time. For the gases, a different approach was chosen since its volume cannot be measured directly. For air and helium, the tubing exits were fixed at the bottom of a large tank of water. With the pressure set at a certain level, a measuring cup filled with water was placed upside down and above the exit. With the first gas bubbles entering the measuring cup, a timer was started. Upon filling the cup, the cup was moved away under the stream of bubbles and the timer was stopped simultaneously. Hereafter, the total volume of gas in the cup could be determined.

With the elapsed time and total volume at certain pressure values, mass flow can be related to pressure. The pressure drop due to the viscosity of a laminar incompressible flow through a long, slender cylinder of constant cross-section is described theoretically by the Hagen-Poiseuille equation. This equation reads:

$$\Delta p = \frac{8\mu L Q}{\pi R^4}, \quad (4.1)$$

where the pressure drop Δp between two ends of a pipe with length L and radius R can be related to the volumetric flow rate Q of a fluid with dynamic viscosity μ (Pfitzner 1976). The Hagen-Poiseuille relationship remains valid for $L/D > Re/48$, which is true for all tubing tested.

As a reference, the work of Faleiros et al. (2019) was used which analysed the performance of the *NLR* type nozzle (Figure 3.6). Both the *NLR* and *HFSB-V11.3* nozzles are based on the flow-focusing principle to produce HFSB. Furthermore, the nozzles have a similar geometry in terms of shape and orifice diameter. To obtain comparable results, calibration curves for similar flow ranges as studied by Faleiros et al. (2019) are determined. This corresponds to $Q_{\text{BFS}} = [3.6, 11]$ ml/h, $Q_{\text{Air}} = [30, 150]$ l/h and $Q_{\text{He}} = [4, 15]$ l/h.

Equation (4.1) is only valid for incompressible and laminar flows. Analysing the Mach number and Reynolds number provides information on the applicability of the linear relationship between pressure and velocity within the tubing. First, compressibility effects may arise when the Mach number, as determined by Equation (4.2), within a cylindrical tube is greater than 0.3 (Elger et al. 2019). Second, for $Re_D < 2300$, the flow within the tube is considered to be laminar. Above $Re_D = 2900$, the flow becomes turbulent (Schlichting and Gersten 2017), see Equation (4.3).

$$M = \frac{V}{a}, \quad (4.2)$$

$$Re_D = \frac{DV\rho}{\mu} = \frac{4Q\rho}{\pi D\mu}. \quad (4.3)$$

The following figures show the volume and elapsed time for various pressure settings of the air, helium and soap supply together with a linear fit and the theoretical approximation via the Hagen-Poiseuille equation is applicable, which is marked as *HP* in the following figures.

The calibration curve for the soap solution is illustrated in Figure 4.6. A linear fit is included which crosses the origin. The resulting line shows that $Q_{\text{BFS}} = 2.8P_{\text{BFS}}$. Additionally, the solution of the Hagen-Poiseuille equation is included for the specific tubing. The relatively high viscosity of the soap solution ($\mu_{\text{BFS}} = 8.0 \cdot 10^{-3}$ Pa s) causes flow velocities to remain well below the compressibility threshold. Furthermore, $Re = \mathcal{O}(1)$ and the flow is thus laminar. As a result, the theoretical line and fit curve lay almost on top of each other.

For air and helium, the calibration curves are plotted in Figures 4.7 and 4.8, respectively. The radius

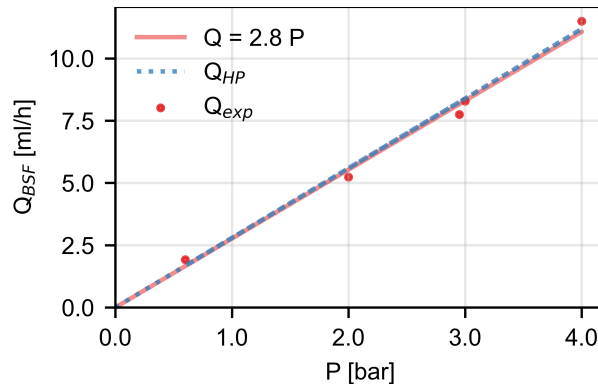


Figure 4.6: Calibration curve for BSF.

of the air tubing is more than 2.5 times the radius of the soap and helium tubing. Additionally, the viscosities of air and helium are more than 400 times lower compared to the soap solution. Both effects contribute to higher flow rates within the tubing, hence compressibility turbulence effects influence the approximation. Within the air tubing, the Mach number reaches 0.3 at $P = 0.4$ bar. Using isentropic flow relations, the density is expected to decrease by 8% with respect to near stagnant flow. However, this value rises to 37% for $P = 3.5$ bar. At $P = 0.4$ bar, $Re_D = 2700$ and is well above the turbulent threshold for $P = 1.0$ bar. Application of the Hagen-Poiseuille equation is therefore not valid, which confirms the deviation observed in Figure 4.7. The deviation from the linear trend at lower pressures is expected to be a result of measurement errors, which are more pronounced at lower flow rates. It was found during the measurements that timer could not always be initiated at the exact moment that the measuring cup was placed above the tube exit, where gas bubble column was located. The helium tube features an identical diameter, but a shorter length. At $P = 1.0$ bar, $M \approx 0.4$. For this reason, the Hagen-Poiseuille relationship is again invalid and large deviations are visible in Figure 4.8. The maximum Reynolds number is just below 500, meaning that the gas flow is fully laminar.

The slope of the Hagen-Poiseuille relationship for air is around twice as large, whereas the slope for the Hagen-Poiseuille prediction of helium is twice as small. These variations seem significant, but the linear fitted trends between Q and P are considered to be sufficiently accurate for the experiments as it includes the effects of all complex phenomena and holds well for the tested flow rates. Analysing the interactions between these phenomena to provide an answer for the deviations is beyond the scope of the project.

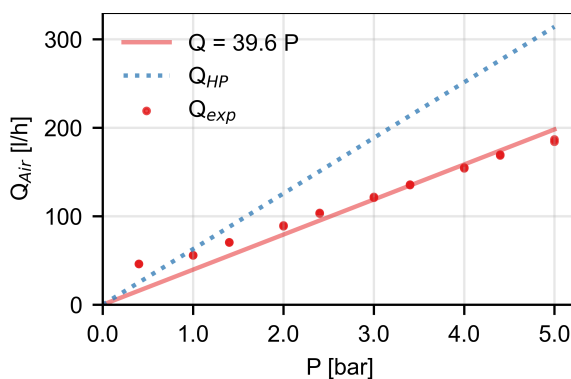


Figure 4.7: Calibration curve for air, of the S1 series nozzles.

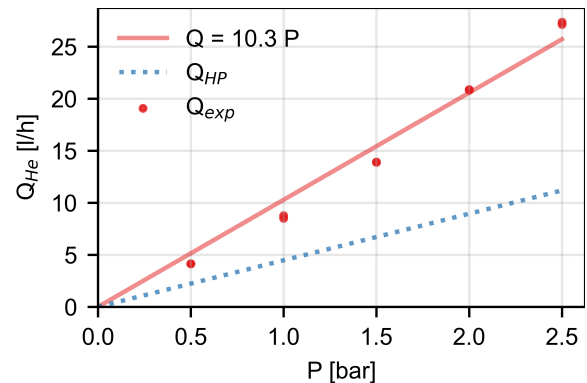


Figure 4.8: Calibration curve for helium, of the S1 series nozzles.

The linear relation is again experimentally confirmed in Figure 4.9 for a tube having a 130% larger diameter than the soap tube used in the conventional S1 nozzle. The ratio of the slopes of both BSF curves ($2.8/8.8$) and the fourth power of the ratio of radii for both tubes $(R_1/R_2)^4$ is similar within 2% uncertainty. This shows that tubes can be sized for nozzles requiring different flow rates, using the

experimentally fitted curve and theoretical proportionality of Equation (4.1).

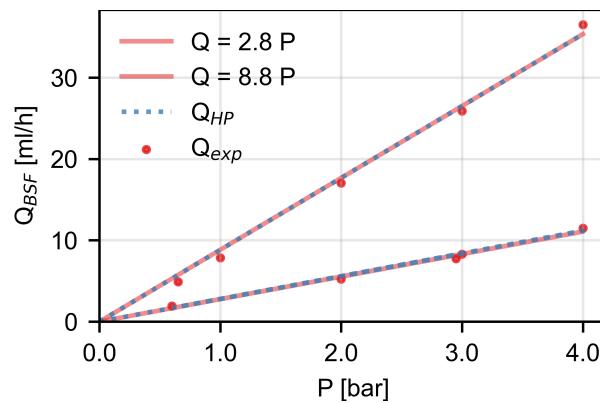


Figure 4.9: Calibration curve for both sizes of BSF tubing.

Due to the internal radii of the tubing, the flow rate is limited. If not sized correctly, the range of input conditions for the operational parameters Q_{Air} , Q_{He} and Q_{BFS} is restricted. For larger nozzles, the volumetric flow rate Q is related to the area A within the nozzle. The linear proportionality between Q and A is employed for the air, helium and soap lines within the nozzle. Thus, for a nozzle scaled by a factor $S15$, the volumetric flow rates for the base $S1$ nozzle are multiplied by the area scale: 1.5^2 . This approximation allowed the nozzle internals to remain unchanged and enabled for rapid prototyping of the designs. With the range of flow rates required for each operational parameter (air, helium & soap) and the maximum pressure on the FSU for each parameter, the size of the tubing can be determined. The maximum pressure for air and helium is limited by the range of the available pressure gauges, which is up to 6 bar. For soap, the maximum pressure is limited by the pressure limit of the soap container, which is 3.4 bar. Using the relationship between pressure and volumetric flow rate from Equation (4.1), the required tubing size for the upper limit of the volumetric flow rate at maximum pressure can be determined. Due to the limited availability of tubing with different radii, the tube length was the only available parameter for varying the flow rate.

The calibration curves for the larger tubes, used in $S15$, $S2$ and $S3$, for air and helium are presented in Figures 4.10 and 4.11, respectively. The inverse proportionality between flow rate and tube length in Equation (4.1) is assumed to remain valid for these tubes as well, despite the limitations of the Hagen-Poiseuille relationship in terms of compressibility and turbulence effects. While the flow within the helium tubing remains laminar throughout the operating range, $Re_D = 4500$ at $P = 1$ bar for air. Compressibility effects are expected to be mild for helium with $M = 0.4$ at $P = 2.0$ bar, while again for air these effects do have an influence ($M = 0.4$ at $P = 1.0$ bar). Observing the offsets shows that the Hagen-Poiseuille relationship overestimates the measured value for air, while again the inverse is true for helium. In both cases, the offset is similar to the deviations for the $S1$ nozzle.

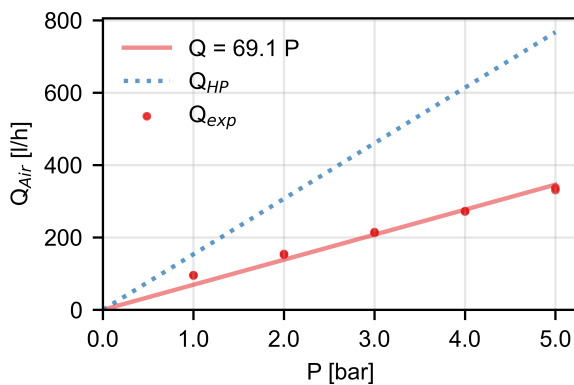


Figure 4.10: Calibration curve for air for $S15$, $S2$ and $S3$ nozzles.

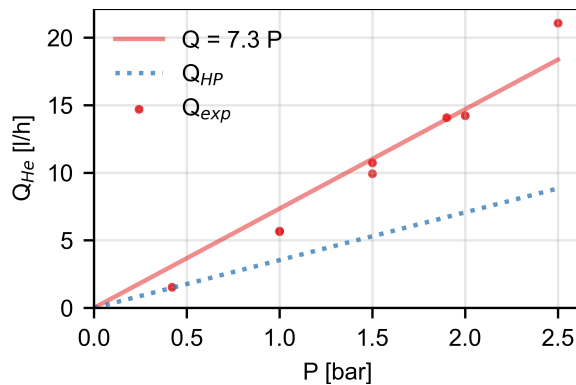


Figure 4.11: Calibration curve for helium for $S15$, $S2$ and $S3$ nozzles.

4.4. Acquisition Strategy

Results on the performance of the nozzle by [Faleiros et al. \(2019\)](#) indicate that for the highest soap rates tested ($Q_{\text{BSF}} = 8.9$ and 11.0 ml/h), the nozzle was performing in the bubbling regime over a large range of air and helium flow rates. It has therefore been decided to test the *S1* series nozzles at identical soap flow rates. Section 3.5.2 emphasized the importance of achieving neutral buoyancy on the measurement accuracy of PIV experiments using HFBS as tracers. For a given flow rate of soap, the helium flow rate can be derived by relating the bubble density to the density of air in Equation (3.4). Using the values in Table 3.1, the theoretical neutrally buoyancy condition is achieved at $Q_{\text{He}}/Q_{\text{BSF}} = 1095$. Bubbles are produced neutrally buoyant, under the assumption that there is no leakage, at helium flow rates of 9.7 and 12.0 l/h for the previously mentioned values of Q_{BSF} . For the geometrically scaled nozzles, the flow rates are multiplied by the area scale as previously described in Section 4.3. For the *S2 nozzle with updates internals, two more operating conditions are included which correspond to the neutrally buoyant conditions of the *S1* nozzle.

The last remaining parameter, Q_{Air} , has a significant influence on the operating regime and particle diameter as the studies of [Faleiros et al. \(2019\)](#) and [Gibeau et al. \(2020\)](#) have reported. A sampling strategy of ΔQ_{Air} has therefore been chosen whereby for each set of $(Q_{\text{BSF}}, Q_{\text{He}})$, the airflow rate is increased until the nozzle ceases to produce bubbles. Depending on the range of Q_{Air} , the step size is varied from 30 l/h for the *S1* and *S15* series nozzles to 60 l/h for the *S2* and for the *S3* series to 180 l/h. Tests are denoted by $T_{xx.yy}$, where xx represents a particular neutrally buoyant condition $(Q_{\text{BSF}}, Q_{\text{He}})$ for that nozzle, while yy indicates the set-point of Q_{Air} . Thus, $T_{xx.1}$ to $T_{xx.14}$ indicate the first to fourteenth set-point of Q_{Air} . The test matrix for all nozzles is presented in Table 4.4. The test matrix, converted to pressure values, can be found in the Appendix, Tables A.1 and A.2. As previously described, the flow rates for larger nozzles are obtained by multiplying the flow rates of the base nozzle with the area scale.

Starting at the lowest set-point of Q_{Air} for each test condition, recordings were taken when the nozzle was producing any kind of bubbles in a stable, continuous manner. Before recordings were initiated, a delay of approximately one minute was applied after setting the desired pressure valves on the FSU to ensure the system is settled. Then, 500 images were taken at a recording rate of 15 Hz. For every tested condition, it was noted whether the nozzle was working (*w*) or non-working (*nw*). If the nozzle stopped producing bubbles after increasing the airflow rate by ΔQ_{Air} , the next set-point was initiated by changing the helium and soap flow rates or switching nozzles. This was also done when the pressure P_{Air} could not be set higher due to gauge or maximum container pressure limits.

Table 4.4: Test Matrix for nozzles with a scaling factor of 1.5, 2 and 3 and varying orifice sizes.

Nozzle	Test no.	Q_{BSF} [ml/h]	Q_{He} [l/h]	ΔQ_{Air} [l/h]
S1_O075	T1	8.9	9.7	30
	T2	11.0	12.0	30
S1_O100	T3	8.9	9.7	30
	T4	11.0	12.0	30
S1_O125	T5	8.9	9.7	30
	T6	11.0	12.0	30
S1_O150	T7	8.9	9.7	30
	T8	11.0	12.0	30
S15_O100	T9	20	21.9	30
	T10	24.8	27.1	30
S15_O150	T11	20	21.9	30
	T12	24.8	27.1	30
S15_O200	T13	20	21.9	30
	T13	24.8	27.1	30
S15_O250	T15	20	21.9	30
	T16	24.8	27.1	30
S2_O200	T17	35.6	39.0	60
	T18	44.0	48.2	60
*S2_O200	T19	17.8	19.5	60
	T20	22.0	24.1	60
*S2_O200	T21	35.6	39.0	60
	T22	44.0	48.2	60
S3_O300	T23	80.1	87.7	180
	T24	99	108.4	180

4.5. Image Pre-processing

Before peaks from glare points can be analysed, images are pre-processed in Python 3.8 according to four steps:

1. Loading *.im7* files
2. Cropping
3. Reducing background noise
4. Normalizing

Captured images are stored as *.im7* files. This required the use of the *ReadIM* module ¹, which reads native DaVis file types. After the images are loaded as a grayscale image array, CPU and memory requirements are lowered by cropping the image. Consequently, a region of approximately 30 mm² is used for processing. In the next step, image pixels are normalized to the range [0,1]. Background noise, such as electronic camera noise and reflections, is filtered using a subtract minimum filter over three images. The filter length is based on a trade-off between noise reduction and processing speed. Since the background noise is mainly static, three images already provided good results while still maintaining an acceptable level of computational effort. Figure 4.12 exemplifies a single image with raw data, background noise and the pre-processed result.

¹<https://pypi.org/project/ReadIM/>

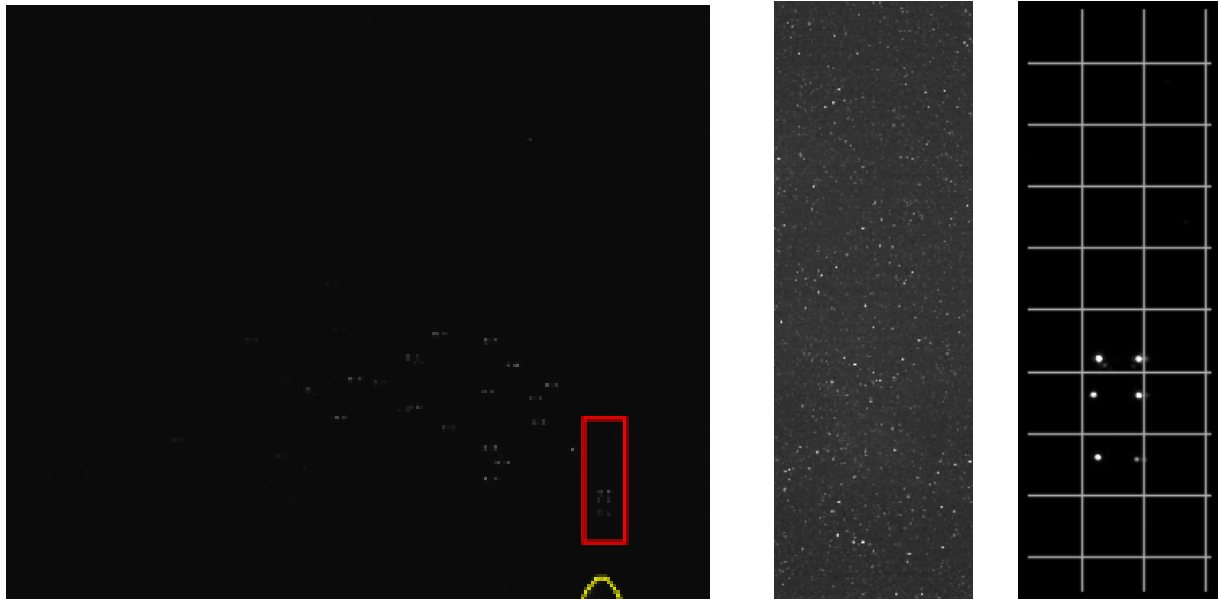


Figure 4.12: Image pre-processing steps. Note that relative intensity between images changes. *Left*: Raw image with highlighted cropping region (red) and nozzle (yellow). *Middle*: Minimum background noise over three images. *Right*: Processed image, with 1x1 mm grid.

4.6. Bubble diameter determination

After pre-processing, the image can be used to determine the location of the glare points and subsequently the glare point distance d_g . The glare point distance method has been proven to be a reliable and accurate approach to determine the bubble diameter in a comparison to shadow visualizations whereby an ellipse is fitted to the edge of the recorded bubble shadow. [Faleiros et al. \(2019, p. 15\)](#) reported that *"No significant difference is observed between the two methods, demonstrating control and repeatability in both experiments"*. The method itself can thus be regarded as a reliable tool to determine the size of the bubble. The exact procedure, continuing on the previously mentioned steps, consists of 5 phases:

5. Pixel integer peak finding
6. Peak sorting
7. 2D Gaussian peak interpolation
8. Peak pairing
9. Glare point distance determination

The location of the local maxima in the pre-processed image are determined via the `peak_local_max` function from the `scikit-image` module. This function returns the location to pixel accuracy. The pre-processed image still contains various isolated maxima. Furthermore, if pairs of maxima are located in proximity of one another, it is difficult to identify which two glare points corresponds to the same bubble. Phase 6 consists of an additional sorting stage to find and remove peaks based on two conditions. For each located peak, a bounding box centred around this peak. Its width and height are predefined to be 100x5 pixels. The first condition is met when only a single peak is found within the box. The second is true when more than 2 peaks are found within the predefined box. The complying peaks are removed and the conditions are re-evaluated for the remaining peaks, until all peaks satisfy the bounding box criteria. This procedure is shown in Figure 4.13. The remaining peaks are assumed to only consist of peak pairs. In the next phase, the location of glare points are determined to sub-pixel accuracy by applying a 2D Gaussian fit function from the `Photutils` package². After updating the peak locations, pairs of peaks are linked which correspond to a single bubble. With this information, the glare point

²<https://photutils.readthedocs.io/en/stable/index.html>

distance is determined and returned from the function. The resulting distance is then multiplied by $\sqrt{2}$ to obtain the bubble diameter, following Equation (3.6).

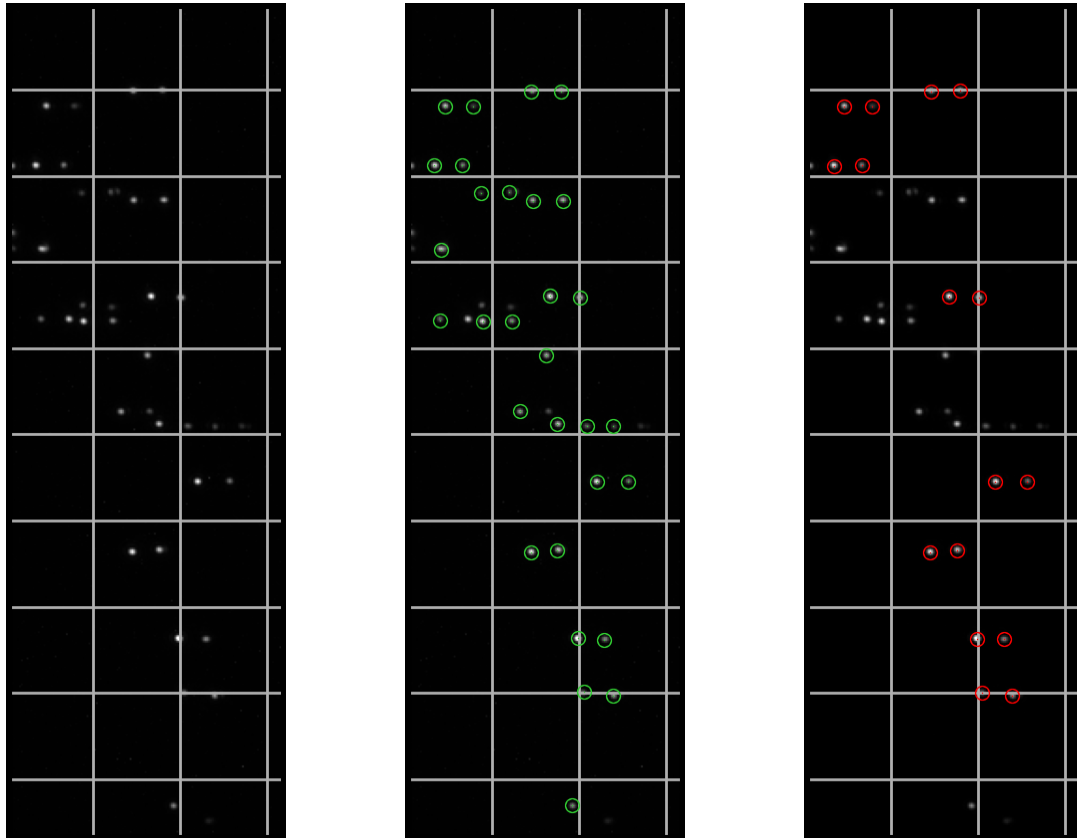


Figure 4.13: Peak sorting step on post-processed images with 1x1 mm grid. *Left:* Raw image. *Middle:* Initial peaks found at pixel accuracy. *Right:* Remaining 2D Gaussian interpolated peaks after the sorting phase.



Figure 4.14: Initial peak location with integer pixel accuracy.

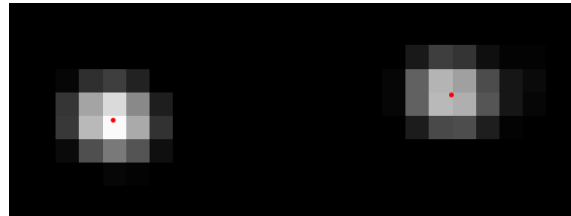


Figure 4.15: 2D Gaussian interpolated peak location.

The tenth step of the process is to convert the glare point distance into physical units. This requires a calibration image to relate image pixels to physical millimetres. The resulting magnification is 0.0216 mm/px. With the glare point distance, the bubble diameter is calculated according to Equation (3.6). A flowchart of the code that was used to derive the bubble diameter from raw images is given in Figure B.1.

4.7. Data Reduction Techniques

For distributions of HFSB diameters with a single mode, a Gaussian least-squares fit is applied, as can be observed in Figure 4.16. For bi-modally distributed histograms as shown in Figure 4.17, a Gaussian least-squares fit is used to both modes. After determining the mean and standard deviation of the Gaussian fit, a Z-score outlier filter with 3σ is implemented, which reads as:

$$\text{remove } d_{d,i} \text{ if } -3 < z_i < 3 \text{ for } z_i = \frac{d_{d,i} - \mu}{\sigma},$$

where $d_{d,i}$ is the i th bubble diameter sample. The Gaussian least-squares fit is once more applied, and the resulting mean and standard deviations of the modes are used for further processing and calculating the coefficient of variation of the bubble diameter.

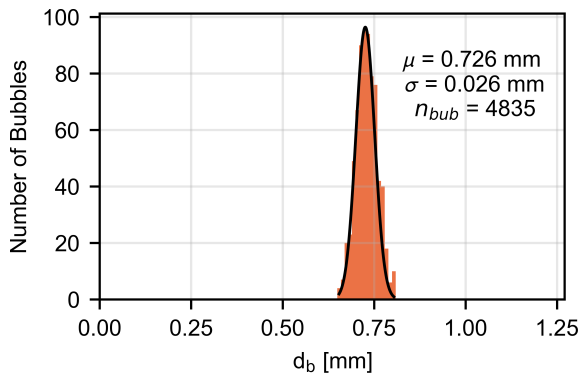


Figure 4.16: Unimodal distribution of HFSB diameters for *S2_O200, test T21.6.

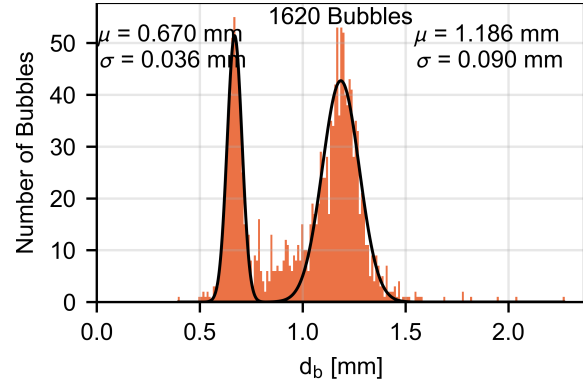


Figure 4.17: Bimodal distribution of HFSB diameters for *S2_O200, test T21.5.

4.8. Operating Regime Determination

To determine the operating regime of the nozzle at a certain operating point (ΔQ_{Air} , Q_{He} , Q_{BSF}), the coefficient of variation of the bubble diameter is determined. As described in Section 3.4, for this method the mean bubble diameter and standard deviation are used, which are computed according to Section 4.7. [Faleiros et al. \(2019\)](#) reported a deviation in the coefficient of variation of the bubble diameter for the two main operating regimes: bubbling and jetting. As previously mentioned, for bubbling it was found that $CV_d \approx 2 - 3\%$, while for jetting $CV_d \approx 13\%$. Figures 4.18 and 4.19 show histograms of the bubble diameter in case of bubbling and jetting, respectively. For raw image data, no visual differences could be found between the bubbling and jetting regimes. The distinction between jetting and bubbling will therefore be solely based on the dispersion of the bubble diameter.

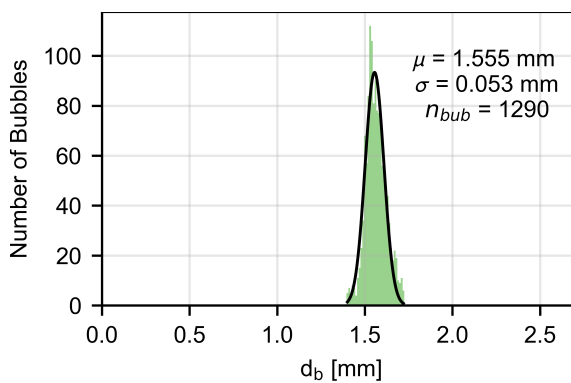


Figure 4.18: Distribution of HFSB diameters for S15_O150, test T11.1 whereby $CV_d = 3.4\%$.

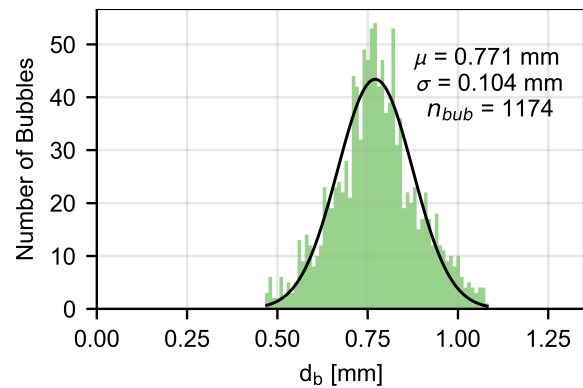


Figure 4.19: Distribution of HFSB diameters for S15_O150, test T11.7 whereby $CV_d = 13.5\%$.

4.9. Production Frequency

Additional recordings were performed in double-frame mode to analyse the production frequency of the nozzle generator at several operational conditions. In total, 100 images were captured at various

separation times, depending on the jet velocity v_{jet} . The production frequency f is derived from

$$f = \frac{v_{\text{jet}}}{\lambda M}. \quad (4.4)$$

Here, v_{jet} is the mean velocity in a rectangular area in front of the nozzle exit. PTV in DaVis 10.1.2 is employed to track particles and compute the velocity field, whereby images were pre-processed using a subtract minimum filter. Furthermore, λ is the distance between successive bubbles within the same frame. As the distance is measured in pixel units, the magnification factor M is introduced. The results of this analysis are described in Chapter 5.

4.10. Uncertainty Analysis

This section attempts to quantify the uncertainties of the experimental campaign. Quantifiable uncertainties can be grouped per project phase:

- Preparation
- Execution
- Analysis

During the preparation phase, the calibration curves for each tube of the *S1* series nozzles are made. Uncertainties arise from reading the fluid or gas volume levels after a certain elapsed time. For soap, the fluid level was read off and interpolated between intermediate marks of a 2 mm graduated cylinder. The resulting error is estimated to be 2%. Air and helium calibration curves are obtained by measuring the gas volume within a measuring cup of 1950 mm with interval marks at 25 mm. The resulting uncertainty is 1.3%. Another source of error during the calibration phase is introduced by determining the correct length of the tube used for calibration as well as for the nozzle itself. It is estimated that this error is around 1.5% for both cases. The last quantifiable error is the difference between the linear fit and the data points. On average, this is approximately 6% of the fitted curve for the upper half of the tested flow rates.

The pressure values, determined by scaling the base *S1* nozzle and converting via the calibration curves, cannot be set digitally on the FSU. Instead, analogue gauges are used which have finite interval between marks. For all gauges, the difference between intermediate intervals was 0.1 bar. The pressure values were therefore rounded to one decimal values. This introduces a relative error between actual and rounded value up to $\pm 7\%$ at the lowest pressure setting. For higher flow rates, this error reduces to 0.8%.

In the last phase, uncertainties arise in the estimation of the peak location of the glare point intensity distribution. The error is determined relative to the distance between glare points. The uncertainty of the initial peak finding algorithm, which is accurate to integer pixel values, ranges between 2.9% for the smallest measured bubbles and 0.6% for the largest diameters for unsaturated pixels. With the implementation of the 2D Gaussian interpolation, uncertainties are assumed to be negligible. When pixels are saturated however, the algorithm cannot determine the peak location accurately, since there are no gradients between pixels. For a 2x2 saturated glare point, uncertainties for the smallest and largest bubble size are 5.8% and 1.2%. Likewise, for a glare point with 3x3 saturated pixels, the uncertainty is 11.8% and 2.3%. When both glare points of a single bubble are saturated, this uncertainty must be multiplied by $\sqrt{2}$. Nonetheless, it is most unlikely that saturated pixels occur for the smallest particles sizes since the amount of light that is scattered scales with the square of the particle diameter. From the data, it was observed that pixel saturation was mainly occurring for larger particles and thus the relative uncertainty can be estimated to range between 0.6% to 2.3%. Figures 4.20 and 4.21 show the pre-processed image data for a relatively large and small bubble, respectively.

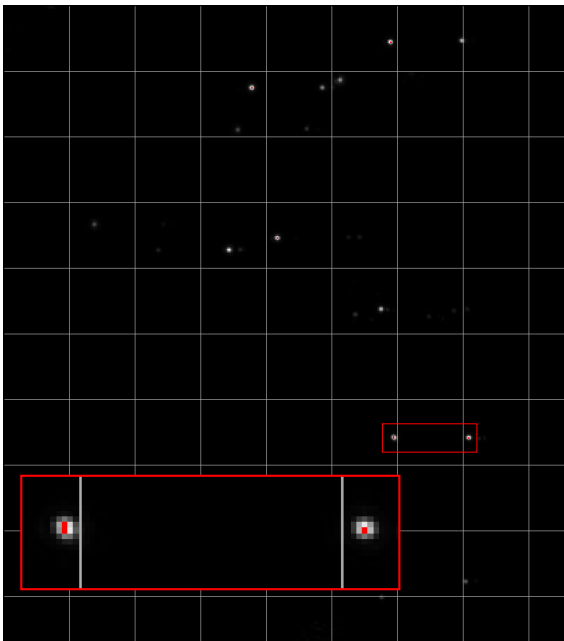


Figure 4.20: 2D intensity distribution of a large bubble of *S15_O150* during test *T11.1* with saturated peaks (*red*).

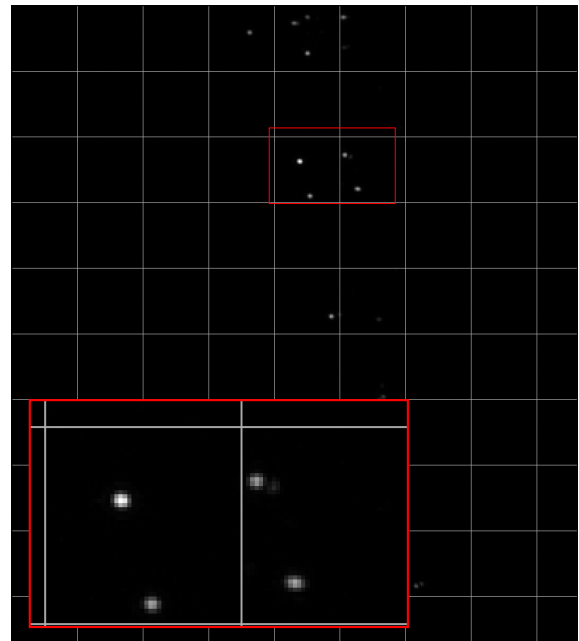


Figure 4.21: 2D intensity distribution of small bubbles of *S15_O150* during test *T11.7* without saturated peaks.

5

Results & Discussion

Results of the various tested nozzles are presented in this chapter. A starting point of the discussion is the production regime maps, qualitatively showing the nozzle performance in terms of working and non-working operating points. Hereafter, the outcome of the glare point detection algorithm is presented in terms of mean bubble diameter per nozzle. Previous research has shown that air, helium and the orifice diameter are the main parameters governing the HFSB size, which will be analysed in further detail (Faleiros et al. 2019, Gibeau et al. 2019). The results are subsequently benchmarked against a simplified model approximating the bubble diameter as a function of the orifice diameter and the flow rates of helium and air. This is followed by a validation of the data with the NLR-type nozzle used in the work of Faleiros et al. (2019). Conclusively, the disparity of the bubble diameter is introduced, expressed by the coefficient of variation of the bubble diameter.

5.1. General Nozzle Performance

The performance of the nozzles tested is initially assessed by observing whether the nozzle is producing bubbles (*working*) or not (*non-working*). A distinction based on the operating regime (bubbling or jetting) can be made using the information in the subsequent sections. For the *working* operating points, data is recorded and used for the determination of the bubble diameter. For each considered case, the soap and helium mass flow has been adjusted according to Equation (3.4) with $Q_{\text{He}}/Q_{\text{BSF}} = 1095$ and the values in Table 3.1 to obtain neutrally buoyant bubbles. It is expected that small deviations of around 5% from the neutrally buoyant condition do not alter the performance of the nozzle.

As described in Section 4.3, the range of Q_{Air} for the *S1* series nozzles is based on the tested range in the study by Faleiros et al. (2019), which was 30 to 150 l/h. This range is extended up to 215 l/h in Figure 5.1. The *S1_O075* nozzle is the only nozzle not capable of reaching this flow rate, already ceasing to produce bubbles from approximately 50 l/h onwards, see Figure 5.1a. It was observed during the experiments that for higher flow rates of air, this nozzle exhibited a spraying behaviour whereby a fine mist of bubble fluid solution was emitted. As the orifice diameter of the nozzle is increased to 1 mm, the amount of working operating points increases. The lack of working operating points may thus be a result of the high contraction ratio of the *S1_O075* nozzle.

Results for the *S15* series nozzles in Figure 5.2 feature similar characteristics as the *S1* series. For the nozzle with the highest contraction ratio of this series, the *S15_O100* nozzle, similar spraying behaviour is observed. As the orifice diameter increases, the nozzle is working nominally more often. Both Figures 5.2c and 5.2d show that the nozzles have identical performance in terms of working operating points between $Q_{\text{Air}} = 62$ l/h and 387 l/h. At low air flow rates, the nozzle exhibits a foaming behaviour. This has been an indicator for low gas flow rates throughout the experimental campaign.

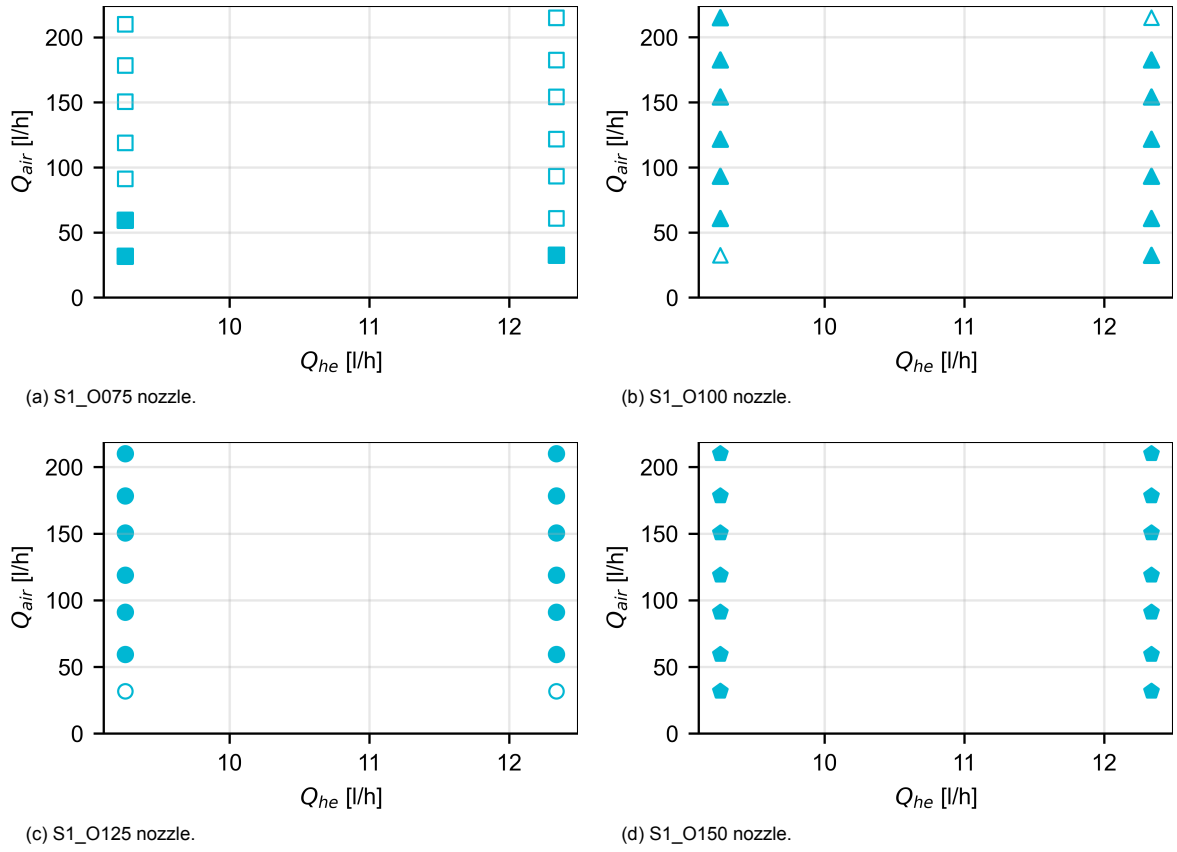


Figure 5.1: Production regimes for series S1 nozzles, whereby filled and empty markers indicate working and non-working conditions, respectively.

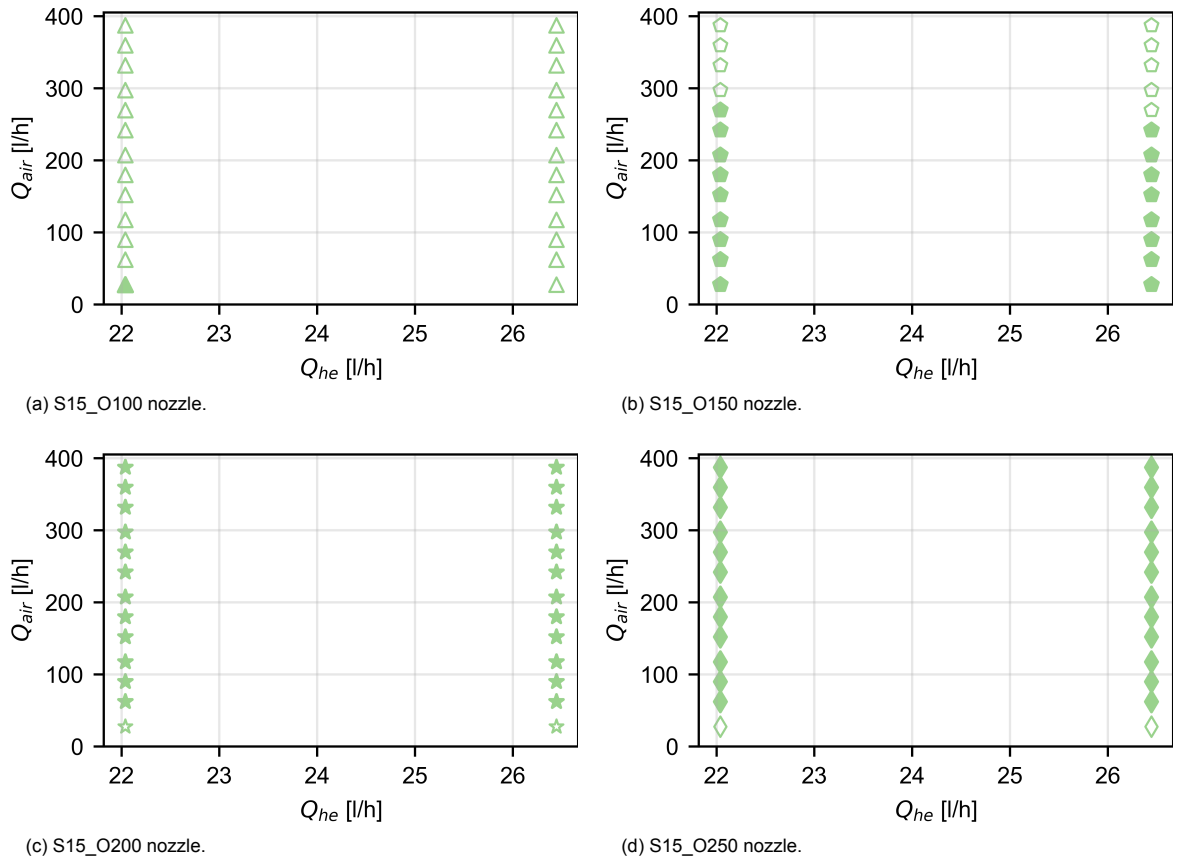


Figure 5.2: Production regimes for series S15 nozzles, whereby filled and empty markers indicate working and non-working conditions, respectively.

For the S2 scale series in Figure 5.3a, the width of the internal soap channel causes bubbles to be produced only at higher flow rates. During the experiments, it was seen that for most of the operating conditions soap was continuously dripping from the nozzle, indicating soap excess. By updating the internal geometry of the soap channel excess soap is minimized and the number of working operating points is greatly increased, see Figure 5.3b. For all nozzles, changes in the helium and soap flow rates to maintain the neutral buoyancy condition does not impact the overall performance.

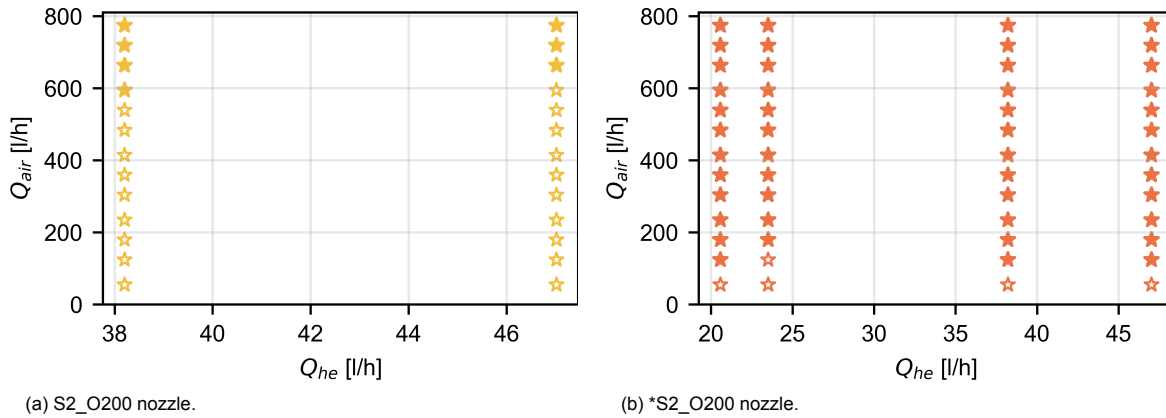


Figure 5.3: Production regimes for series S2 nozzles, whereby coloured and gray markers indicate working and non-working conditions, respectively.

The results for the scale S3 series nozzle are found in Figure 5.4. For each tested operating condition, this nozzle did not produce any bubbles at all. Even at higher flow rates, soap was dripping from the nozzle, indicating that the internal soap channels should not be scaled geometrically. An *S3 nozzle was manufactured but production deficiencies made this nozzle unusable.

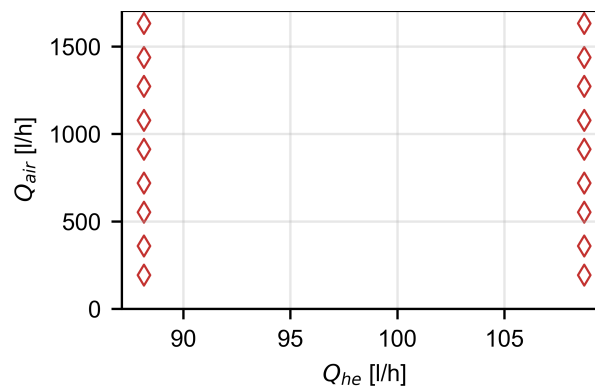


Figure 5.4: Production regimes for series S3 nozzle, whereby filled and empty markers indicate working and non-working conditions, respectively.

5.2. Mean Bubble Diameter

For each working operating point as discussed in Section 5.1, recordings are made to capture both glare points and derive the mean bubble diameter. No distinction has been made regarding the production regime; the data consists of both jetting and bubbling operating points. For uni-modal distributions of the bubble diameter (Figure 4.16), the mean and standard deviation follow from the Gaussian regression. For bi- and poly-modal distributions, however, the mode with the highest amplitude is chosen.

The analysis of the bubble diameter comprises two parts. In the first part, the results for all operating conditions are summarized by presenting the bubble diameter as a function of the air flow rate. Several

curves are analysed in-depth and an axis normalization is applied. In the second part, a first-order theoretical approximation is presented and compared to the data of the *S2_O200 nozzle.

As the supply of air is increased, the annular jet of helium and soap is extruded at greater effort and forced through the orifice. This causes the annular jet to shrink, whereby instabilities cause the jet to break up into bubbles. Thus for a higher supply of air, this effect is more pronounced, leading to smaller bubbles produced at higher rates. The results depicted in Figure 5.5 confirm this trend, following the findings of the study by Faleiros et al. (2019).

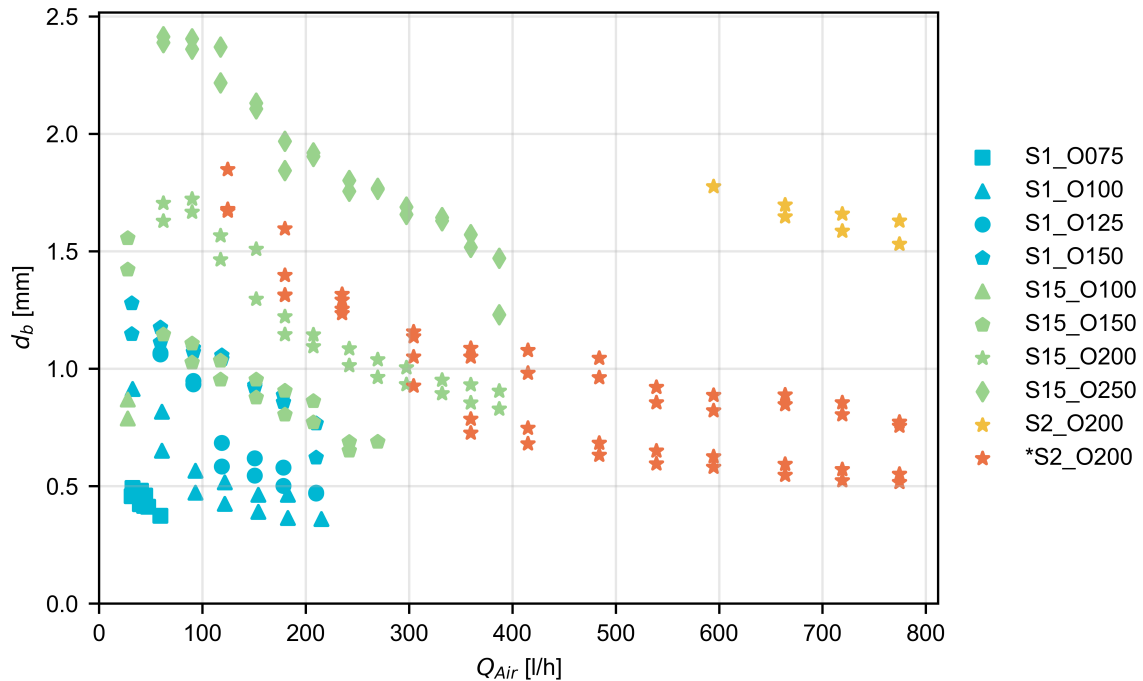


Figure 5.5: HFSB diameter variation as a function of Q_{Air} for all tested nozzles.

The four different neutrally buoyant conditions of the *S2_O200 nozzle are isolated to analyse the effect of the air flow rate in more detail, as plotted in Figure 5.6. For $Q_{Air} < 350$ l/h, the lines for $Q_{He} = 20$ and 23 l/h show a steep decrease in particle diameter for increasing airflow rate. After $Q_{Air} = 350$ l/h, the curves exhibit a more 'converged' or stable behaviour. An upward shift is visible for increasing Q_{He} . Between $Q_{Air} = 400$ and 800 l/h, the bubble diameter drops about 0.25 mm for all neutrally buoyant conditions.

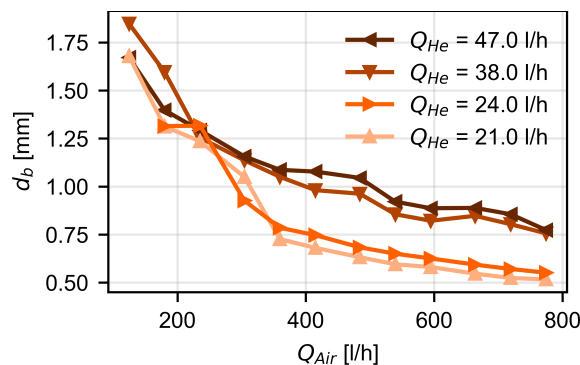


Figure 5.6: HFSB diameter variation as a function of Q_{Air} for the *S2_O200 nozzle.

The same data is used in Figure 5.7, illustrating the effect of Q_{He} on d_b more clearly. Compared to Q_{Air} , Q_{He} causes the largest variations in the bubble diameter. This is expected since helium is the main gas comprising the bubble's volume. On average, d_b increases with 0.27 mm for $\Delta Q_{He} = 26$ l/h. The

bubble's volume is assumed to be comprised only of helium, and thus $Q_{\text{He}} \propto V_b$. Leakage of helium and the variation of the production frequency with Q_{He} is assumed to be negligible. Subsequently, the volume of the bubble is related to the bubble diameter, resulting in $Q_{\text{He}} \propto V_b \propto d_b^3$. Figure 5.7 includes the expected variation of d_b based on the difference between $Q_{\text{He}} = 22$ l/h and 47 l/h, relative to the initial point. With particle sizes not exceeding $d_b/d_o > 1$, this explains why for lower air flow rates, increasing helium does not produce larger bubbles. At higher flow rates of air, the relationship between the flow rate of helium and the bubble diameter underestimates the actual bubble diameter. These deviations are, however, much smaller compared to the offsets at lower flow rates of air.

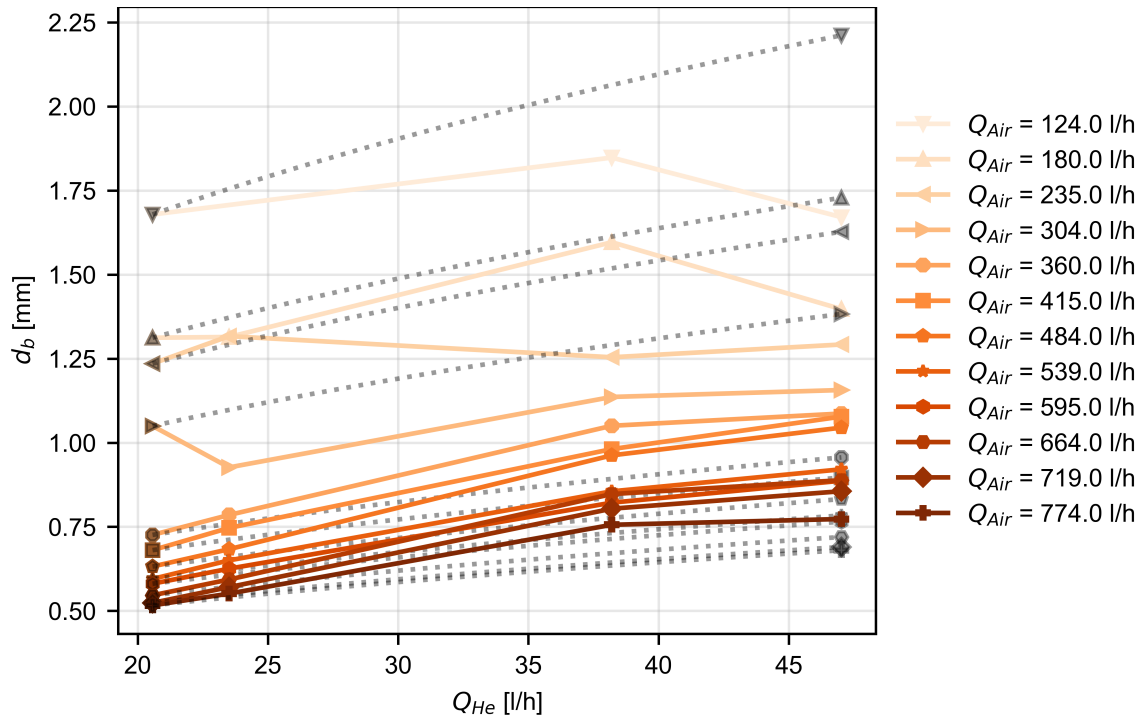


Figure 5.7: HFSB diameter variation as a function of Q_{He} for the *S2_O200 nozzle. The black marks, slightly offset for clarity, indicate the expected values based on proportionality between Q_{He} and d_b .

The physical units on the axes of Figure 5.5 can be normalized by Q_{He} and d_o , as shown in Figure 5.6. The data for the S1_O100, S1_O125, S15_O150, S15_O200 and *S2_O200 nozzles collapse well into a single curve. Nozzles not following the hyperbolic trend are the S1_O075, S15_O100, S1_O150, S15_O250 and S2_O200 nozzles.

An attempt is made to find a reason for these deviations. However, caution must be taken while interpreting the data due to the limited amount of operational conditions that are available. For example, the S15_O100 only has two data points. This nozzle and the S1_O075 and S2_O200 nozzles, feature an orifice diameter d_o much smaller than the internal soap channel diameter d_{BSF} . Specifically, $2d_o < d_{\text{BSF}}$. Nevertheless, this does not explain the deviations of the S15_O250 for which $d_{\text{BSF}} \approx d_o$. This shows that (relative) internal nozzle geometry must be subject to further investigation to fully understand the deviations from the observed hyperbolic trend. Filtering data based on the dispersion of the particle diameter, which will be discussed in the following section, did not provide any new insights. The deviations from the approximation are thus not a consequence of the production regime of the nozzle. Other observations include that the particle diameter never exceeds the orifice diameter, apart from a single case. Extrapolating the hyperbolic trend of the *S2_O200 nozzle shows a possible lower limit of $d_b/d_o \approx 0.2$. Similar asymptotic behaviour is seen for $(Q_{\text{Air}}, Q_{\text{He}}) \rightarrow 0$, as bubble production is not possible when the flow rates are minimal.

The hyperbolic trend for the *S2_O200 nozzle, having the most number of data points, is analysed in more detail using a basic theoretical model. Figure 5.9 schematically illustrates the parameters used in this model.

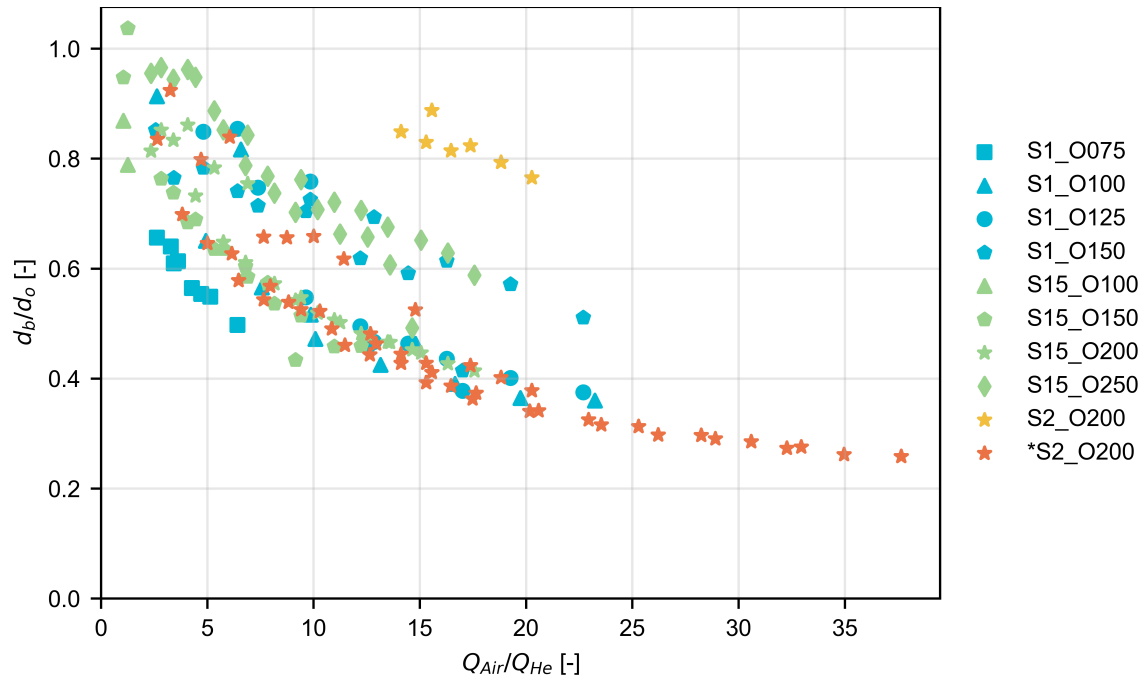


Figure 5.8: Normalized HFSB diameter variation as a function of Q_{Air}/Q_{He} for all tested nozzles.

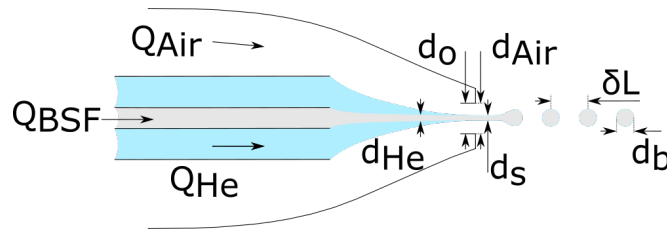


Figure 5.9: Parameter definitions used in the model. Figure not to scale.

To find a relationship for the bubble diameter d_b , bubble formation is assumed to occur outside the nozzle. This simplifies the analysis since the streamtube within the orifice can be related to the orifice diameter d_o . Moreover, the flow of bubble fluid solutions is negligible compared to air and helium ($Q_{BSF} \ll Q_{Air}, Q_{He}$). The mass flux through the orifice can be related to the cross-sectional area according to

$$\frac{Q_{He}}{Q_{Air}} = \frac{u_{He} A_{He}}{u_{Air} A_{Air}}. \quad (5.1)$$

This relation can be simplified by assuming that the velocities within the orifice for each fluid is the same. Thus, the velocity profile is a vertical line and $u_{He} = u_{Air}$. This is valid when there is no shear between the air and soap solution. The ratio of flow rates thus only depends on the area ratio

$$\frac{Q_{He}}{Q_{Air}} \approx \frac{A_{He}}{A_{Air}}. \quad (5.2)$$

While the helium streamtube is cylindrical, air behaves as an annulus within its core the helium streamtube. A_{Air} is therefore dependent on the diameters of helium and air

$$\frac{Q_{He}}{Q_{Air}} \approx \frac{A_{He}}{A_{Air}} \approx \frac{d_{He}^2}{d_{Air}^2 - d_{He}^2}. \quad (5.3)$$

The diameter of the helium flow is rewritten with the streamtube diameter: $d_{\text{He}} = d_s$. Furthermore, $d_{\text{Air}} = d_o$. Solving Equation (5.3) for d_{He} and rewriting results in

$$d_s \approx d_o \sqrt{\frac{Q_{\text{He}}}{Q_{\text{Air}} + Q_{\text{He}}}}. \quad (5.4)$$

Equation (5.4) is written in terms of the streamtube diameter, whereas only the bubble diameter d_b is obtained from measurements. To relate the streamtube diameter to the bubble diameter, the breakup of a cylindrical jet into spheres is considered. Each sub-cylinder of length δL collapses into a sphere with volume $V_b = \frac{\pi}{6}d_b^3$. The volume of each sub-cylinder is

$$\delta V_s = \frac{\pi}{4}d_s^2\delta L, \quad (5.5)$$

whereby an approximation for δL is found by assuming that the lateral surface area of the helium streamtube can be equated to the sphere's surface area. This results in the system of equations

$$\begin{cases} \pi d_s \delta L = \pi d_b^2, \\ \frac{\pi}{4} d_s^2 \delta L = \frac{\pi}{6} d_b^3. \end{cases} \quad (5.6)$$

The system can be solved for d_s and δL as functions of d_b , resulting in

$$\begin{cases} d_s = \frac{2}{3} d_b, \\ \delta L = \frac{3}{2} d_b. \end{cases} \quad (5.7)$$

The expression for d_s is substituted in Equation (5.4) and the relationship for the particle diameter will read

$$\frac{d_b}{d_o} \approx \frac{3}{2} \sqrt{\frac{Q_{\text{He}}}{Q_{\text{Air}} + Q_{\text{He}}}}. \quad (5.8)$$

The particle diameter normalized by the orifice diameter is proportional to the square root of the ratio between the helium and sum of flow rates.

The theoretical relationship is compared to a trendline fitting the data from the *S2_O200 nozzle. Using the same proportionality between variables as Equation (5.8), given by $y = c(Q_{\text{He}}/(Q_{\text{Air}} + Q_{\text{He}}))^b$, has coefficients $c = 1.83$ and $b = 0.52$ with $R^2 = 0.89$.

Both curves, together with the data of the *S2_O200 nozzle, are presented in Figure 5.10. The theoretical approximation underestimates the bubble diameter between 10% to 15% compared to the fitted curve and can therefore be said to be a lower limit of the particle diameter.

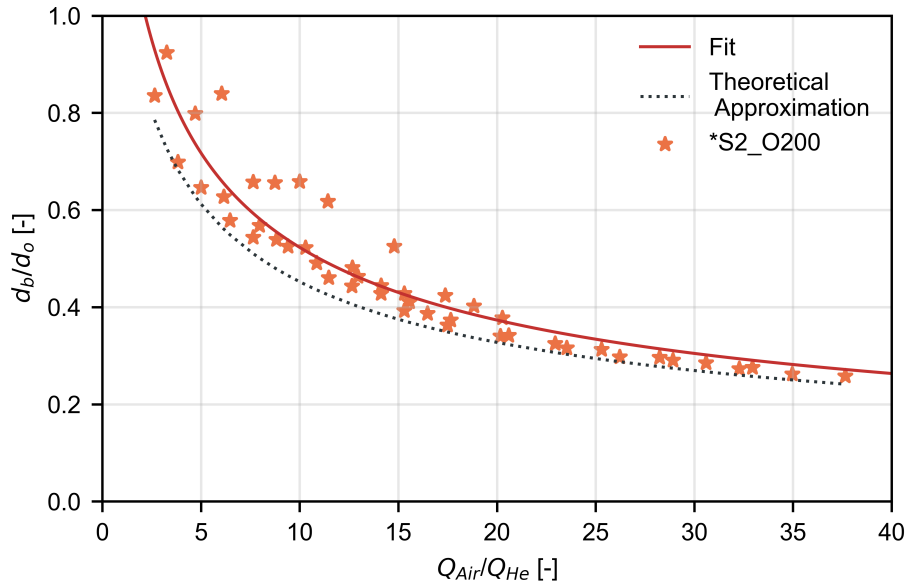


Figure 5.10: Normalized HFSB diameter variation as a function of Q_{Air}/Q_{He} for the *S2_O200 nozzle, including approximated and fitted trend.

The relationship in Equation (5.8) theoretically holds for all nozzles. However, only the data for the S1_O100, S1_O125, S15_O150, S15_O200 and *S2_O200 nozzles, which collapse into a single curve, follow the theoretical approximation as shown in Figure 5.11. It is hypothesized that the parameters involved in the approximation do not fully describe the complex phenomena involved in this multi-phase flow system. The only geometrical dependent variable in the current theoretical approximation is the orifice diameter. Other geometrical aspects of the nozzle such as the scale are not taken into account. It can be seen that for the S1 and S15 series, the lowest contraction ratio nozzles S1_O150 and S15_O250 feature larger particle diameters for similar flow rate ratios. The theoretical approximation behaves as a lower bound for the possible range of particle sizes. For the S1_O075 nozzle which features a high contraction ratio, data is located below this approximation. This is likely to be the case for the S15_O100 nozzle as well, but it is hard to draw conclusions based on the limited operational conditions of this nozzle.

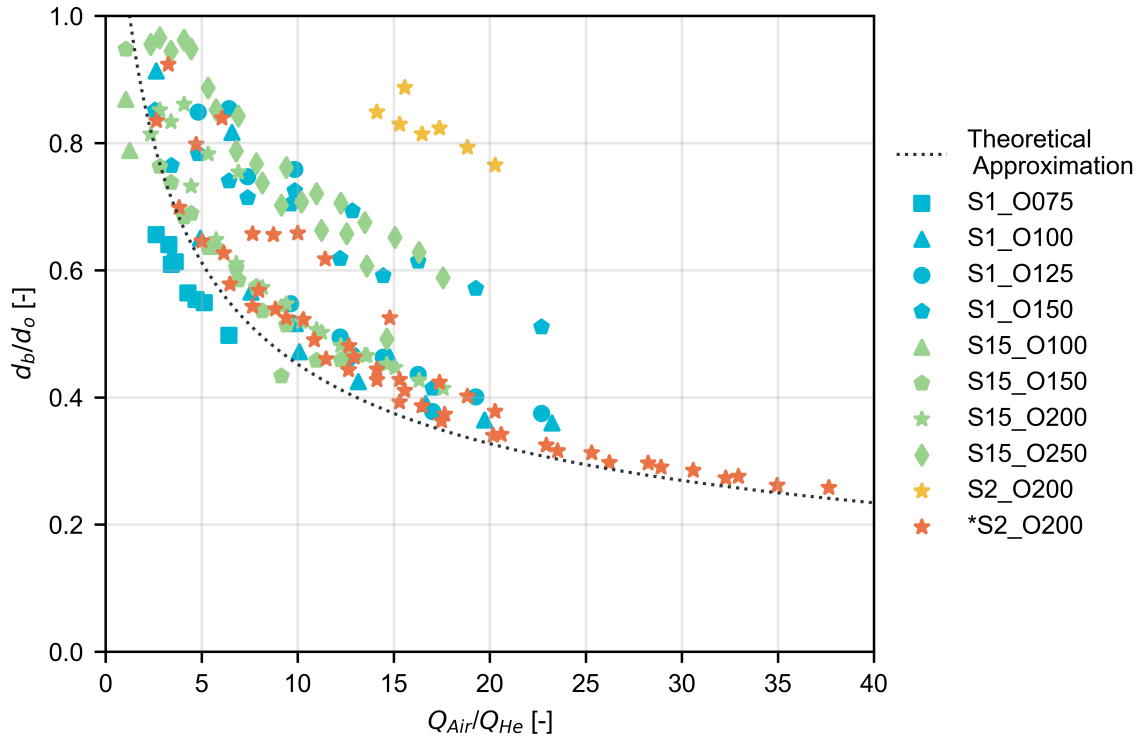


Figure 5.11: Normalized HFBS diameter variation as a function of Q_{Air}/Q_{He} including theoretical approximation.

The particle diameter is bounded by the size of the orifice as the limit $(d_b/d_o)_{max} = 1.0$ is never exceeded. The minimum particle diameter is derived for $Q_{Air}/Q_{He} = 40$, when the variation of the particle diameter beyond this flow rate ratio is minimal ($\Delta y/\Delta x \approx 0.003$). Using

$$\frac{d_b}{d_o} \approx \frac{3}{2} \sqrt{\frac{x}{x+1}}, \text{ where} \quad (5.9)$$

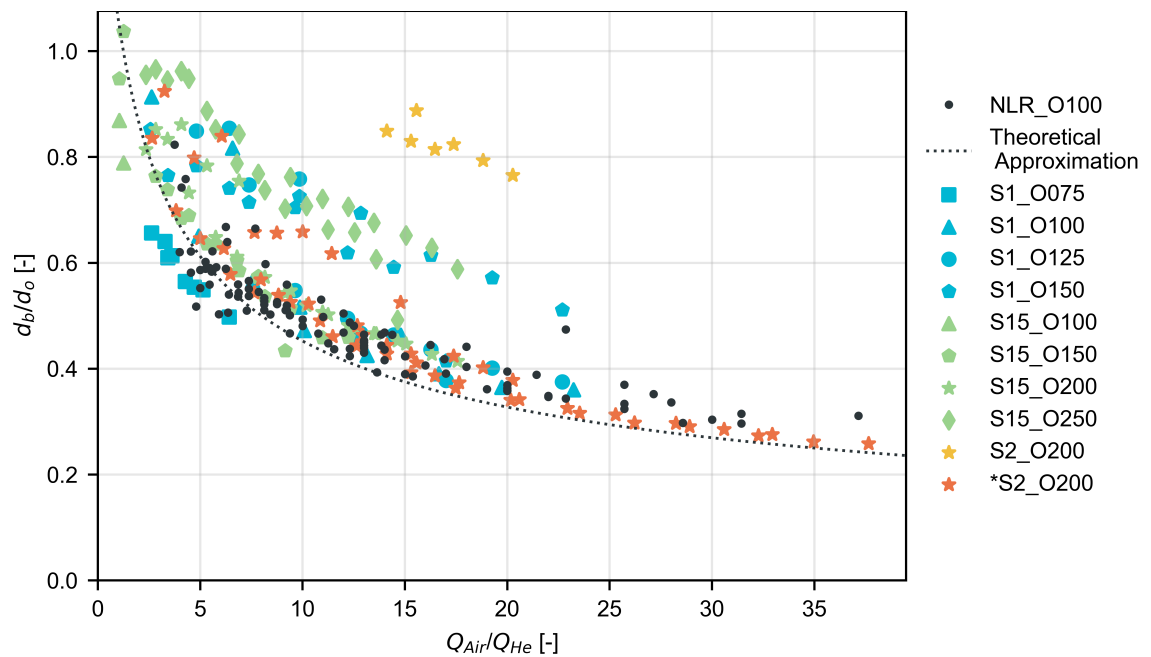
$$x = \frac{Q_{He}}{Q_{Air}}, \quad (5.10)$$

it is found that $(d_b/d_o)_{min} = 0.26$. The results for both minimum and maximum particle diameters per nozzle orifice are shown in Table 5.1. These results are for an ideally operating nozzle. This means that independent of the operating conditions, the nozzle is always in the bubbling regime. It is expected that these results form the lower and upper limits of the possible particle sizes per nozzle orifice diameter.

Closing this section, a brief validation with data from the study by [Faleiros et al. \(2019\)](#) is performed. Data of the *NLR* nozzle with $d_o = 1.0$ mm is incorporated in Figure 5.12. This particular nozzle is schematically shown in Figure 3.6 (*left*). Data stretches almost as far as the *S2_O200 nozzle in terms of the flow rate ratio as a result of the number of operating conditions that were tested. The theoretical approximation is in good agreement with the data. At relatively low Q_{Air}/Q_{He} however, the particle diameter is approximately 15% smaller than estimated.

Table 5.1: Theoretical minimum and maximum particle diameter for an ideally operating nozzle.

Orifice diameter [mm]	$d_{b,\min}$ [mm]	$d_{b,\max}$ [mm]
0.75	0.20	0.75
1.0	0.26	1.0
1.25	0.33	1.25
1.50	0.40	1.50
2.0	0.53	2.0
2.5	0.66	2.5
3.0	0.79	3.0

Figure 5.12: Normalized HFSB diameter variation as a function of $Q_{\text{Air}}/Q_{\text{He}}$ including theoretical approximation and data from the study by Faleiros et al. (2019) for the NLR type nozzle, shown in Figure 3.6 (left).

5.3. Bubble Diameter Dispersion

For each operating point, data on the bubble diameter is filtered and fitted with a Gaussian distribution as described in Chapter 4. For each Gaussian curve, the mean and standard deviation is used to derive the coefficient of variation of the bubble diameter. This variable has been established in the study by Faleiros et al. (2019) to quantify dispersion and distinguish between the jetting and bubbling regimes. In Figure 5.13, the data on the dispersion for all operating points is shown. The thresholds for bubbling and jetting according to Faleiros et al. (2019) are included as a reference, which are 5% and 13%, respectively. It is observed that, as the air flow rate increases, the dispersion increases as well. Comparing the *S1* and *S15* series, it can be seen that CV_d remains well below 10% for the *S1* series. For the *S15* series, however, the increased flow rates cause the relative dispersion to become larger.

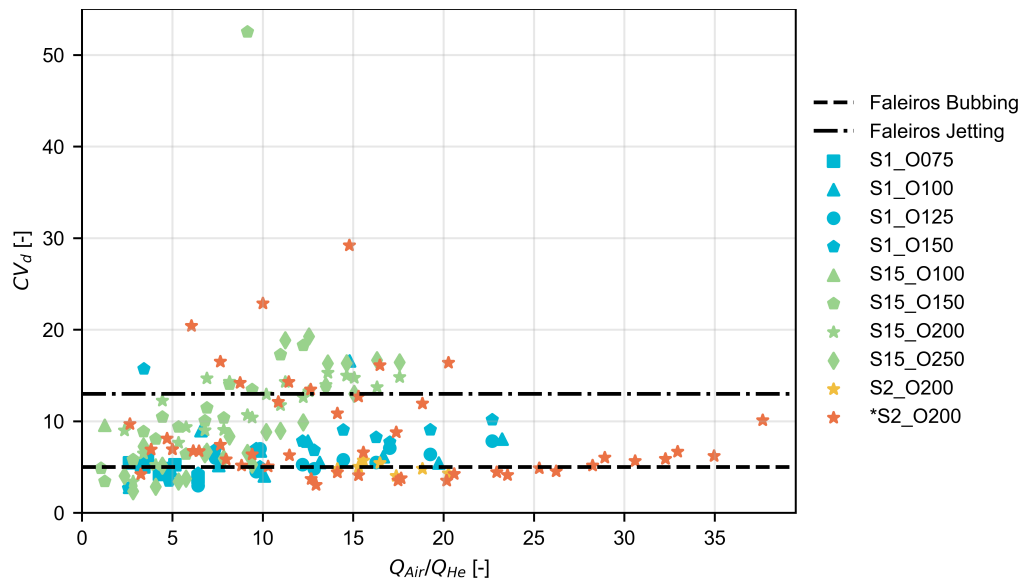


Figure 5.13: HFSB diameter disparity expressed as CV_d as a function of Q_{Air}/Q_{He} for all tested nozzles, including the bubbling and jetting thresholds identified by Faleiros et al. (2019).

5.4. Detailed Nozzle Performance

The key findings of the previous sections can be summarized into a single figure for each nozzle. The production regime plots from Section 5.1 include information regarding the regime (bubbling/jetting) and the minimum and maximum bubble diameter, while in the bubbling regime for each particular neutrally buoyant condition is given. The threshold for jetting is derived from the data observed by Faleiros et al. (2019), which is $CV_d = 13\%$. Finally, to quantify the bubble scalability of an individual nozzle, the scalability ratio of maximum to minimum bubble diameter ($d_{b,max} / d_{b,min}$) for all tested conditions is used, which is presented at the end of this section. Data on the nozzle performance for series S3 nozzle has been omitted since this nozzle does not have a single working operating point.

Variations in the flow rate of helium are expected to influence the bubble size, which is described in Section 5.2. Contrary to expectations, a higher flow rate of helium does not necessarily result in larger bubbles at identical values of Q_{Air} . This can be seen in several of the following figures, including Figure 5.14. For the tested conditions of the S1 series nozzles, jetting occurs infrequently as the nozzles cease to produce any bubbles at higher flow rates of air. The best performing S1 nozzle in terms of the scalability ratio is the S1_O125 nozzle with $d_{b,max} / d_{b,min} = 2.3$.

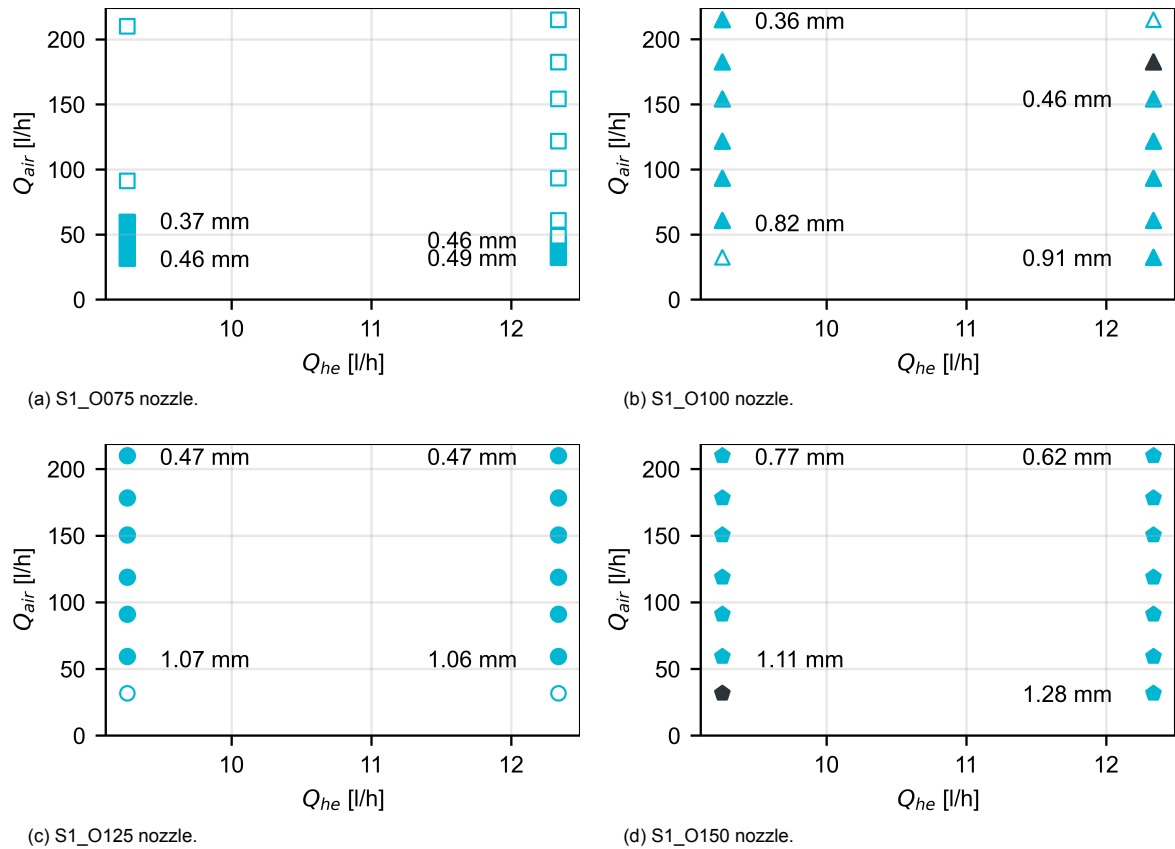


Figure 5.14: Detailed nozzle performance for series *S1* nozzles, whereby filled and empty markers indicate working and non-working conditions, and gray markers indicate jetting. Largest and smallest mean bubble diameter for bubbling regimes is indicated.

Increasing the size of the nozzle by 1.5 times and thus increasing the supply rates by 1.5^2 leads more often to jetting for higher flow rates, as can be seen from Figure 5.15. Again, higher flow rates of helium do not necessarily result in bigger bubbles. Both the S15_O150 and S15_O200 nozzles have a scalability ratio of 1.8. For the nozzle with the largest orifice, S15_O250, bubbles of 2.41 mm in diameter are produced at $(Q_{\text{Air}}, Q_{\text{He}}, Q_{\text{BSF}}) = (89.9 \text{ l/h}, 22.0 \text{ l/h}, 20.0 \text{ ml/h})$. Another point of interest is the air flow rate for the largest measurable diameter in Figure 5.15c. It can be seen that the largest diameter is only measured for the second bubbling operating point.

For the pure geometrically scaled nozzle in Figure 5.16a, jetting does not occur. However, for three-quarters of the tested conditions the nozzle does not produce bubbles at all. The size range of bubbles is therefore low, and it is advised to use alternatives such as the S15_O200 and S15_O250 nozzle. These have a much larger operating range and produce similar sized bubbles. For the nozzle with updated internals in Figure 5.16b, the range is much broader. For all tested conditions, $d_{b,\text{max}} / d_{b,\text{min}} = 3.6$. The average bubble diameter is 0.52 mm for the operational point at the lowest helium and highest air flow rate. Similar sized bubbles are produced by the *S1* series nozzles. However, for lower air flow rates, the bubble size can be increased up to 1.85 mm on average. It must be noted that the relative performance of the *S2_O200 nozzle to other nozzles should not be overestimated, since four neutrally buoyant conditions were tested instead of two.

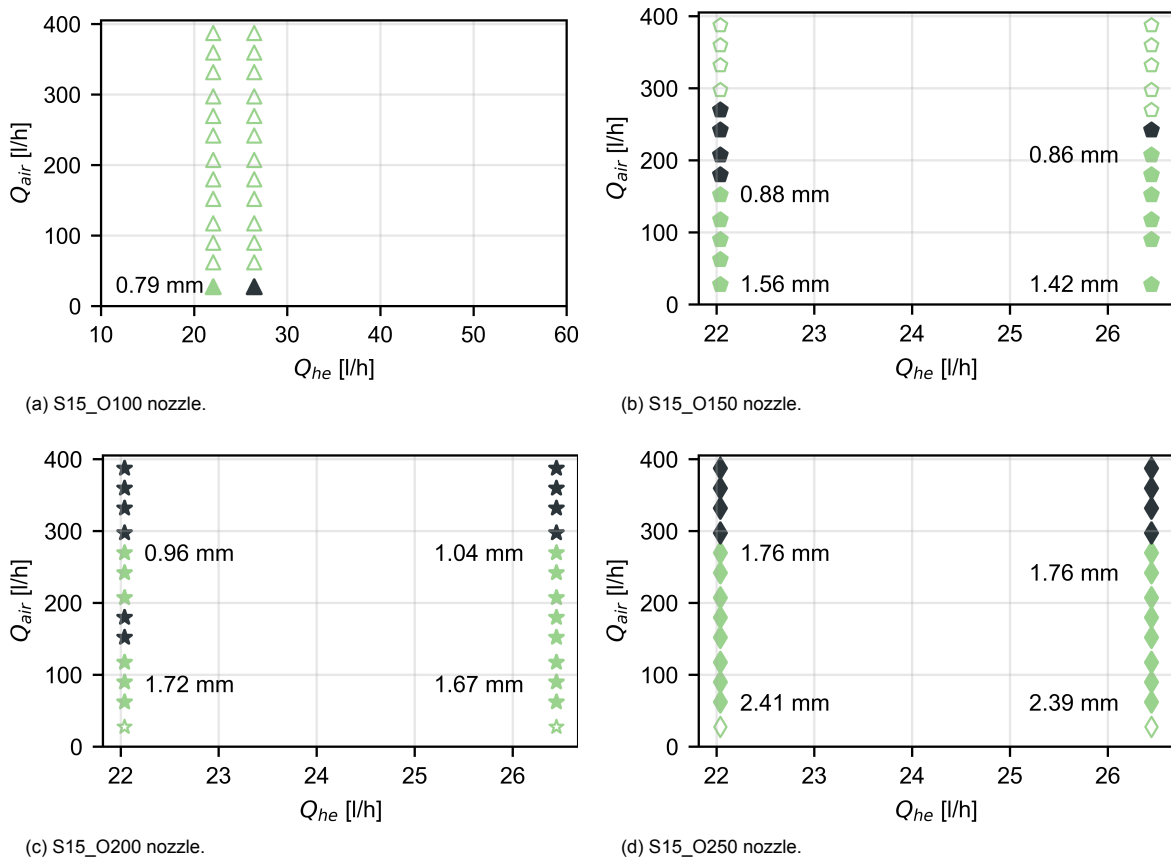


Figure 5.15: Detailed nozzle performance for series S15 nozzles, whereby filled and empty markers indicate working and non-working conditions, and gray markers indicate jetting. Largest and smallest mean bubble diameter for bubbling regimes is indicated.

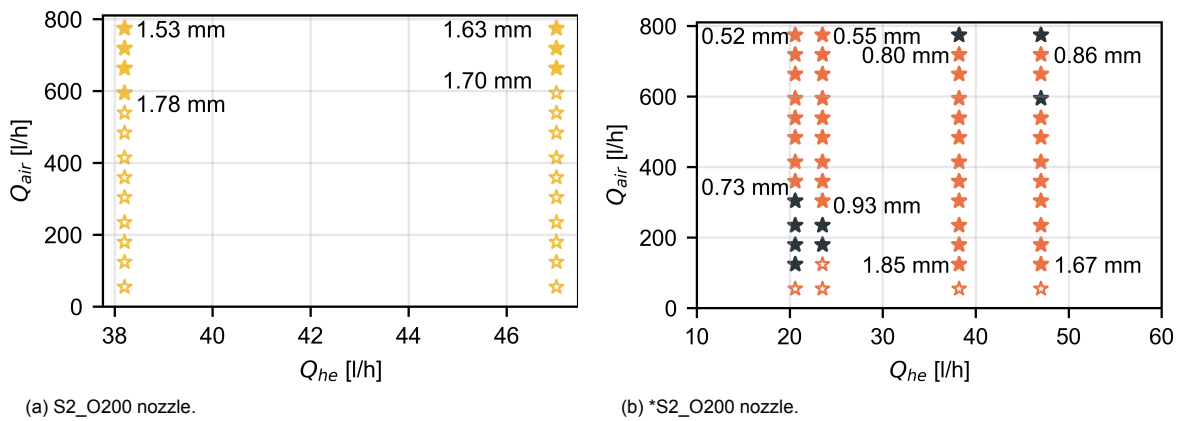


Figure 5.16: Detailed nozzle performance for series S2 nozzles, whereby filled and empty markers indicate working and non-working conditions, and gray markers indicate jetting. Largest and smallest mean bubble diameter for bubbling regimes is indicated.

The ratios of largest to smallest mean bubble diameter can be found in Table 5.2. In comparison to the theoretical model in Table 5.1, the prediction minimum particle diameter only matches with the experimental data for the *S2_O200 nozzle. For the other nozzles, the minimum particle diameters are between 25-200% larger than estimated. The maximum theoretical particle diameter is only exceeded for the S15_O150 nozzle by 4%. The bubbles produced by other nozzles except S1_O075 are between 4-20% smaller than estimated. For the latter, actual particle diameters are 50% smaller than anticipated using the approximation outlined in Section 5.2.

In summary, the smallest bubbles, 0.36 mm in diameter, are produced by the S1_O100 nozzle at $(Q_{\text{Air}}, Q_{\text{He}}, Q_{\text{BSF}}) = (215.0 \text{ l/h}, 9.3 \text{ l/h}, 8.9 \text{ ml/h})$. The largest average bubbles of 2.41 mm are produced by the S15_O250 nozzle at $(Q_{\text{Air}}, Q_{\text{He}}, Q_{\text{BSF}}) = (89.9 \text{ l/h}, 22.0 \text{ l/h}, 20.0 \text{ ml/h})$. Using the theoretical approximation outlined in Section 3.9, it translates to a measurement volume of approximately $2.5 \times 10^5 \text{ cm}^3$, which is equivalent to domains larger than the human body itself.

Table 5.2: Minimum and maximum bubble diameter per nozzle for $CV_d < 13\%$.

Nozzle	$d_{b,\text{min}}$ [mm]	$d_{b,\text{max}}$ [mm]	$d_{b,\text{max}} / d_{b,\text{min}}$
S1_O075	0.37	0.49	1.3
S1_O100	0.36	0.91	2.5
S1_O125	0.47	1.07	2.3
S1_O150	0.77	1.28	2.1
S15_O100	0.79	-	-
S15_O150	0.86	1.56	1.8
S15_O200	0.96	1.72	1.8
S15_O250	1.76	2.41	1.4
S2_O200	1.53	1.78	1.2
*S2_O200 (T19-T20)	0.52	0.93	2.3
*S2_O200 (T21-T22)	0.80	1.85	1.8
*S2_O200	0.52	1.85	3.6
S3_O300	-	-	-

5.5. Production Frequency

Although larger particles lift some of the restrictions of PIV systems with conventional HFSB generators, it is important to keep other key variables such as the production frequency in mind. Section 2.4 describes that the spatial resolution for a given experimental set-up can be increased by the number of bubbles per second introduced into the measurement domain. Both the number of nozzles and the production frequency of each nozzle can be used to reach the desired tracer concentration. To gain insight to the production frequency of the geometrically scaled nozzles, several double frame recordings are made for tests *Txx.2*, *Txx.5* and *Txx.13*. The jet velocity is derived with DaVis 10.1. software from LaVision, using PTV as introduced in Section 2.2. The production frequency is subsequently derived from the relations as defined in Section 4.9.

The volume occupied by the bubble V_b , based on its diameter, can be compared to the flow rate of helium used and the production frequency via

$$d_b = \left(\frac{6}{\pi} V_b \right)^{1/3}, \text{ where} \quad (5.11)$$

$$V_b = \frac{Q_{\text{He}}}{f}. \quad (5.12)$$

With these relations it can be derived that $f \propto d_b^{-3}$.

The relationship $V_b = f/Q_{\text{He}}$ is shown in Figure 5.17 together with the experimental data. When the linear relationship is maintained, the volume occupied by the bubble agrees with the used amount of helium and corresponding production frequency. However, deviations above this line indicate that $V_b > f/Q_{\text{He}}$, while below means the opposite. Both deviations could be a result of incorrect pressure to flow rate conversions. However, it is expected that calibration errors introduce biases for all data-points, which also be more pronounced at lower flow rates. Analysing the bubble diameter histograms for the nozzles showing large deviations did not provide a reason for these offsets. The deviations of the S1_O075 and *S2_O200 nozzles, whereby $V_b < f/Q_{\text{He}}$, have been reported by [Faleiros et al. \(2019\)](#), [Gibeau et al. \(2020\)](#) to be likely to occur. It is caused by the leakage of helium during the bubble formation process, overestimating the amount of helium captured by the bubble.

Figure 5.18 shows the production frequency as a function of the bubble diameter. Given the low amount of data-points, some caution is necessary for the analysis of the observed trends. It includes the proportionality trend between the variables f and d_b for $Q_{\text{He}} = 9.3$ l/h for the S1 series and $Q_{\text{He}} = 22$ l/h for the S15 series nozzles.

The data can be validated with data from the study by [Faleiros et al. \(2019\)](#), whereby a similar nozzle (*NLR* type, Figure 3.6) with $d_o = 1$ mm operated at $f = 20$ kHz at similar operating conditions of Q_{Air} , Q_{He} and Q_{BSF} . This is twice the production frequency of the S1_O100 nozzle, but the same order of magnitude. The *DLR* type nozzle, however, is reported to operate at 8 kHz, which is slightly lower than the measured production rate for the similarly sized nozzle.

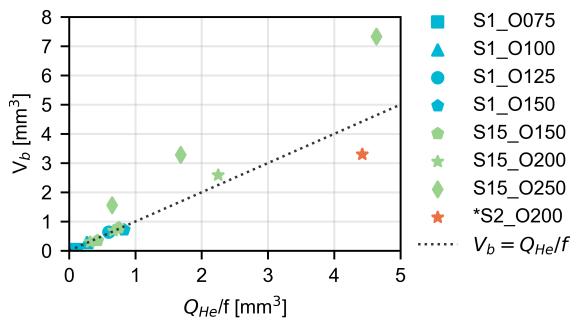


Figure 5.17: Bubble volume dependency on the production rate.

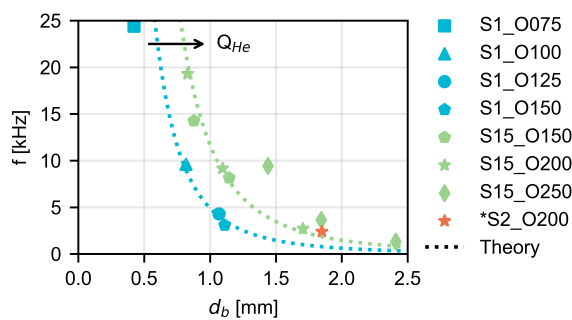


Figure 5.18: Variation of the production frequency with bubble diameter, including a trendline following Equations 5.11 and 5.12 and an arrow indicating the increase of helium.

6

Conclusion & Recommendations

In this research project, an attempt has been made to identify and characterise the main scaling parameters in the production of helium-filled soap bubbles used in Particle Image Velocimetry. In this chapter, the conclusions based on the performed work are presented and recommendations are made for future research.

6.1. Conclusion

A literature survey shows there is a growing demand to analyse flow fields of volumes larger than the human body itself. The experimental technique called Particle Image Velocimetry has already evolved during the last decade to cope with the diminishing light scattering intensity to analyse flow fields on large domains. However, proposed solutions such as increasing the laser intensity or using traversing or robotic systems are costly. The latter method also suffers from the need to time-average the velocity field, only providing insight into the statistics of the mean flow. Limitations have been partially addressed by the introduction of helium-filled soap bubbles for quantitative measurements, which are several orders of magnitudes larger than conventional tracer particles (Scarano et al. 2015). Following the ray-tracing model presented by Caridi (2018), the quadratic relation between the scattered light and the particle diameter is confirmed. This is the fundamental reason for scaling particles and increasing the size of the domain. Application of the relationships established by Caridi (2018) enables a mathematical coupling between particle diameter and measurement domain. Compared to recently performed 3D-3C time-resolved measurements, a 25 fold increase in the maximum attainable measurement domain can be achieved by scaling current HFSB to 2.5 mm. This highlights that scaling HFSB is a viable solution for the application of PIV to large-scale, industrial measurements. Analysing the formation, evolution and motion of fluid structures and their complex interactions as a function of time on domains of several cubic metres would be extremely valuable for aerodynamicists, while the industry could also benefit from faster turnaround times and reduced operating costs in wind tunnel facilities.

In the experimental campaign that followed, recordings are made of the individual glare points originating from a single bubble to analyse the particle diameter for various operating conditions. Here, the theoretical neutrally buoyant condition is maintained by controlling the supply of helium and soap. This condition must be preserved to ensure that HFSB approach ideal flow tracing behaviour. Various geometrical changes to the design of the nozzle developed by Delft University of Technology were analysed. A geometrical scaling factor increasing the size in all three dimensions was applied in combination with changes to the diameter of the orifice. Changes to the internal geometry for nozzles with a scaling factor higher than two results in significant improvements in terms of the ability to produce bubbles over a large range of input variables. This is a crucial design aspect for scaled nozzles, which prevents the formation of excess soap within the nozzle, causing a blockage and obstructing the

production of bubbles.

As opposed to currently available data-driven predictions, a novel, physics-based model predicting the bubble diameter is presented. The non-dimensional proportionality $d_b/d_o \propto \sqrt{Q_{\text{He}}/(Q_{\text{Air}} + Q_{\text{He}})}$ that has been found is in good agreement with the experimental data over a wide range of operational conditions. Furthermore, the theoretical approximation provides upper and lower bounds of $(d_b/d_o)_{\text{max}} = 1$ and $(d_b/d_o)_{\text{min}} = 0.26$ for an ideally operating nozzle. The relationships found in this research project can be used to size HFSB according to a particular experimental arrangement, supporting the design of large-scale, time-resolved volumetric measurements using PIV and the nozzle generator design by Delft University of Technology.

Bubbles with a diameter up to 2.5 mm are produced, which is five times larger than the bubbles produced by conventional HFSB generators used by Delft University of Technology. A theoretical analysis of the attainable measurement domain shows that this corresponds to an increase of a factor 3 in every dimension compared to recently conducted HFSB experiments, enabling the analysis of volumes of approximately $2.5 \times 10^5 \text{ cm}^3$.

Returning to the research objective of this project, which read:

To increase the ratio of largest to smallest particle diameter of neutrally buoyant HFSB by analysing the experimental results of varying geometrical and operational parameters of a 3D printed nozzle developed by Delft University of Technology.

This objective is successfully accomplished in the research project. Conventional HFSB nozzle generators developed by Delft University of Technology produce particles with scalability ratio $d_{b,\text{max}}/d_{b,\text{min}}$ of 2.5. The most versatile nozzle in terms of the scalability ratio in the current work is capable of producing bubbles up to 3.6 times larger than the smallest bubbles from the same nozzle, by varying the neutrally buoyant condition and the flow rate of air. This nozzle can therefore meet a variety of requirements for the light scattering intensity of different optical arrangements.

6.2. Recommendations

The research has shown the potential and flexibility of nozzle generators to scale HFSB beyond the conventional size. However, various improvements in both the research method itself and the design of the nozzles can be made, leading to more reliable nozzles and better repeatability of the experiments. Recommendations will be given regarding the research framework and chosen processes and propositions are made for subsequent research on the scalability of HFSB and the design of nozzle generators.

In the nozzle design phase, 8 additional nozzles were manufactured with varying orifices and updated internals. However, after the 3D printing process was finished, nozzles were not cleaned thoroughly to prevent printing resin to harden. This resulted in the blockage of the internal channels, making it impossible to test them. Thus, it is advised to thoroughly flush the nozzles and clean any remaining 3D-print resin to minimise production deficiencies. The ongoing COVID pandemic prevented reprinting nozzles within the time-frame of this project. This is unfortunate since the framework and analysis presented in this work could have been used to describe the behaviour of more nozzles which could ultimately further emphasize the validity of the proposed models. Nevertheless, the presented work is a basis for future research and presents a novel physics-based model for the prediction of HFSB sizes.

The current research uses calibration curves to relate the pressure set on the Fluid Supply Unit to flow rates. This had several consequences. First of all, as new gauges became available, the operating range per nozzle could be expanded. For this, no additional calibration curves were constructed, but the current ones are extrapolated to convert pressure to volumetric flow rates. Turbulence and compressibility effects at these higher flow rates may cause deviations from the assumed linear proportionality at higher flow rates. Secondly, with the new gauges, several nozzles still operated nominally at the limits

of the operational range of the gauges on the FSU. Using pressure gauges with a higher maximum pressure would allow for mapping of the operational limits of the nozzles. Thirdly, the use of analogue pressure gauges introduces observational errors over the full pressure range and instrumental errors at the lowest pressure settings. These cumulatively contribute to an error of approximately 10%, as described in Section 4.10. Therefore, it is advised to switch to digital mass flow meters and control valves to avoid the need for curves relating pressure to flow rates.

During the experimental phase, nozzles are orientated in the vertical direction to minimise excess soap blocking the nozzle. For wind tunnel experiments, this orientation is not suitable for the use in a rake with multiple nozzles. It will lead to blockage and an uneven spatial distribution of the bubbles, as they are produced in each others wake. It is hypothesised that optimising the internal soap channels for each nozzle scale could solve this challenge.

After filtering, cropping and normalising the raw image data, intensity peaks are located using a peak finding algorithm. Here, the initial peak filtering takes place by selecting the minimal allowed distance separating intensity peaks. This distance is currently a constant value for all nozzles and operating conditions. However, the initial peak filtering procedure can be made more robust by integrating an adaptive threshold related to the mean bubble diameter for the minimal peak separation. The subsequent peak sorting by means of the bounding box, as indicated in Section 4.6, can also be improved by means of adaptive thresholds. The dimensions of the bounding box remain constant, while the bubble diameter varies significantly between 0.4 and 2.5 mm. By iteratively updating the thresholds with a value based on the mean bubble diameter, more peaks can be found. This enhances the accuracy of the results, since the number of bubbles detected for some measurements are as low as 300.

Measurements on the particle size for various nozzles have shown that the S15_O250 nozzle is capable of producing bubbles with a diameter of 2.41 mm. This is 2.5 times larger than the tracers produced with the baseline nozzle currently used by TU Delft. However, the reason for producing bigger bubbles is the increase of the measurement domain due to an increase in the scattered light. The current research uses literature and a theoretical model to confirm this, but an experimental validation would amount to a more comprehensive study where reason, method and result are covered as a whole. The scattered light is not included in the current study, since a light source with varying pulse amplitude was used. This prevented the comparison of the scattering intensity between different test cases. This also introduced challenges in the set-up of the laser to maintain a high signal-to-noise ratio without saturating image pixels. The image data however, shows that pixel saturation is also occurring for larger particle sizes. The saturation of pixels, as noted in Section 4.10, introduces additional uncertainties in the results. It is therefore advised to ensure that the equipment, in particular the illumination source, is able to operate with minimal amplitude variations between pulses.

The most promising nozzles in terms of largest particle diameter and particle ratio should be subject to more detailed investigations. It is particularly useful to analyse the particle response time and be able to draw conclusions on the neutral buoyancy of the HFSB. For this, a standardized experiment is advised so that HFSB of different nozzles can be compared accurately and reliably. The experiment outlined in the study by [Scarano et al. \(2015\)](#) is a good starting point.

The trends of Figure 5.8, relating d_b/d_o to $Q_{\text{Air}}/Q_{\text{He}}$, which do not collapse must be subject to further investigation. As yet, no exact reason could be found explaining this behaviour. It is hypothesised however, that more geometrical parameters must be included to completely understand the phenomena involved. It is thought that the contraction ratio could play a role here, which affects the relative positioning between internal helium and soap exits and the nozzle orifice. Testing more nozzles, with identical orifice size but varying scale, could provide definitive answers regarding the influence of the contraction ratio.

While the current research focused on the geometrical scale and orifice size of the HFSB nozzle generator, other design considerations are worth investigating. A suggestion is to analyse the shape and length of the orifice as well. The shape of the inner-edge side of the orifice, influences the streamline pattern within the orifice, as seen in Figure 6.1. This may have a significant effect on the production of HFSB in terms of size and production frequency. Additionally, varying orifice length may cause similar

effects. For a viscous flow within a pipe, the velocity profile transforms from constant to parabolic due to friction effects occurring near the walls. This could cause the helium streamtube, located in the 'core' of the orifice, to travel at higher speeds. As a result, it might be possible to attain higher production frequencies since this is mainly a function of the jet velocity (Faleiros et al. 2019). Shear between the different gases within the orifice could also enhance instabilities, which is the main mechanism behind the bubble formation process as presented in Section 3.2.

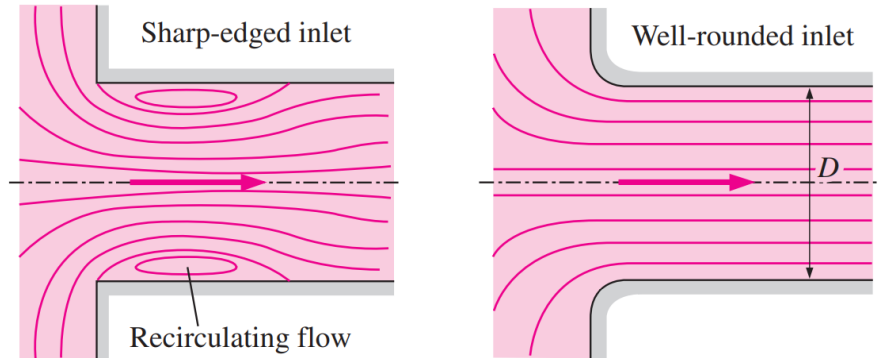
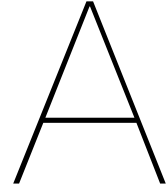


Figure 6.1: Streamlines for sharp-edged and rounded orifices. Adapted from Cengel et al. (2016).



Test matrices

Table A.1: Test Matrix for P_{BSF} and P_{He} for nozzles with a scaling factor of 1.5, 2 and 3 and varying orifice sizes.

Nozzle	Test no.	P_{BSF} [bar]	P_{He} [bar]
S1_O075	T1	1.6	0.9
	T2	2.0	1.2
S1_O100	T3	1.6	0.9
	T4	2.0	1.2
S1_O125	T5	1.6	0.9
	T6	2.0	1.2
S1_O150	T7	1.6	0.9
	T8	2.0	1.2
S15_O100	T9	2.3	1.5
	T10	2.8	1.8
S15_O150	T11	2.3	1.5
	T12	2.8	1.8
S15_O200	T13	2.3	1.5
	T13	2.8	1.8
S15_O250	T15	2.3	1.5
	T16	2.8	1.8
S2_O200	T17	2.0	1.3
	T18	2.5	1.6
*S2_O200	T19	1.0	0.7
	T20	1.2	0.8
*S2_O200	T21	2.0	1.3
	T22	2.5	1.6
S3_O300	T23	2.3	3.0
	T24	2.8	3.7

Table A.2: Conversion matrix Q_{Air} to P_{Air} per geometrical scaling factor.

Test number	Tx.0	Tx.1	Tx.2	Tx.3	Tx.4	Tx.5	Tx.6	Tx.7	Tx.8	Tx.9	Tx.10	Tx.11	Tx.12	Tx.13
Q_{Air} [l/h]	0	30	60	90	120	150	180	210	240	270	300	330	360	390
P_{Air} for S1 [bar]	0	0.8	1.5	2.3	3	3.8	4.5	5.3						
P_{Air} for S15 [bar]	0	0.4	0.9	1.3	1.7	2.2	2.6	3	3.5	3.9	4.3	4.8	5.2	5.6
Q_{Air} [l/h]	0	60	120	180	240	300	360	420	480	540	600	660	720	780
P_{Air} for S2 [bar]	0	0.4	0.9	1.3	1.7	2.2	2.6	3	3.5	3.9	4.3	4.8	5.2	5.6
Q_{Air} [l/h]	0	180	360	540	720	900	1080	1260	1440	1620				
P_{Air} for S3 [bar]	0	0.7	1.3	2	2.6	3.3	3.9	4.6	5.2	5.9				

B

Code Flowchart

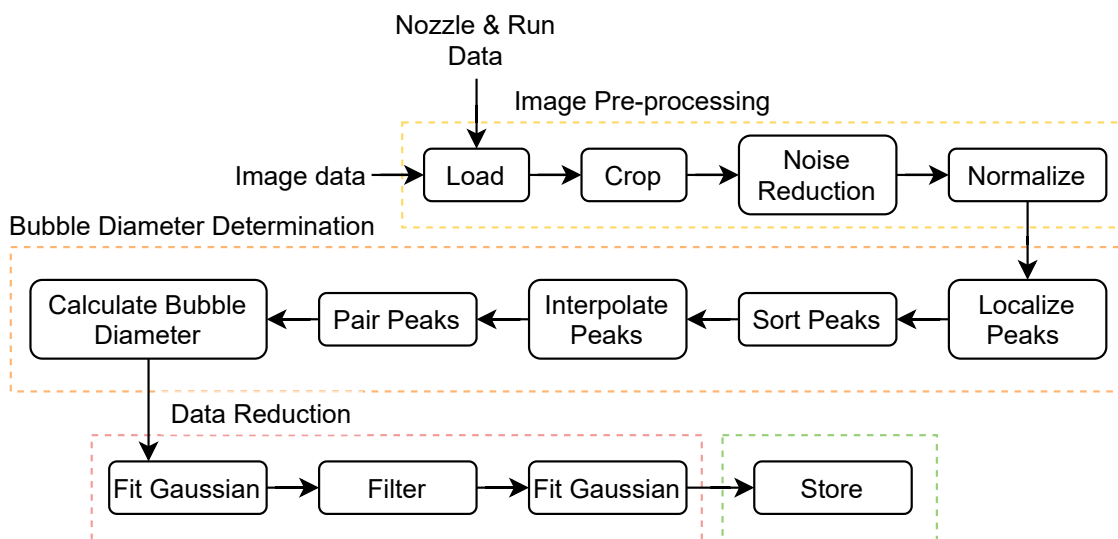


Figure B.1: Code Flowchart.

Bibliography

- Adrian, R. J. Dynamic ranges of velocity and spatial resolution of particle image velocimetry. *Measurement Science and Technology*, 8(12):1393–1398, 1997. ISSN 09570233. DOI: 10.1088/0957-0233/8/12/003.
- Adrian, R. J. Statistical properties of particle image velocimetry measurements in turbulent flow. *Proceedings of Laser Anemometry in Fluid Mechanics III*, 1986.
- Adrian, R. J. Particle-Imaging Techniques for Experimental Fluid Mechanics. *Annual Review of Fluid Mechanics*, 23:261–304, 1991. ISSN 0066-4189. DOI: 10.1146/annurev.fl.23.010191.001401.
- Adrian, R. J. and Westerweel, J. *Particle image velocimetry*. Number 30. Cambridge university press, 2011.
- Adrian, R. J. and Yao, C.-S. Pulsed laser technique application to liquid and gaseous flows and the scattering power of seed materials. *Applied Optics*, 24(1):44–52, 1985. ISSN 0003-6935. DOI: 10.1364/ao.24.000044.
- Ambravaneswaran, B., Subramani, H. J., Phillips, S. D., and Basaran, O. A. Dripping-jetting transitions in a dripping faucet. *Physical Review Letters*, 93(3):3–6, 2004. ISSN 00319007. DOI: 10.1103/PhysRevLett.93.034501.
- Bakar, H. A., Abas, A., Mokhtar, N. H., Razak, N., and Abdul, M. N. B. Particle Image Velocimetry and Finite Volume Method Study of Bi-leaflet Artificial Heart Valve. *Journal of Applied Fluid Mechanics*, 11(5):1365–1375, 2018. DOI: 10.29252/jafm.11.05.
- Berg, J. V. D., Jux, C., and Sciacchitano, A. Robotic Volumetric PIV measurements of a full-scale swimmer 's hand. In *13th International Symposium on Particle Image Velocimetry – ISPIV 2019*, 2019. DOI: 10.18726/2019.
- Biwole, P. H. *Large Scale Particle Tracking Velocimetry for 3-Dimensional Indoor Airflow Study*. PhD thesis, National Institute of Applied Sciences of Lyon, 2009.
- Bomphrey, R. J., Henningson, P., Michaelis, D., and Hollis, D. Tomographic particle image velocimetry of desert locust wakes: Instantaneous volumes combine to reveal hidden vortex elements and rapid wake deformation. *Journal of the Royal Society Interface*, 9:3378–3386, 2012. ISSN 17425662. DOI: 10.1098/rsif.2012.0418.
- Bosbach, J., Kühn, M., and Wagner, C. Large scale particle image velocimetry with helium filled soap bubbles. *Experiments in Fluids*, 46:539–547, 2009. ISSN 07234864. DOI: 10.1007/s00348-008-0579-0.
- Brownstein, I. D., Wei, N. J., and Dabiri, J. O. Aerodynamically Interacting Vertical-Axis Wind Turbines: Performance Enhancement and Three-Dimensional Flow. *Energies*, 12:2724, 2019. ISSN 1996-1073. DOI: 10.3390/en12142724.
- Caridi, G. C. A. *Development and application of helium-filled soap bubbles For large-scale PIV experiments in aerodynamics*. PhD thesis, Delft University of Technology, 2018.
- Caridi, G. C. A., Ragni, D., Sciacchitano, A., and Scarano, F. A seeding system for large-scale Tomographic PIV in aerodynamics. In Adrian, R. J., editor, *11th International symposium on particle image velocimetry , PIV15*, page 2015, 2015.

- Caridi, G. C. A., Ragni, D., Sciacchitano, A., and Scarano, F. HFSSB-seeding for large-scale tomographic PIV in wind tunnels. *Experiments in Fluids*, 57:190, 2016. ISSN 07234864. DOI: 10.1007/s00348-016-2277-7.
- Caridi, G. C. A., Sciacchitano, A., and Scarano, F. Helium-filled soap bubbles for vortex core velocimetry. *Experiments in Fluids*, 58:130, 2017. ISSN 07234864. DOI: 10.1007/s00348-017-2415-x.
- Cengel, Y., Turner, R., and Cimbala, J. *Fundamentals of Thermal-Fluid Sciences*. McGraw-Hill Education, 5 edition, 2016. ISBN 978-0078027680.
- Clanet, C. and Lasheras, J. C. Transition from dripping to jetting. *Journal of Fluid Mechanics*, 383: 307–326, 1999. ISSN 00221120. DOI: 10.1017/S0022112098004066.
- Czyż, Z., Karpiński, P., and Stryczniewicz, W. Measurement of the flow field generated by multicopter propellers. *Sensors*, 20(19):1–22, 2020. ISSN 14248220. DOI: 10.3390/s20195537.
- Elger, D. F., LeBret, B. A., Crowe, C. T., and Roberson, J. A. *Engineering Fluid Mechanics*. John Wiley & Sons, 2019.
- Elsinga, G. E., Oudheusden, van, B. W., and Scarano, F. Experimental assessment of Tomographic-PIV accuracy. In *13th Int Symp on Applications of Laser Techniques to Fluid Mechanics*, 2006a.
- Elsinga, G. E., Scarano, F., Wieneke, B., and Oudheusden, van, B. W. Tomographic particle image velocimetry. *Experiments in Fluids*, 41:933–947, 2006b. ISSN 07234864. DOI: 10.1007/s00348-006-0212-z.
- Faleiros, D. E., Tuinstra, M., Sciacchitano, A., and Scarano, F. Helium-filled soap bubbles tracing fidelity in wall-bounded turbulence. *Experiments in Fluids*, 59:56, 2018. ISSN 07234864. DOI: 10.1007/s00348-018-2502-7.
- Faleiros, D. E., Tuinstra, M., Sciacchitano, A., and Scarano, F. Generation and control of helium-filled soap bubbles for PIV. *Experiments in Fluids*, 60:40, 2019. ISSN 07234864. DOI: 10.1007/s00348-019-2687-4.
- Fukuchi, Y. Influence of number of cameras and preprocessing for thick volume Tomographic PIV. In *16th Int. Symp. on Applications of Laser Techniques to Fluid Mechanics*, 2012.
- Ghaemi, S. and Scarano, F. Multi-pass light amplification for tomographic particle image velocimetry applications. *Measurement Science and Technology*, 21, 2010. ISSN 13616501. DOI: 10.1088/0957-0233/21/12/127002.
- Ghaemi, S. and Scarano, F. Counter-hairpin vortices in the turbulent wake of a sharp trailing edge. *Journal of Fluid Mechanics*, 689:317–356, 2011. ISSN 00221120. DOI: 10.1017/jfm.2011.431.
- Gibeau, B. and Ghaemi, S. A modular, 3D-printed helium-filled soap bubble generator for large-scale volumetric flow measurements. *Experiments in Fluids*, 59:178, 2018. ISSN 07234864. DOI: 10.1007/s00348-018-2634-9.
- Gibeau, B., Gingras, D., Raffel, J., Raffel, M., and Ghaemi, S. Effect of internal geometry and orientation on the performance of a helium-filled soap bubble nozzle. *13th International Symposium on Particle Image Velocimetry*, 2019.
- Gibeau, B., Gingras, D., and Ghaemi, S. Evaluation of a full-scale helium-filled soap bubble generator. *Experiments in Fluids*, 61:28, 2020. ISSN 14321114. DOI: 10.1007/s00348-019-2853-8.
- Hale, R. W., Tan, P., Stowell, R., Ordway, D. E., and Incorporated, S. A. Development of an integrated system for flow visualization in air using neutrally-buoyant bubbles. Technical report, Office of Naval Research, Aeronautics, 1971.
- Henningsson, P., Michaelis, D., Nakata, T., Schanz, D., Geisler, R., Schröder, A., and Bompfrey, R. J. The complex aerodynamic footprint of desert locusts revealed by large-volume tomographic particle image velocimetry. *Journal of the Royal Society Interface*, 12, 2015. ISSN 17425662. DOI: 10.1098/rsif.2015.0119.

- Herrero, E., Percin, M., Karasek, M., and Oudheusden, B. V. Flow Visualization around a Flapping-Wing Micro Air Vehicle in Free Flight Using Large-Scale PIV. *aerospace*, 5:99, 2018. DOI: 10.3390/aerospace5040099.
- Huhn, F., Schanz, D., Gesemann, S., Dierksheide, U., van de Meerendonk, R., and Schröder, A. Large-scale volumetric flow measurement in a pure thermal plume by dense tracking of helium-filled soap bubbles. *Experiments in Fluids*, 58(9):116, 2017. ISSN 07234864. DOI: 10.1007/s00348-017-2390-2.
- Hulst van de, H. C. and Wang, R. T. Glare points. *Applied Optics*, 30(33):4755, 1991. ISSN 0003-6935. DOI: 10.1364/ao.30.004755.
- Jux, C. Robotic Volumetric Particle Tracking Velocimetry by Coaxial Imaging and Illumination. Master's thesis, Delft University of Technology, 2017.
- Jux, C., Sciacchitano, A., Schneiders, J. F., and Scarano, F. Robotic volumetric PIV of a full-scale cyclist. *Experiments in Fluids*, 59, 2018. ISSN 07234864. DOI: 10.1007/s00348-018-2524-1.
- Kähler, C. J., Sammler, B., and Kompenhans, J. Generation and control of tracer particles for optical flow investigations in air. *Experiments in Fluids*, 33:736–742, 2002. ISSN 07234864. DOI: 10.1007/s00348-002-0492-x.
- Katz, M. *Introduction to Geometrical Optics*. World Scientific Publishing Company, 2002.
- Kent, J. C. and Eaton, A. R. Stereo photography of neutral density He-filled bubbles for 3-D fluid motion studies in an engine cylinder. *Applied Optics*, 21(5):904–912, 1982. ISSN 0003-6935. DOI: 10.1364/ao.21.000904.
- Kerho, M. F. and Bragg, M. B. Neutrally buoyant bubbles used as flow tracers in air. *Experiments in Fluids*, 16:393–400, 1994. ISSN 07234864. DOI: 10.1007/BF00202064.
- Kim, D., Kim, M., Saredi, E., Scarano, F., and Kim, K. C. Robotic PTV study of the flow around automotive side-view mirror models. *Experimental Thermal and Fluid Science*, 119:110202, 2020. ISSN 08941777. DOI: 10.1016/j.expthermflusci.2020.110202.
- Klimas, P. C. Helium bubble survey of an opening parachute flowfield. *Journal of Aircraft*, 10(9):567–569, 1973. ISSN 00218669. DOI: 10.2514/3.44391.
- Kühn, M., Ehrenfried, K., Bosbach, J., and Wagner, C. Large-scale tomographic particle image velocimetry using helium-filled soap bubbles. *Experiments in Fluids*, 50:929–948, 2011. ISSN 07234864. DOI: 10.1007/s00348-010-0947-4.
- Lobutova, E., Resagk, C., Rank, R., and Dirk, M. Extended Three Dimensional Particle Tracking Velocimetry for Large Enclosures. In *Imaging Measurement Methods for Flow Analysis*, pages 113–124. Springer Berlin Heidelberg, 2009.
- Lock, C. N. H. Photographs of Streamers Illustrating the Flow Around an Airscrew in the Vortex Ring State. *Aeronautical Research Committee Reports and Memoranda 1167 (Ae. 331)*, (Apr), 1928.
- Loth, E. Quasi-steady shape and drag of deformable bubbles and drops. *International Journal of Multiphase Flow*, 34(6):523–546, 2008. ISSN 03019322. DOI: 10.1016/j.ijmultiphaseflow.2007.08.010.
- Lynch, K. P. *Advances in Time-Resolved Tomographic Particle Image Velocimetry*. PhD thesis, Delft University of Technology, 2015.
- Macháček, M. *A quantitative Visualization tool for large wind tunnel experiments*. PhD thesis, ETH Zürich, 2003.
- Mamaikin, D., Knorsch, T., Rogler, P., and Wensing, M. Experimental investigation of flow field and string cavitation inside a transparent real \square size GDI nozzle. *Experiments in Fluids*, 61:154, 2020. ISSN 1432-1114. DOI: 10.1007/s00348-020-02982-y.

- Mansfield, C. R. and Peck, E. R. Dispersion of Helium. *Journal of the Optical Society of America*, 59 (2):199–204, 1969.
- Marshall, J. S. and Li, S. *Adhesive Particle Flow: A Discrete-Element Approach*. Cambridge University Press, 2014. DOI: 10.1017/CBO9781139424547.
- Maxey, M. R. and Riley, J. J. Equation of motion for a small rigid sphere in a nonuniform flow. *Physics of Fluids*, 26(4):883–889, 1983. ISSN 10706631. DOI: 10.1063/1.864230.
- Mei, R. Velocity fidelity of flow tracer particles. *Experiments in Fluids*, 22:1–13, 1996. ISSN 07234864. DOI: 10.1007/BF01893300.
- Melling, A. Tracer particles and seeding for particle image velocimetry. *Measurement Science and Technology*, (12):1406–1416, 1997. ISSN 09570233. DOI: 10.1088/0957-0233/8/12/005.
- Mie, G. Beiträge zur Optik trüber Medien, speziell kolloidaler Metallösungen. *Annalen der Physik*, 330 (3):377–445, 1908.
- Morias, K. On the tracing fidelity of helium-filled soap bubbles for PIV experiments. Master's thesis, Delft University of Technology, 2016.
- Morias, K. L. L., Caridi, G. C. A., Sciacchitano, A., and Scarano, F. Statistical Characterization of Helium-Filled Soap Bubbles Tracing Fidelity for PIV. *18th International Symposium on the Application of Laser and Imaging Techniques to Fluid Mechanics*, 2016.
- Müller, D. and Renz, U. A particle streak tracking system (pst) to measure flow fields in ventilated rooms. *Air Distribution in Rooms: Ventilation for Health and Sustainable Environment*, 2:325–331, 2000.
- Müller, D., Müller, B., and Renz, U. Three-dimensional particle-streak tracking (PST) velocity measurements of a heat exchanger inlet flow. *Experiments in Fluids*, 30:645–656, 2001. ISSN 07234864. DOI: 10.1007/s003480000242.
- Nakagawa, M., Kallweit, S., Michaux, F., and Hojo, T. Typical Velocity Fields and Vortical Structures around a Formula One Car, based on Experimental Investigations using Particle Image Velocimetry. *SAE International Journal of Passenger Cars - Mechanical Systems*, 9(2), 2016. ISSN 19464002. DOI: 10.4271/2016-01-1611.
- Okuno, Y., Fukuda, T., Miwata, Y., and Kobayashi, T. Development Of Three-Dimensional Air Flow Measuring Method Using Soap Bubbles. *JSAE Review*, 14(4):50–55, 1993.
- Oudheusden, van, B. W., Schrijer, F. F. J., and Scarano, F. Application of PIV in a Mach 7 double-ramp flow. *Experimental Eye Research*, 41:353–363, 2006. DOI: 10.1007/s00348-006-0140-y.
- Pfitzner, J. Poiseuille and his law. *Anaesthesia*, 31:273–275, 1976. ISSN 13652044. DOI: 10.1111/j.1365-2044.1976.tb11804.x.
- Pounder, E. Parachute inflation process Wind-Tunnel Study. Technical report, Wright Air Development Center, Air Research and Development Command, Ohio, 1956.
- Pröbsting, S., Scarano, F., Bernardini, M., and Pirozzoli, S. On the estimation of wall pressure coherence using time-resolved tomographic PIV This article is part of the topical collection on application of laser techniques to fluid mechanics 2012. *Experiments in Fluids*, 54:1567, 2013. ISSN 07234864. DOI: 10.1007/s00348-013-1567-6.
- Raffel, M., Willert, C. E., Scarano, F., Kähler, C. J., Wereley, S. T., and Kompenhans, J. *Particle Image Velocimetry - A Practical Guide*. Springer International Publishing AG, 3 edition, 2018. ISBN 9783319688510. DOI: 10.3139/9783446436619.
- Ragni, D., Schrijer, F., Oudheusden, van, B. W., and Scarano, F. Particle tracer response across shocks measured by PIV. *Experiments in Fluids*, 50:53–64, 2011. ISSN 07234864. DOI: 10.1007/s00348-010-0892-2.

- Redon, M. and Vinsonneau, M. Etude de l'écoulement d'une maquette. *Bulletin L'Aerotechnique*, 18 (204):60–66, 1936.
- Rhode, D. L. *Predictions and Measurements of Isothermal Flow-Fields in Axisymmetric Combustor Geometries*. PhD thesis, Oklahoma State University, 1981.
- Rosi, G. A., Sherry, M., Kinzel, M., and Rival, D. E. Characterizing the lower log region of the atmospheric surface layer via large-scale particle tracking velocimetry. *Experiments in Fluids*, 55:1736, 2014. ISSN 07234864. DOI: 10.1007/s00348-014-1736-2.
- Samimy, M. and Lele, S. K. Motion of particles with inertia in a compressible free shear layer. *Physics of Fluids A*, 3:1915–1923, 1991. ISSN 08998213. DOI: 10.1063/1.857921.
- Scarano, F. Tomographic PIV: Principles and practice. *Measurement Science and Technology*, 24, 2013a. ISSN 13616501. DOI: 10.1088/0957-0233/24/1/012001.
- Scarano, F. AE 4180: Experimental Aerodynamics, 2013b. Lecture Notes.
- Scarano, F. *Overview of PIV in Supersonic Flows*, pages 445–463. Springer Berlin Heidelberg, 2008. ISBN 978-3-540-73528-1. DOI: 10.1007/978-3-540-73528-1_24.
- Scarano, F. and Poelma, C. Three-dimensional vorticity patterns of cylinder wakes. *Experiments in Fluids*, 47:69–83, 2009. ISSN 07234864. DOI: 10.1007/s00348-009-0629-2.
- Scarano, F., Ghaemi, S., Caridi, G. C. A., Bosbach, J., Dierksheide, U., and Sciacchitano, A. On the use of helium-filled soap bubbles for large-scale tomographic PIV in wind tunnel experiments. *Experiments in Fluids*, 56:42, 2015. ISSN 07234864. DOI: 10.1007/s00348-015-1909-7.
- Schanz, D., Gesemann, S., and Schröder, A. Shake-The-Box: Lagrangian particle tracking at high particle image densities. *Experiments in Fluids*, 57, 2016. ISSN 07234864. DOI: 10.1007/s00348-016-2157-1.
- Schiller, L. and Naumann, A. Über die grundlegende berechnungen bei der schwerkraft-aufbereitung. *Zeitschrift des Vereines Deutscher Ingenieure*, 77:318–320, 1933.
- Schlichting, H. and Gersten, K. *Boundary Layer Theory*. 9 edition, 2017. ISBN 9783662529171.
- Schneiders, J. F., Caridi, G. C., Sciacchitano, A., and Scarano, F. Large-scale volumetric pressure from tomographic PIV with HFSB tracers. *Experiments in Fluids*, 57:164, 2016. ISSN 07234864. DOI: 10.1007/s00348-016-2258-x.
- Schröder, A., Schanz, D., Heine, B., and Dierksheide, U. *Investigation of Transitional Flow Structures Downstream of a Backward-Facing-Step by Using 2D-2C- and High Resolution 3D-3C- Tomo- PIV*, pages 219–226. Springer Berlin Heidelberg, Berlin, Heidelberg, 2013. ISBN 978-3-642-35680-3. DOI: 10.1007/978-3-642-35680-3_27.
- Schröder, A., Geisler, R., Elsinga, G. E., Scarano, F., and Dierksheide, U. Investigation of a turbulent spot and a tripped turbulent boundary layer flow using time-resolved tomographic PIV. *Experiments in Fluids*, 44:305–316, 2008. ISSN 07234864. DOI: 10.1007/s00348-007-0403-2.
- Sciacchitano, A., Caridi, G. C. A., and Scarano, F. A quantitative flow visualization technique for on-site sport Aerodynamics optimization. *Procedia Engineering*, 112:412–417, 2015. ISSN 18777058. DOI: 10.1016/j.proeng.2015.07.217.
- Senft, V. and Gillan, M. A. Recent advances and test processes in automotive and motorsports aerodynamic development. *Journal of Mechanical Engineering Science*, 233, 2019. DOI: 10.1177/0954406219875770.
- Smith, D. M., Goodwin, T. W., and Schillinger, J. A. Challenges to the Worldwide Supply of Helium in the Next Decade. *AIP Conference Proceedings*, 710:119, 2004. ISSN 15517616. DOI: 10.1063/1.1774674.

- Staack, K., Geisler, R., Schröder, A., and Michaelis, D. 3D3C-coherent structure measurements in a free turbulent jet. In *15th International Symposium on Applications of Laser Techniques to Fluid Mechanics*, 2010.
- Symon, S., Dovetta, N., Mckeon, B. J., Sipp, D., Schmid, P. J., and Symon, S. Data assimilation of mean velocity from 2D PIV measurements of flow over an idealized airfoil flow and the minimum experimental measurements needed. *Experiments in Fluids*, 58:61, 2017. ISSN 1432-1114. DOI: 10.1007/s00348-017-2336-8.
- Terra, W., Sciacchitano, A., and Scarano, F. Aerodynamic drag of transiting objects by large-scale tomographic-PIV. In *Proceedings of the 18th International Symposium on the Application of Laser and Imaging Techniques to Fluid Mechanics*, Lisbon, Portugal, 2016. Springer.
- Tescione, G., Ragni, D., He, C., Simão Ferreira, C. J., and van Bussel, G. J. Near wake flow analysis of a vertical axis wind turbine by stereoscopic particle image velocimetry. *Renewable Energy*, 70: 47–61, 2014. ISSN 09601481. DOI: 10.1016/j.renene.2014.02.042.
- Tropea, C. Optical Particle Characterization in Flows. *Annual Review of Fluid Mechanics*, 43:399–426, 2011. ISSN 0066-4189. DOI: 10.1146/annurev-fluid-122109-160721.
- Tropea, C., Yarin, A. L., and Foss, J. F. *Springer Handbook of Experimental Fluid Mechanics*. 2007.
- TSI Incorporated. Flow characterization of bio-medical devices, 2019. URL https://tsi.com/getmedia/d7f48245-dc8b-4836-a9c3-d08a10e320df/PIV-026_Flow_Characterization_Bio-Medical_Devices_A4-web?ext=.pdf.
- Urban, W. D. and Mungal, M. G. Planar velocity measurements in compressible mixing layers. *Journal of Fluid Mechanics*, 431(March):189–222, 2001. ISSN 00221120. DOI: 10.1017/S0022112000003177.
- Utada, A. S., Lenceau, E., Link, D. R., Kaplan, P. D., Stone, H. A., and Weitz, D. A. Monodisperse double emulsions generated from a microcapillary device. *Science*, 308(5721):537–541, 2005. ISSN 00368075. DOI: 10.1126/science.1109164.
- Uzol, O., Chow, Y.-C., Katz, J., and Meneveau, C. Average Passage Flow Field and Deterministic Stresses in the Tip and Hub Regions of a Multistage Turbomachine. *Journal of Turbomachinery*, 125 (4):714–725, 12 2003. ISSN 0889-504X. DOI: 10.1115/1.1625692.
- Violato, D., Moore, P., and Scarano, F. Lagrangian and Eulerian pressure field evaluation of rod-airfoil flow from time-resolved tomographic PIV. *Experiments in Fluids*, 50:1057–1070, 2011. ISSN 07234864. DOI: 10.1007/s00348-010-1011-0.